A MULTIMESSENGER APPROACH TO NEUTRINO ASTRONOMY

A Dissertation
Presented to
The Academic Faculty

By

Chun Fai Tung

In Partial Fulfillment
of the Requirements for the Degree
Doctor of Philosophy in the
School of Physics
College of Sciences

Georgia Institute of Technology

May 2021

© Chun Fai Tung 2021

A MULTIMESSENGER APPROACH TO NEUTRINO ASTRONOMY

Thesis committee:

Dr. Ignacio J. Taboada
School of Physics
Georgia Institute of Technology

Dr. Laura Cadonati
School of Physics
Georgia Institute of Technology

Dr. David R. Ballantyne
School of Physics
Georgia Institute of Technology

Dr. Michael Crenshaw
Department of Physics and Astronomy
Georgia State University

Dr. Nepomuk A. Otte
School of Physics
Georgia Institute of Technology

Date approved: April 7, 2021

To Hong Kong

ACKNOWLEDGMENTS

First off, I want to thank my advisor Prof. Ignacio Taboada for the help and guidance he provided in the past six years. The completion of this thesis would not be possible without his support.

I would also like to thank many people in IceCube: Prof. Markus Ahlers and Prof. George Japaridze, for their help in the development of FIRESONG; Prof. Erik Blaufuss for his support in the realtime alert update; Qinrui Liu for her scientific discussion and memes which propelled the X-ray binaries analysis forward; my fellow group members Dr. Dirk Lennarz, Pranav Dave and Chujie Chen, from whom I always got good suggestions.

For making my experience in Georgia Tech fun and interesting, I would like to show my gratitude to my fellow graduate students and more importantly, friends: Maryrose Barrios, Dr. Matt Gudorf, Dr. Zach Jackson and his wife Kristen Jackson, Dr. Rana Jafari, Bhavesh Khamesra, Dr. Shashank Markande, Dr. Adrien Saremi, and Hemaa Selvakumar. I also want to thank my friends in Hong Kong, Michael Tang and Chun Ho Lau, for frequently checking up on me.

Finally, I want to thank my family for always being supportive to my decisions.

TABLE OF CONTENTS

LIST OF TABLES

LIST OF FIGURES

LIST OF ACRONYMS

AGN active galactic nucleus

CC charged current

CMB cosmic microwave background

CR cosmic ray

DIS deep inelastic scattering

DOM digital optical module

EBL extragalactic background light

EHE extreme high-energy

EM electromagnetic

FSRQ flat-spectrum radio quasar

GFU GammaFollowUp

GRB gamma-ray burst

GZK Greisen-Zatsepin-Kuzmin

HESE high-energy starting-events

HLC hard local coincidence

ICL IceCube Laboratory

MAGIC Major Atmospheric Gamma Imaging Cherenkov Telescope

MPE multi photoelectron

NC neutral current

PE photoelectrons

PnF Processing and Filtering

SFR star formation rate

SLC soft local coincidence

SMT simple multiplicity trigger

SPE single photoelectron

UHECR ultra high energy cosmic ray

VHE very high energy

WB Waxman-Bachall

WR Wolf-Rayet

XRB X-ray binary

SUMMARY

Neutrino astronomy is an emerging branch of astronomy which studies the high energy cosmos with neutrinos from astrophysical objects. Currently still at the ”discovery” stage, neutrino astronomy's progression towards the ”science” stage has proven to be difficult, mainly due to limited statistics. This motivates a multimessenger approach, one that combines the information delivered by different messengers instead of relying on neutrinos alone, in identifying the source of cosmic neutrinos. In this dissertation, three works based on the multimessenger approach are presented. The first one is an open source software known as FIRESONG, which is designed to generate neutrino flux distributions that include the effects due to cosmology and source density evolution. It has been used by different collaborations in the particle astrophysics community to interpret the findings from IceCube Neutrino Observatory and apply them in their analyses. The second one is the update for IceCube's Realtime Neutrino Alert System. This updated system has an increased alert rate, improved resolution on the arrival direction, a reduced retraction rate, and a more user-friendly alert classification. These improvements promote the general astronomical community to perform follow-up observation for interesting IceCube events, therefore increasing the chance to observe any rare transient astrophysical events. The third one is a search for periodically modulated neutrino emission from X-ray binaries(XRB). Binaries with a compact object have long been considered as galactic neutrino sources. The method for this search involves using the orbital periods measured by electromagnetic (EM) observations to improve the sensitivity. The search was performed on 55 XRBs with more than 1.5 million neutrino events collected by IceCube from 2011 to 2018, and no significant emission was found. Upper limits on the neutrino flux from each XRB were calculated. The upper limits of the two XRBs were compared with the neutrino flux predicted by phenomenological models.

CHAPTER 1

COSMIC RAYS AND NEUTRINO ASTRONOMY

For millennia, astronomers like Ptolemy, Galileo, Hubble, and Penzias and Wilson, have learned everything about the universe from light, or more generally, electromagnetic (EM) waves. Since photons of different wavelengths are emitted by processes of different energy levels, the multiwavelength approach allows astronomers to study celestial objects in more detail. Unfortunately, there is a limit to what we can study with traditional EM astronomy. Photon-photon collisions are capable of producing electron-positron pairs, known as Breit-Wheeler pair production,

$$\gamma + \gamma \rightarrow e^- + e^+, \tag{1.1}$$

as long as the product of the photon energies satisfies the kinematic requirement

$$E\epsilon \geq (m_e c^2)^2, \tag{1.2}$$

where E and ϵ are the energies of the two photons in the center-of-mass frame. Due to pair productions, PeV photons will be attenuated by the cosmic microwave background (CMB) photons within 1 Mpc of propagation, and TeV photons will be attenuated by the infrared photons present in the extragalactic background light (EBL) [1]. As a result, the high energy landscape of the extragalactic sources cannot be observed with photons. Figure 1.1 shows the maximum observable distance as a function of the energy of the photon. The drop between 10^{10} and 10^{13} eV is due to EBL while the dip centered at 10^{15} eV is due to CMB. This prompts us the question: Can we study our universe with messengers other than EM waves? The answer is positive, and one of the alternatives is to study the universe with neutrinos.

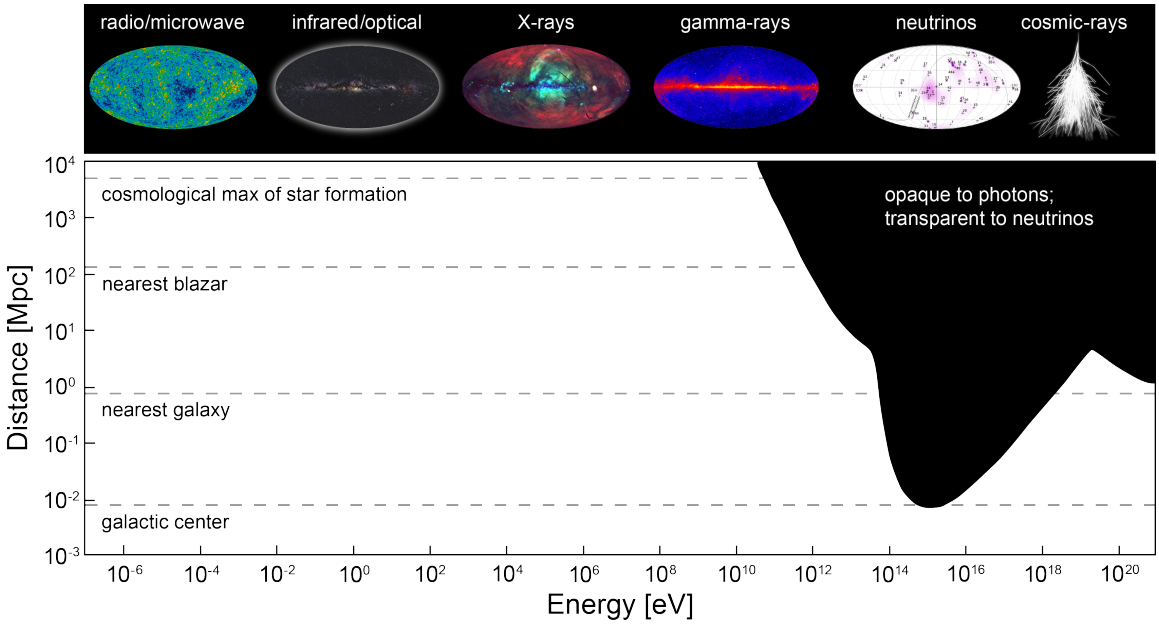

Figure 1.1: The observable range for photons at different energy. Figure produced by the IceCube Collaboration.

1.1 Cosmic Rays

One of the most important open questions in high energy astrophysics is the origin of ultra high energy cosmic ray (UHECR). Before discussing the cosmic-ray origin problem, in this section, some current knowledge of cosmic rays should be reviewed. Cosmic rays (CR) are high energy particles from outside the solar system, and they were first discovered by Victor Hess in 1912 [2]. They are mainly composed of atomic nuclei synthesized by stars (hydrogen, helium, oxygen, carbon, iron), and elementary particles (electrons, positrons). Among the nuclei, hydrogen and helium dominate the composition. About 74% of the CR nucleons are in the form of free proton (hydrogen nuclei) and about 18% are bounded in the form of helium nuclei [3]. These particles can be further classified into primary cosmic rays and secondary cosmic rays, where primaries are those accelerated at the unknown sources, and secondaries are produced by interactions between interstellar gas and primary cosmic rays.

The spectrum of cosmic rays spans over 10 decades in energy, ranging from GeV to

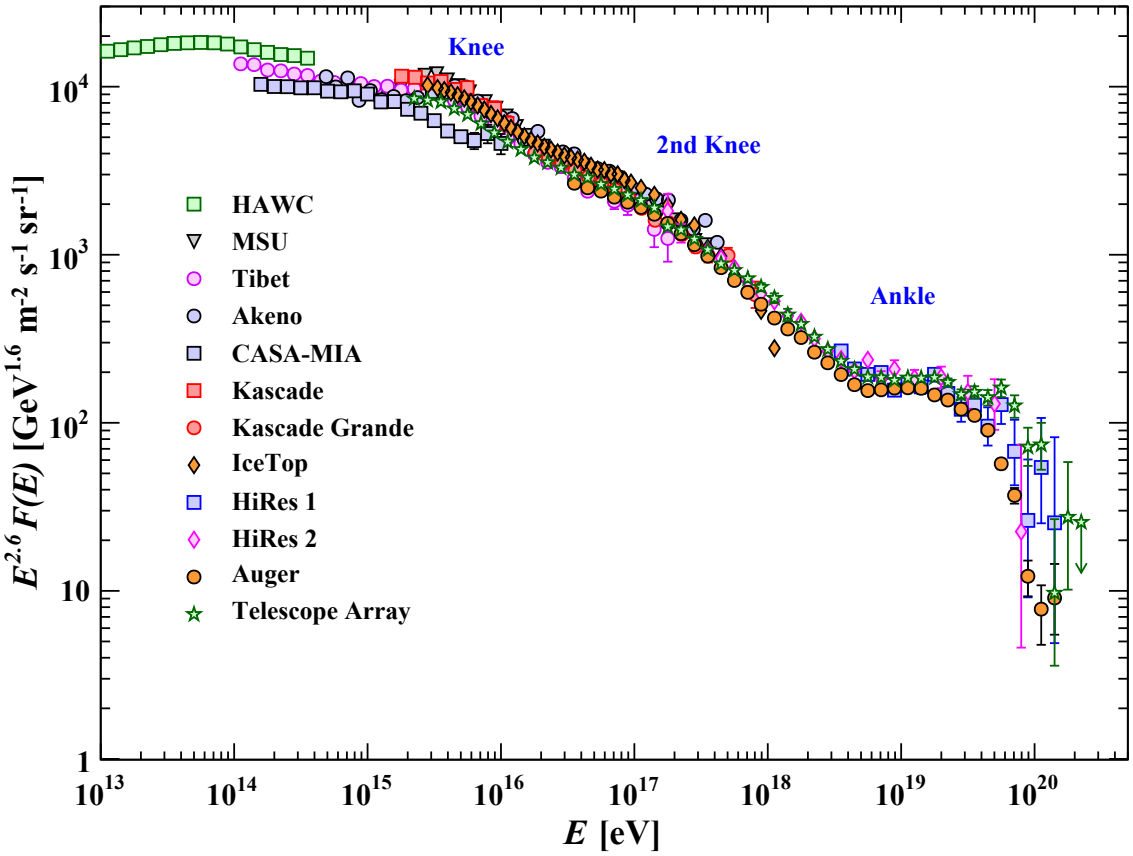

Figure 1.2: "All-particle" cosmic-ray spectrum measured by various air shower experiments listed in the legend. The spectrum is multiplied by $E^{2.6}$ to signify the different features. Figure is reproduced from [3].

100 EeV. In the lower energy range between 10 GeV and 100 TeV, the differential nucleon intensity of primary cosmic rays can be approximated by a single power law with a spectral index -2.7:

$$I_N(E) = 1.8 \times 10^4 \left(\frac{E}{\mathrm{GeV}}\right)^{-2.7} \frac{\mathrm{nucleon}}{\mathrm{GeV\,s\,m^2\,sr}}, \tag{1.3}$$

where E is the energy per nucleon. Above 100 TeV (10^{14} eV), there are three major features in the spectrum. The first one is a sudden steepening that happens between 10^{15} and 10^{16} eV, which is known as "the knee". The second feature is another steepening that happens around 10^{17} eV, and is known as "the second knee". The third feature is a hardening of the spectrum, which happens at around $10^{18.5}$ eV, which is known as "the ankle". Finally, the spectrum falls off sharply below 10^{20} eV. The cosmic-ray spectrum up to the cut-off energy

has been measured by various experiments. Their results are plotted in Figure 1.2 [3]. It should be noted at cosmic rays above 10^{18} eV are usually referred to as UHECR.

The origins of the different features in the spectrum are still being investigated. The current data and models suggest that the first knee may be originated from the limit on the maximum energy a proton can gain from galactic accelerators. For example, supernova remnants can only accelerate protons up to 10^{15} eV [3]. Under the same accelerator, the maximum energy of the nucleus scales with its charge, i.e. a nucleus of charge Ze will have a maximum energy of Z times the maximum energy of a proton [4]. Thus, the steepening of the heavier nuclei happen at a higher energy, with iron nuclei having the highest energy limit among the primaries. This may produce the second knee in the spectrum.

A possible origin for the ankle is that the extragalactic population overtake the galactic population at $10^{18.5}$ eV. The cosmic rays from extragalactic sources are believed to be more energetic than those from galactic sources, because of the larger size or the stronger magnetic field strength of the extragalactic accelerators. Thus, it might explain the hardening of the spectrum observed at the ankle. Starting at $10^{18.5}$ eV, the cosmic rays are mostly extragalactic, so they have propagated over 100 Mpc before reaching Earth. In this energy range and over the cosmic distance, high energy protons can interact with the CMB photons to produce electron-positron pairs, in a way similar to the Breit-Wheeler process mentioned at the beginning of this chapter. The pair production will cause the protons to lose energy, which may explain the dip feature at the ankle.

Protons at 5×10^{19} eV can produce pion with the CMB photon through Δ resonance

$$p + \gamma_{\mathrm{CMB}} \rightarrow \Delta^{+} \rightarrow \begin{cases} p + \pi^{0}, \\ n + \pi^{+}. \end{cases} \tag{1.4}$$

In either case, the proton will lose a large fraction of its energy to the pion. As a result, the cosmic-ray spectrum is predicted to have a sharp steepening at 5×10^{19} eV, known as the Greisen-Zatsepin-Kuzmin (GZK) feature [5][6]. In a mixed composition model, photo-

dissociation of nuclei can also produce a similar suppression at the said energy. Pierre Auger Observatory and Telescope Array both detected this feature in the spectrum [7][8]. Nonetheless, recent data seems to support the existence of flux suppression at the GZK energy.

1.2 Origin of Cosmic Rays

Since cosmic rays are charged particles, their directions are scrambled by the galactic and intergalactic magnetic field during the propagation. The angle of deflection for a proton with energy E can be estimated from the gyroradius of this field

$$\theta \approx \frac{d}{R_{\text{gyro}}} = \frac{dB}{E}, \tag{1.5}$$

where d is the distance between the source and Earth, B is the strength of the inter-galactic magnetic field. For a distance of 100 Mpc and $B = 10^{-9}$ Gauss, even the protons at GZK limit are deflected by more than 10 degrees. On top of that, the highest energy CR events happen at a rate of about 1 event per km^2 per century, so the statistics are very limited. As a result, it is almost impossible to locate the source by tracing the incoming direction of the cosmic rays. It should be noted that Pierre Auger Observatory has detected a dipole anisotropy in CRs above 8×10^{18} eV [9]. This anisotropy in UHECRs could be caused by the dipole anisotropy observed in the galaxy distribution observed by 2MRS [10].

Besides the pointing problem, it is also still a mystery how UHECRs acquire energies up to 10^{20} eV. If we assume cosmic-ray protons are confined in a magnetic field during the acceleration, the size of the accelerator R must be larger than the gyroradius R_g

$$R > R_g = \frac{E}{B}, \tag{1.6}$$

where E is the energy of the proton and B is the magnetic field strength of the acceleration. Equation 1.6 is known as the Hillas criterion, and it limits the potential cosmic-ray sources

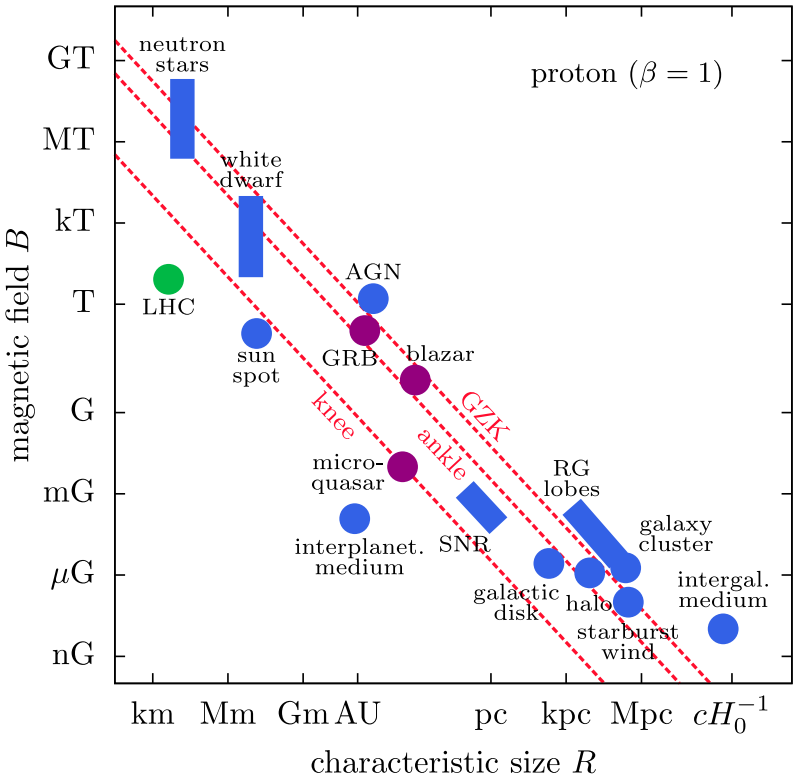

Figure 1.3: A modern version of the Hillas plot. Different potential cosmic-ray sources are plotted according to their magnetic field and size. The red lines are the criteria for the sources to emit cosmic rays at the energy of the knee, ankle and above GZK limit. Figure is reproduced from [11].

to a handful of astrophysical objects. Figure 1.3 shows the magnetic field plotted against the size of different potential cosmic-ray sources. The red lines in the plot are the boundaries for producing cosmic rays with energy up to the knee (3×10^{15} eV), ankle (3×10^{18} eV), and above GZK limit (10^{21} eV). However, the Hillas criterion is a dimensional analysis assuming an optimized accelerator with perfectly aligned magnetic field. It is unlikely for natural particle accelerators to have the same optimization as the man-made counterpart.

1.2.1 Acceleration Mechanism

A viable acceleration mechanism for cosmic rays must be able to reproduce the power law spectrum. Consider a generic acceleration mechanism that is diffusive, i.e. the particles gain energy through multiple non-continuous interaction. In this model, the energy gain

from each interaction is proportional to the energy of the particle

$$\Delta E = \beta E. \tag{1.7}$$

After n interaction, the energy of the particle will be

$$E(n) = E_0\, e^{n\beta}. \tag{1.8}$$

If the particle has a fixed probability P to remain in the acceleration region after each interaction, the number of particles experienced at least n interaction is

$$N(\geq n) = N_0\, P^n. \tag{1.9}$$

By substituting n with E, the number of particle as a function of E is

$$N(\geq E) = N_0 \times \left(\frac{E}{E_0}\right)^{\ln P/\ln \beta}, \tag{1.10}$$

so the particle spectrum will also follow a power law with a spectral index $\ln P/\ln \beta - 1$. The spectral index is controlled by the escape probability and the coefficient of energy transfer in each interaction. Thus, an acceleration mechanism for cosmic rays should have these parameters set to give the observed spectral index.

The most widely accepted diffusive acceleration mechanism is known as first-order Fermi acceleration. In the original version (now known as second-order Fermi acceleration) proposed by Enrico Fermi in 1949 [12], relativistic particles are accelerated by repeated collisions with randomly moving, non-relativistic "magnetic mirrors". In practice, massive interstellar clouds can act as these mirrors. Figure 1.4a shows the scattering of a particle by an interstellar cloud. If the particle is relativistic, the energy of the particle in the cloud's

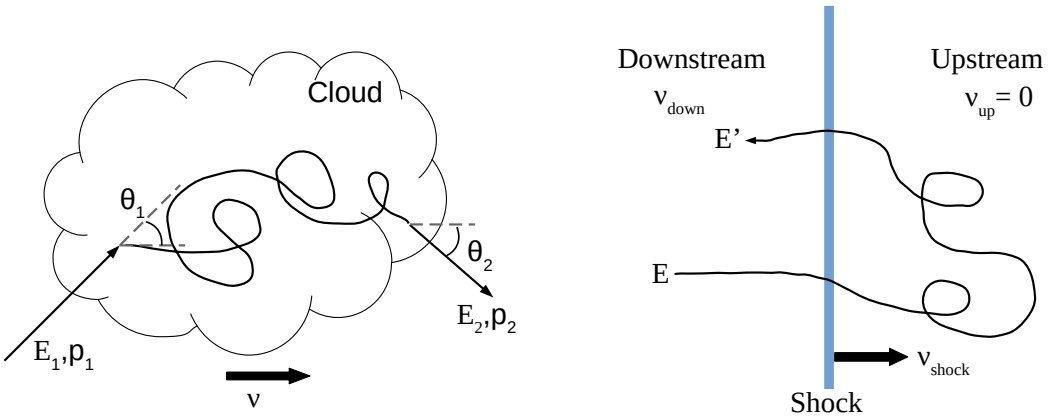

(a) (b)

Figure 1.4: (a) Illustration of a particle scattered by a cloud. (b) Illustration of a particle from downstream crossing the shock to upstream, then crossing the shock again to returning to downstream.

frame will be

$$E_1' = \gamma E_1(1 - \beta\cos\theta_1), \tag{1.11}$$

where $\gamma = \sqrt{1-\beta^2}^{-1}$, $\beta = v/c$, and v is the speed of the cloud. Since the cloud is massive, we can assume the particle energy is constant inside the cloud, i.e., $E_1' = E_2'$. The energy of the particle in the lab frame after leaving the cloud is

$$E_2 = \gamma E_2'(1 + \beta\cos\theta_2). \tag{1.12}$$

The average fractional energy change is

$$\begin{aligned}\langle\frac{E_2 - E_1}{E_1}\rangle &= \langle\gamma^2(1 - \beta\cos\theta_1 + \beta\cos\theta_2 - \beta^2\cos\theta_1\cos\theta_2) - 1\rangle \\ &\approx -\beta\langle\cos\theta_1\rangle\end{aligned} \tag{1.13}$$

where the approximation is performed because the cloud is non-relativistic, and the outgoing angle θ_2 is isotropic. The particle will gain energy if the collision is head-on ($\cos\theta_1 < 0$), but will lose energy when the collision is tail-end ($\cos\theta_1 > 0$). However, the collision frequency favors head-on collisions. Therefore, after averaging the collision angle,

the energy gain per collision is [13]

$$\Delta E = \frac{4}{3}\left(\frac{v}{c}\right)^2 E. \tag{1.14}$$

Since the energy gain depends on the second order of the cloud velocity v/c, this mechanism is now known as second-order Fermi acceleration. However, because of the second order dependence on the small factor v/c, this process is not efficient enough to produce the desired -2.7 spectrum.

The efficiency can be improved if all collisions are head-on. A modified version of Fermi acceleration, known as first order Fermi acceleration, achieves this using strong shocks in the accelerator, which have been observed in objects like supernovae, active galactic nucleus (AGN), etc. In the model, the shock is propagating at a speed v_s. For a strong shock (Mach number $\gg 1$), the shocked gas in the downstream area is moving with a speed $v_{\text{down}} \approx 0.75 v_s$, while the gas upstream is at rest. Due to turbulence and irregularities, the particles' directions are distributed isotropically in the rest frame of the gas in either region. If the outgoing direction is away from the shock, the particle will escape, but if it is toward the shock, the particle will collide with the gas approaching at v_{down}, regardless of the side of the shock. Thus, every collision is head-on. Figure 1.4b illustrate the scenario of a particle crossing the shock twice.

Since the collisions are always head-on, the average collision angle no longer depends on the velocity of the shock. Therefore, following the same calculation for the cloud scattering, the average energy gained by the particle in a round-trip is [13]

$$\Delta E = \frac{4}{3}\left(\frac{v_{\text{down}}}{c}\right) E, \tag{1.15}$$

which is of first order in v/c. Using a similar argument, it can be shown that the escape

probability for a particle from a strong shock is approximately

$$P_{\rm esc} = (1 - P) = \frac{4}{3}\left(\frac{v_{\rm down}}{c}\right). \tag{1.16}$$

It is then straightforward to derive the spectral index of the cosmic-ray spectrum,

$$\Gamma = \frac{\ln P}{\ln \beta} - 1 \approx -2, \tag{1.17}$$

assuming the downstream gas is non-relativistic.

Although the predicted spectral index is not -2.7 as the spectral index of the galactic CR, the first-order Fermi acceleration is still widely accepted. It is because the predicted hard spectrum provides room for spectral steepening due to propagation. For example, in the leaky box model of propagation, cosmic rays are confined in a volume, but can propagate freely and have a constant probability per unit time to escape. The escape probability depends on the element of the cosmic ray and its energy. For a proton, its mean path travelled before escaping is much shorter than the mean path travelled before interacting, i.e., high energy protons are very likely to escape the confinement. This results in an observed spectrum steeper than the source spectrum. According to [14], the observed hydrogen spectrum will have an index 0.6 steeper than the source spectrum in the leaky box model. There, the first-order Fermi acceleration can explain the observed CR spectrum when combined with a propagation model.

1.3 Multimessenger Approach to CR Origin Problem

Intense photon fields or dense gas clouds are expected to be found surrounding the accelerator, for example, the photons emitted by the accretion disk of an active galactic nucleus (AGN). During or after the acceleration, some of the cosmic rays will interact with these targets, and produce high energy neutrinos and very high energy (VHE) gamma rays. Since these secondary products are neutral, they will not be deflected by the magnetic field during

propagation. Thus, by detecting neutrinos and gamma rays, the sources of cosmic rays can be identified in a multimessenger approach.

However, given the potential cosmological distances these sources are at, the gamma rays will face significant attenuation by EBL, as discussed in the beginning of the chapter. Neutrinos, on the other hand, have an extremely small cross-section, a property that will be discussed more in depth in chapter 2. This allows neutrinos to reach Earth without much attenuation. Besides that, VHE gamma rays can be produced by up-scattering (Inverse Compton Scattering) with electrons, so a detection of VHE gamma rays alone is not enough evidence for identifying the cosmic-ray sources. In that sense, high energy neutrino production, which will be discussed in the next section, must involve high energy hadrons. Therefore, neutrinos are the ideal messenger for solving the UHECR origin problem.

1.4 Neutrino Production

High energy neutrinos are usually produced via the decay of charged mesons, such as pions and kaons, which are products of the interactions between cosmic rays and i) photons ($p\gamma$) and ii) hadrons (pp). In the $p\gamma$ path, pions are produced dominantly via Δ-resonance, which is stated in Equation 1.4, except the photons involved are not only in the microwave wavelengths, so the resonance can occur with protons with different energies. Alternatively, they can also be produced directly via

$$p + \gamma \rightarrow \begin{cases} n + \pi^+, \\ p + \pi^0, \end{cases} \tag{1.18}$$

It should be noted that at high energy, the direct pion production usually happens in the multi-π way, i.e.

$$p + \gamma \rightarrow p + a(\pi^0) + b(\pi^+ + \pi^-), \tag{1.19}$$

where a and b are the ratio of neutral and charged pions. As a remark, high energy neutrinos are also expected to be produced by the GZK mechanism. These neutrinos are usually referred to as cosmogenic neutrinos. They are almost guaranteed to be found in the highest energy portion of the neutrino flux at $\sim 10^{18}$ eV. However, the flux strength is uncertain because many factors, such as the composition of UHECRs, are not well known.

On the pp interactions side, both pions and kaons can be produced, with pions being the dominant product ($\sim$85%) [15]. Considering only pions, the most relevant interaction is in the form

$$p + p \rightarrow N_\pi \left[\pi^0 + \pi^+ + \pi^-\right] + X, \tag{1.20}$$

where N_π is the pion multiplicity, and X is a hadronic cascade. Combining the decay of pions and muons, the overall decay pathways are

$$\begin{aligned} \pi^+ &\rightarrow \mu^+ + \nu_\mu, \rightarrow e^+ + \nu_e + \bar{\nu}_\mu + \nu_\mu, \quad (> 99.9\%) \\ \pi^- &\rightarrow \mu^- + \bar{\nu}_\mu \rightarrow e^- + \bar{\nu}_e + \nu_\mu + \bar{\nu}_\mu, \quad (> 99.9\%) \\ \pi^0 &\rightarrow \gamma + \gamma, \quad (> 98.8\%) \end{aligned} \tag{1.21}$$

where the percentages in the parenthesis are the branching ratios for each pion. From Equation 1.21, the first takeaway is that high energy neutrinos are always accompanied by VHE gamma rays, at least at the production site. Whether or not these VHE gamma rays can reach Earth, however, is not guaranteed. They may be absorbed by the local environment or significantly attenuated by EBL if the source is far away. Therefore, it is possible for a neutrino source to be gamma-dark.

The second takeaway is the characteristic neutrino flavor ratio (with neutrinos and antineutrinos combined) at the source. In an ideal environment, the source flavor ratio is $\nu_e : \nu_\mu : \nu_\tau = 1 : 2 : 0$. However, if the environment is suitable, the lifetime of a high energy muon will be long enough for it to lose significant energy from interactions with photons and magnetic field before decaying, thus suppressing the number of high energy

ν_e [16]. Pion's lifetime is much shorter, so ν_μ is not affected as much. This would result in a source flavor ratio of $0:1:0$. Furthermore, the source flavor ratio will be modified by neutrino oscillations (see details in chapter 2) over the long distance propagation to Earth. The predicted flavor ratio on Earth is dependent on the source flavor ratio. The ratio on Earth will be $1:1:1$ if the ratio at the source is $1:2:0$, and $1:1.8:1.8$ if the ratio at the source is $0:1:0$ [16]. This suggests that the environment of the neutrino source can be studied by measuring the flavor ratio of astophysical neutrinos.

As a rough approximation, the pion usually retains one-fifth the energy of the proton, and the energy of the pion is distributed equally among the decay products. Thus, each neutrino will have about 1/20 of the primary energy while each gamma-ray photon will have about 1/10 of the primary energy [17].

1.5 Astrophysical Neutrino Flux: Upper Limit

The neutrino production mechanism allows one to derive the upper limit of astrophysical neutrino flux coming from CR-thin, extra-galactic sources, based on the observed cosmic rays. The neutrino flux limit set by UHECR is known as the Waxman-Bachall (WB) limit [18] [19]. The idea of WB limit can be summarized as follow: If high energy neutrinos are produced by cosmic-ray protons before leaving the site, their energy densities are related, i.e.

$$E_\nu^2 \frac{dN_\nu}{dE_\nu} = \zeta \epsilon E^2 \frac{dN_{\rm cr}}{dE_{\rm cr}}, \tag{1.22}$$

where ϵ is the fractional energy loss by the proton to the pion, and ζ is the fraction of pion energy transferred to neutrinos. Since the goal is to derive an upper limit, ϵ is chosen as 1, such that all sources are assumed to be CR-thin, i.e. the majority of CR can escape the source. If we consider muon neutrinos only, ζ will be about 0.25, assuming neutral pions and charged pions are produced with the same probability.

The energy production rate of cosmic-ray protons from nearby (redshift $z < 1$) sources

can be estimated for a given model of the injection spectrum and source distribution. For non evolving sources (those with a constant number density throughout the entire universe) and first-order Fermi acceleration, the power density is

$$E^2 \frac{dN_{\rm cr}}{dE_{\rm cr} dt} \approx 10^{44}\,{\rm erg\,Mpc^{-3}\,s^{-1}}. \tag{1.23}$$

To convert this to the energy density across the observable universe, the power density is multiplied by the Hubble time $t_H \sim 10^{10}\,{\rm yr}$. The neutrino flux upper limit of all flavours is then found as

$$\frac{c}{4\pi} E_\nu^2 \frac{dN_\nu}{dE_\nu} \approx \zeta \frac{c}{4\pi} t_H E^2 \frac{dN_{\rm cr}}{dE_{\rm cr} dt} \approx 4.4 \times 10^{-8}\,{\rm GeV\,cm^{-2}\,s^{-1}}. \tag{1.24}$$

It must be stressed that this value is for sources with no evolution. The upper limits for a specific class of astrophysical objects can be obtained in a similar by substituting their evolution model. For example, the calculations for gamma-ray burst (GRB) and AGNs were done in [18], and the difference in the upper limit is modest, which changed by about a factor of 3.

Although the limit is subject to the source evolution model, it nevertheless provides a handle on the order of magnitude of the astrophysical neutrino flux. To detect a neutrino flux about $10^{-8}\,{\rm GeV\,cm^{-2}\,s^{-1}}$, the size of the detector has to be in the order of a cubic kilometer. This prediction is used as one of the design criteria for IceCube.

1.6 Atmospheric Neutrinos

Obviously, cosmic rays will interact with Earth's atmosphere when they arrive. This begins at about 15 km above sea level. The interactions produce hadronic showers, which contain mesons such as kaons and pions, and leptons such as electrons, positrons. Electrons and positrons can annihilate each other quickly to produce electromagnetic showers of gamma rays; while the mesons can either interact with other nuclei in the atmosphere to produce

more mesons or decay into leptons and produce neutrinos.

Neutrinos produced by the decay of charged pions, kaons, and muons are known as conventional atmospheric neutrinos. Pions contribute the majority of the neutrinos below 100 GeV and kaons dominate the contribution above that. This variation in contribution is due to the fact that pions have a longer lifetime than kaons, so they are more likely to interact and lose energy. Furthermore, because muons have a lifetime about 100 times longer than the pions, their contribution to neutrinos is the smallest in the energy range relevant to IceCube ($\geq 100\,\mathrm{GeV}$). For experiments like Super-K, which detects neutrinos in the lower energy range, the contribution from muons is important. The fractions of pion's and kaon's contribution to neutrinos and muons are shown in Figure 1.5a.

Given that pions and kaons mostly decay into muons and muon neutrinos, in IceCube's energy range, the muon neutrino flux is about 20 times that of electron neutrinos, which mainly come from muon decay. Since high energy mesons are more likely to interact with the atmosphere before decaying, atmospheric neutrinos are more likely to be produced by lower energy mesons. Hence, the spectral index of the atmospheric muon neutrino flux is about 1 order steeper than that of the cosmic-ray spectrum, and the atmospheric electron neutrino flux is about 2 order steeper. These two fluxes have been calculated with different models [20], and the zenith-averaged flux of muon neutrinos and electron neutrinos are shown in Figure 1.5b, labeled as the conventional fluxes. The fluxes are also zenith-dependent, with its maximum at the horizon, because mesons can reach the ground before decaying into neutrinos and muons.

Neutrinos may also come from the decay of charmed mesons. These neutrinos are known as the prompt neutrinos. Some possible charmed mesons that can be produced by cosmic rays are the D mesons ($D^{\pm}, D^{0}, D_{s}$). Due to the short lifetime of this charmed mesons, they have a low probability to interact in the atmosphere. Therefore, the prompt neutrino flux will not be as steep as the conventional flux, but will be closer to the cosmic-ray spectrum. The expected fluxes calculated using four different models are also shown

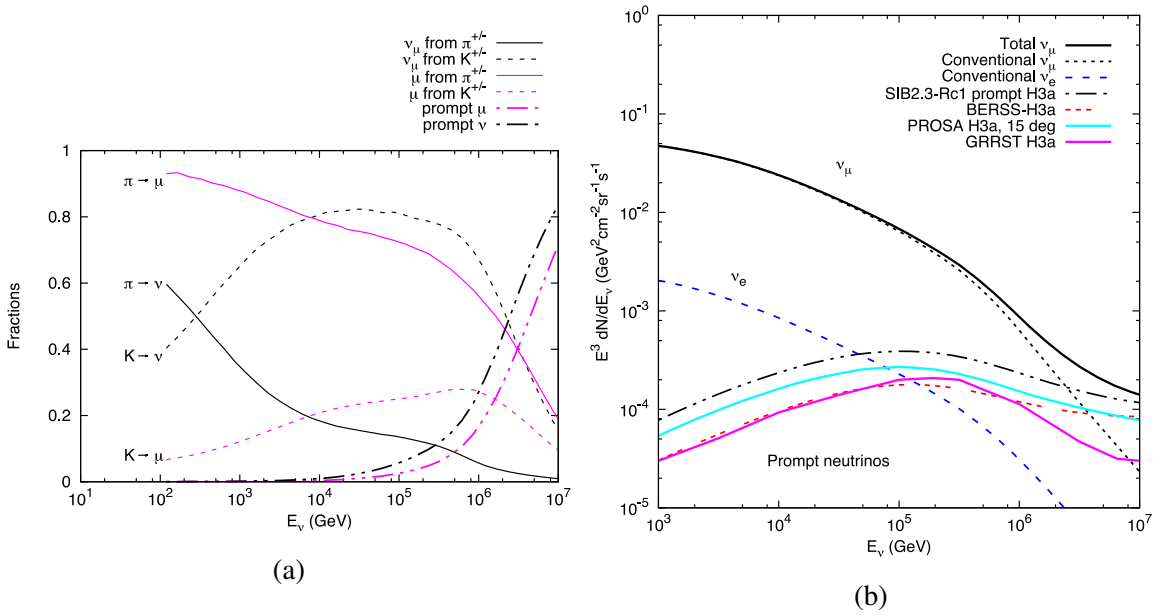

(a) (b)

Figure 1.5: (a) Fraction of neutrinos and muons produced by pion decay and kaon decay, as a function of energy. (b) The expected zenith-averaged atmospheric neutrino flux for muon neutrinos and electron neutrinos. Both the conventional flux and the prompt flux are shown. Both figures are reproduced from [20]

in Figure 1.5b, each labeled by the name of the model. It can be seen that the flux predictions vary from model to model, because the data for the heavy charmed meson is limited. Prompt neutrinos have not been detected and it is an active research topic in IceCube.

1.7 Neutrino Astronomy: Current Status

Astrophysical neutrinos have been discovered [21], and the diffuse astrophysical neutrino flux has been measured by the IceCube Neutrino Observatory [22][23]. IceCube has performed multiple measurements with different techniques for the diffuse flux. Here I will describe two measurements, one using muon neutrino events and one using high-energy starting-events (HESE). The first measurement selected through-going track events (see chapter 3) that came from the northern sky [24]. By restricting the events to come from the northern sky, it used the Earth as a shield to filter atmospheric muons. The sample is highly pure of muon neutrinos. Using a likelihood method, the best-fit for the astrophysical muon

neutrino flux was found to be

$$\frac{d\Phi_{\nu_\mu+\bar{\nu}_\mu}}{dE} = 1.44 \times 10^{-18} \left(\frac{E}{100\,\mathrm{TeV}}\right)^{-2.28} \mathrm{GeV}^{-1}\,\mathrm{s}^{-1}\,\mathrm{cm}^{-2}\,\mathrm{sr}^{-1}. \tag{1.25}$$

In the second measurement , the selection scheme employed a self-veto technique which use the outer part of the detector to remove contamination from atmospheric muons (see chapter 5), and an energy threshold of 60 TeV is placed on the reconstructed deposited energy [23]. This event sample mostly consisted of neutrino events with their interaction vertices inside the detector, and showed weaker bias towards different flavors. Thus, the flux calculated from this sample can be considered all flavors. Assuming an even flavor mixing (i.e., 1:1:1), the per-flavor diffuse neutrino flux is

$$\frac{d\Phi_{\nu+\bar{\nu}}}{dE} = 2.12 \times 10^{-18} \left(\frac{E}{100\,\mathrm{TeV}}\right)^{-2.87} \mathrm{GeV}^{-1}\,\mathrm{s}^{-1}\,\mathrm{cm}^{-2}\,\mathrm{sr}^{-1}. \tag{1.26}$$

Figure 1.6 from [25] is an attempt to interpret the role of the diffuse neutrino flux in the high energy universe. The two measurements of diffuse flux, from slightly older IceCube publications but consistent with this test, are plotted in the central region of, with the red line being the muon neutrino flux and the magenta line being the per flavor flux from the all-flavor measurement. On the right hand side of the same plot are the cosmic-ray measurement by Auger Observatory (green dots), and a model predicted cosmic-ray spectrum from extragalactic sources (green line). Calculating the Waxman Bachall limit (section 1.5) with this UHECR emission model will result in the green dashed line. The neutrino flux has almost saturated this limit, it could be a hint that the neutrinos detected by IceCube do share the same source with the UHECR.

On the left hand side of the plot are the isotropic gamma-ray background (IGRB) measured by Fermi Large Area Telescope (blue crosses), which is the gamma-ray flux from unresolved extragalactic sources. The solid blue line is the predicted observable gamma-ray flux produced by neutral pion decay, and is fitted to the IGRB data. This predicted flux

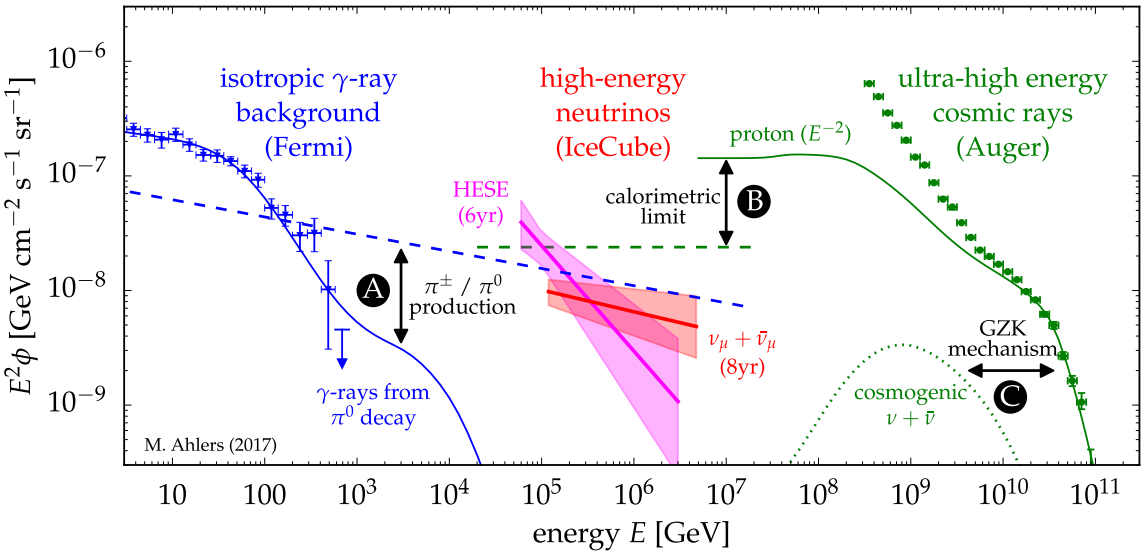

Figure 1.6: Spectrum of isotropic gamma-ray background (blue), neutrinos (red and magenta), and cosmic rays (green). Please see text for full description. Figure reproduced from [25].

can be converted into a neutrino upper limit in a way similar to the WB limit derived from UHECR spectrum. The conversion is performed by fixing the $\pi^{\pm}/\pi^0$ ratio and assuming the primaries have the same spectral index as the observed muon neutrino flux. This upper limit is shown as the blue dashed line. Once again, this limit is saturated by the diffuse neutrino flux. This observation could be suggesting that the neutrino sources indeed also are gamma-ray sources. However, if the diffuse neutrino flux in lower energy is found to be consistent with the HESE measurement (magenta line), it will significantly exceed the limit set by diffuse gamma rays. This would indicate the existence of gamma-dark neutrino sources.

1.7.1 Astrophysical Neutrino Source

Although IceCube has performed multiple searches for neutrino sources, none has returned a definite result. These searches covered objects like GRBs [26], flat-spectrum radio quasar (FSRQ)s, BL Lacs, AGNs, starburst galaxies, supernova remnants, and others [27][28]. Among all tested objects, two stands out from the rest with $\sim 3\sigma$ excess of neutrino signal,

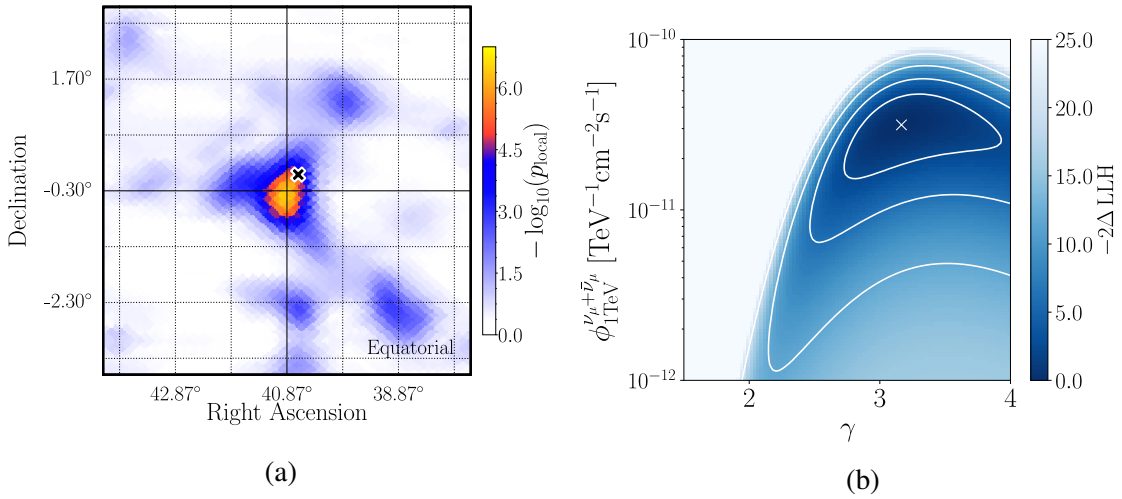

(a) (b)

Figure 1.7: (a) The significance (pre-trial) heatmap centered at the hottest spot of the all sky point source analysis. The location of NGC 1068 was marked with a cross. (b) The test statistic difference scanned over the parameter space for NGC 1068. Both figures are reproduced from [28].

which are the seyfert-II galaxy NGC 1068 and the blazar TXS 0506+056.

NGC 1068 was the most significant source in IceCube's time-integrated point source search using 10 years of muon neutrino data [28]. Among the list of 110 source candidates, NGC 1068 was observed with the highest significance, with a pre-trial p value of 4.1σ and post-trial p value of 2.9σ. It also coincided with the hottest spot in the all-sky scan. The significance heat map around the hottest spot was shown in Figure 1.7a, and the location of NGC 1068 was marked as a cross, which is 0.35^o away. The number of neutrino events coming from it was fitted to be 50.4, and the spectral index of the flux was fitted as 3.2. The parameter space was scanned and shown in Figure 1.7b.

TXS 0506+056's (TXS) story was very different and created a larger impact on neutrino astronomy in general. On 22 September 2017, IceCube detected a high energy neutrino from the direction of TXS. Upon the detection, IceCube issued an alert to the general astronomy community, which triggered a campaign of follow-up observations conducted by 14 observatories across different wavelengths [29]. Conincidentally, Fermi LAT observed TXS to be in a flaring state, and Major Atmospheric Gamma Imaging Cherenkov Tele-

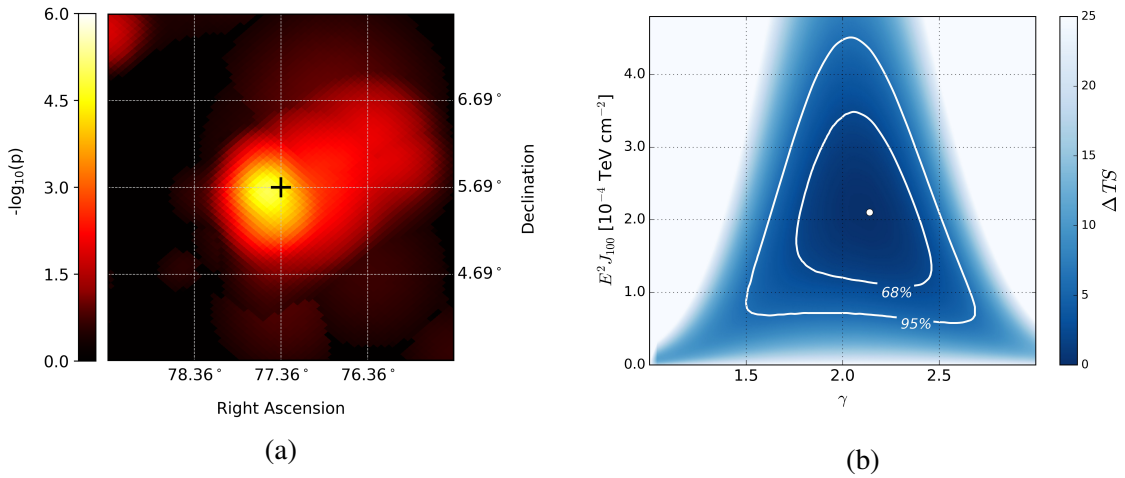

Figure 1.8: (a) The significance (pre-trial) heatmap centered at TXS 0506+056 of the time-dependent analysis. (b) The test statistic difference scanned over the parameter space of TXS 0506+056. Both figures are reproduced from [30].

scope (MAGIC) also observed VHE gamma rays from this source for the first time. The hypothesis that this coincidence happened by chance was rejected at a 3σ level significance [29]. The details of this campaign, including my contributions, will be discuss in detail in chapter 5.

After this event, IceCube also performed a time-dependent point source analysis at the location of TXS [30]. A neutrino flare was observed between September, 2014 and March, 2015. The flare was centered on 13 December 2014, and lasted for 158 days under a box-shaped emission model. An excess of 13 ± 5 events above the background expectation was observed in this flare, which result in a post-trial significance of 3.5σ. The pre-trial significance map centered at TXS and the test statistics scan over the parameter space were shown in Figure 1.8a and Figure 1.8b respectively.

1.8 Summary and Outlook

Although IceCube has yet to identify a neutrino source with 5σ significance, the results we gathered along the way have lightened up the paths forward. First, the diffuse neutrino flux measurement might allow us to interpret the point source search result in a more

comprehensive way. chapter 4 will focus on a software, which I created, that can simulate neutrino sources distribution based on the diffuse neutrino flux, and how it has been applied to calculate a more realistic upper limit for a given population of sources.

Second, the story of TXS suggested a real-time multimessenger approach to the problem. Instead of accumulating neutrino data alone, this new approach focus on the multimessenger observation triggered by the transient behaviors of different astrophysical objects. The challenge imposed by the lack of neutrino statistics could then be overcome by the coincidental observations in other messengers. This strategy echoed with the saturation of neutrino flux limits imposed by the gamma rays and cosmic rays. As discussed previously, the saturation suggested that UHECR, extra-galactic gamma rays, and the neutrinos detected by IceCube could very well be originated from the same population of sources. Therefore, a neutrino event would very likely to be accompanied by another messenger. In this sense, a quick and reliable alert system is of utmost importance. Thus, IceCube has upgraded its real-time neutrino alert system to promote follow-up observations by other observatories. The new system and my contribution to it will be discussed in detail in chapter 5. Likewise, the analysis performed by IceCube should also include more information obtain from other messengers, such as variation in certain EM spectrum. chapter 6 will be dedicated to my time-dependent point source analysis on X-ray binaries, which uses the orbital parameters from various EM measurements to improve its sensitivity.

CHAPTER 2
NEUTRINO PHYSICS AND DETECTION

2.1 Basic Properties

Neutrinos are the electrically neutral members of the lepton group in the standard model. All neutrinos have a lepton number equals to 1. There are three discovered flavors of neutrinos, electron, muon, and tau, correspond to the three flavors of the charged leptons with the same names. There could be other neutrino flavors, such as the proposed sterile neutrino, but there is no conclusive evidence for its existence yet [31].

The antiparticles of neutrinos are known as antineutrinos. They also have zero electrical charge, half-integer spin, and come in three flavors. However, their lepton numbers have the opposite sign as their neutrino counterparts. Another property that differentiates neutrinos from antineutrinos is the chirality. All neutrinos are left-handed and all antineutrinos are right-handed. This is the first known violation of the parity symmetry [32]. In the current understanding, neutrinos are not massless particles, but the exact values of their masses remain undetermined. Instead, upper bounds for them have been set by various experiments. For example, the 90% CL upper limit on electron-neutrino's mass is derived to be 1.1 eV [33], which is 5 orders of magnitude lighter than the mass of an electron.

2.2 Neutrino Oscillation

Neutrinos having mass is deduced from the phenomenon known as neutrino oscillation, in which neutrinos change their flavors from one to another along propagation. This effect has been observed and verified in neutrinos of different origins, such as solar [34], atmospheric [35], reactor [36], and particle accelerator [37]. IceCube has also observed neutrino oscillations in neutrinos with energies between 6 and 56 GeV [38]. This phenomenon arises from

the fact that the neutrino flavor eigenstates are mixed states for the propagation operator,

$$|\nu_\alpha\rangle = \sum_{i=1}^{3} U_{\alpha i}^{*} \, |\nu_i\rangle \, , \tag{2.1}$$

where ν_α are the flavor state, and α can be e, μ, or τ. U is the lepton mixing matrix, or PMNS matrix [39]. ν_i (i = 1,2,3) are the eigenstates of the propagation operator, also known as the mass eigenstates, and each has a definite mass m_i. The differences between m_i cause the mass eigenstates to propagate with different frequencies, which result in a non zero probability of a flavor state changing to another after a propagation length of L,

$$P_{\alpha\to\beta}(L) = |\langle\nu_\beta(L)|\nu_\alpha\rangle|^2 = |\sum_{i=1} U_{\alpha i}^{*} U_{\beta i} e^{-i\frac{m_i^2 L}{2E}}|^2. \tag{2.2}$$

Since the masses of the mass eigenstates are unknown, if we choose m_1 to be the lightest mass, there are two possibilities. The first one is normal ordering (NO), in which $m_1 < m_2 < m_3$. The second one is inverted ordering (IO), in which $m_1 < m_3 < m2$. This is known as the mass hierarchy problem. However, The mass differences $\Delta m_{ij}^2 = m_i^2 - m_j^2$ have been obtained by a global analysis using neutrino data from different experiments [3]. For NO, $\Delta m_{21}^2 = 7.55 \times 10^{-5}\,\mathrm{eV}^2$ and $\Delta m_{32}^2 = 2.42 \times 10^{-3}\,\mathrm{eV}^2$. For IO, $\Delta m_{32}^2 = -2.50 \times 10^{-3}\,\mathrm{eV}^2$.

For illustration purposes, it is useful to consider a two-flavor scenario, in which Equation 2.2 can be further rewritten as

$$P_{\alpha\to\beta}(L) = \sin^2(2\theta)\sin^2\left(\frac{\Delta m^2 L}{4E}\right), \tag{2.3}$$

where θ is the mixing angle between the two eigenstates. Equation 2.3 shows that the probability of flavor transition varies as a sinusoidal function of the ratio between the propagation length and energy of the neutrino, i.e. oscillates as L/E changes, and the frequency of the oscillation is controlled by Δm^2. It must be noted that this two-flavor model is also

applicable to many real-world neutrino experiments, such as atmospheric neutrino oscillation [40], where the oscillations of electron neutrinos are negligible, and only $\nu_\mu \leftrightarrow \nu_\tau$ is considered. The reason for the two-flavor model to work is that one of the mass differences are much smaller than the other two, so the three-flavor model can be approximated by a two-flavor model for small L/E.

When neutrinos propagate in a dense medium, electrons in the matter can change the propagation with charged current forward scattering with electron neutrinos (see definition for charged current in the next section). The change in the propagation Hamiltonian results in a change in the effective mass of the neutrino mass eigenstates. Thus, neutrino oscillations are modified in the dense medium. This is known as the Mikheyev–Smirnov–Wolfenstein (MSW) effect [41][42]. This effect may explain the large mixing angle problem of solar neutrino oscillations.

Neutrinos are still surrounded by open questions. These include but not limited to: the existence of the fourth flavor, the possibility of CP-violation in neutrino oscillations, the possibility of neutrinos being Majorana fermions, the ordering of the mass eigenstates, and the exact value of the neutrino mass.

2.3 Neutrino Interaction with Matters

Neutrinos can interact via weak interaction and gravity. For practicality, we will consider only the weak interaction (or electroweak interaction) between neutrinos and matters. In general, most weak interactions can be separated into two types, namely, charged current (CC) and neutral current (NC). In CC interactions, the interaction is mediated by a $W^\pm$ boson and the outgoing particles always include a charged lepton of the same flavor as the incoming neutrino (anti-lepton for antineutrino), i.e.,

$$\nu_l + N \to l + X. \tag{2.4}$$

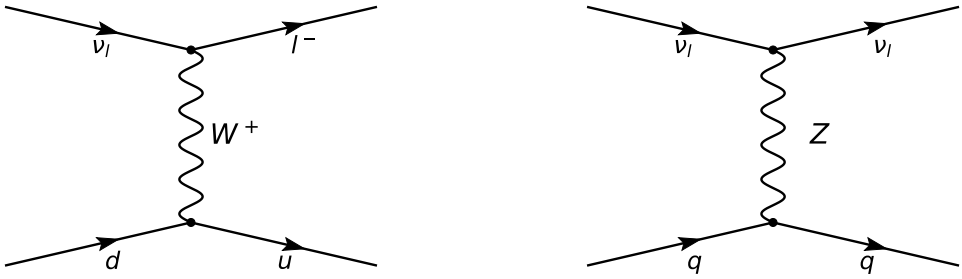

(a) (b)

Figure 2.1: Examples of (a) charged current interaction, and (b) neutral current interaction, between a neutrino and a quark. Please note the change of flavor from a down quark into an up quark after the interaction.

For NC interactions, the Z boson is exchanged to mediate the interaction, and among the products a neutral neutrino of the same flavor as the incoming neutrino can be found, i.e.

$$\nu_l + N \rightarrow \nu_l + X \tag{2.5}$$

In the equations listed above, N and X are nucleons, but the interactions between neutrinos and charged leptons can also be expressed in a similar fashion. Figure 2.1 shows an example Feynman diagram for each type of interaction between a neutrino and a quark.

For neutrinos in the energy range above a GeV, scattering of different categories can happen between neutrinos and nucleons, such as elastic scattering, resonance production, and deep inelastic scattering [43]. The cross sections for these processes scale differently with the neutrino energy. In the energy range of 20 GeV and above, which is the regime of interest for astrophysical neutrinos, deep inelastic scattering (DIS) dominates the interaction. In a DIS, neutrinos are scattered off by individual quarks instead of the composite nucleons, as a result, the nucleon can be broken apart to form a hadronic shower. Figure 2.2 from [44] shows the Feynman diagram of a CC DIS, in which a charged lepton is produced as the scattering product. If the DIS is NC, the Z boson will be exchanged instead of the $W^{\pm}$, and the product will include a neutrino instead of a charged lepton. From the experimental point of view, the information of the scattering can be deduced from both the

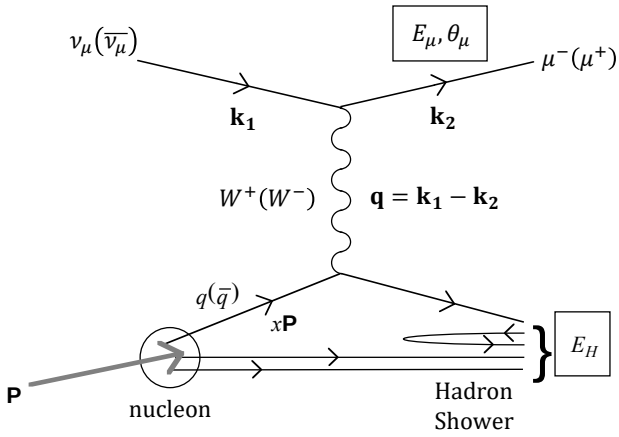

Figure 2.2: Feynman diagram of a CC type deep inelastic scattering. Figure is reproduced from [44]

charged lepton and the hadronic shower in a CC DIS, but only from the hadronic shower in the NC DIS.

The CC and NC inclusive DIS cross sections between a neutrino and an isoscalar nucleon (one with equal number of up and down quarks), according to [45], are given by:

$$\frac{d^2\sigma}{dxdy} = \begin{cases} \dfrac{2G_F M E_\nu}{\pi}\left(\dfrac{M_W^2}{Q^2+M_W^2}\right)^2 \left[xq(x,Q^2) + x\bar{q}(x,Q^2)(1-y^2)\right], & \text{(CC)} \\ \dfrac{G_F M E_\nu}{2\pi}\left(\dfrac{M_Z^2}{Q^2+M_Z^2}\right)^2 \left[xq^0(x,Q^2) + x\bar{q^0}(x,Q^2)(1-y^2)\right], & \text{(NC)} \end{cases} \tag{2.6}$$

where G_F is the fermi constant, M is the mass of the nucleon, $M_{W/Z}$ is the mass of the $W(Z)$ boson, E_ν is the energy of the neutrino, and $Q = -q^2$ is the invariant momentum transfer between the neutrino and the outgoing lepton, i.e. squared-4 momentum. x and y are the Bjorken scaling variable and inelasticity, defined as $x = Q^2/2M(E_\nu - E_l)$ and $y = (E_\nu - E_l)/E_\nu$ in the lab frame where E_l is the energy of the out-going lepton. $q^{(0)}(x,Q^2)$ and $\bar{q^{(0)}}(x,Q^2)$ are the parton distribution functions for quarks and antiquarks, respectively.

Using Equation 2.6, [45] calculated the cross sections for both neutrino and antineutrinos as functions of neutrino energy using CTEQ4[46], the result is shown in Figure 2.3. It can be seen that for both neutrinos and antineutrinos, the cross section scales linearly as the

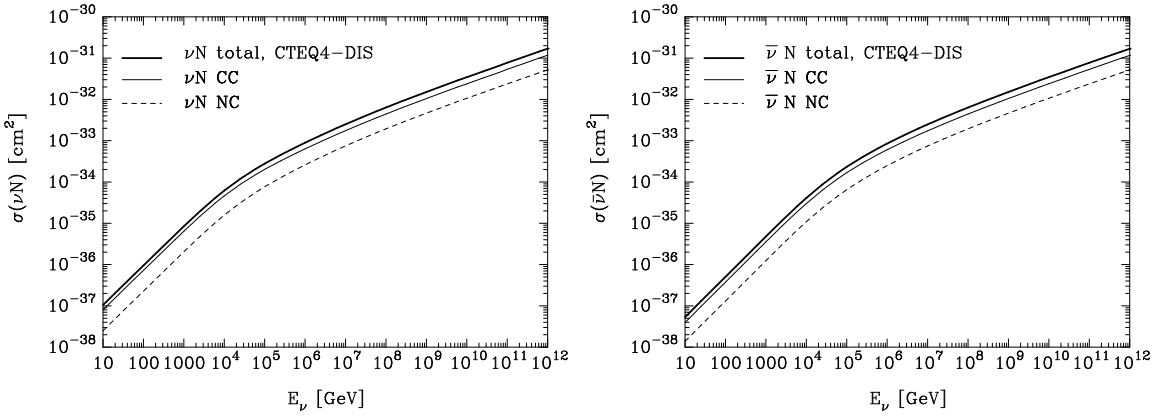

(a) (b)

Figure 2.3: Deep inelastic scattering cross section as function of neutrino's energy for (a) neutrino, and (b) antineutrino. Figure is reproduced from [45].

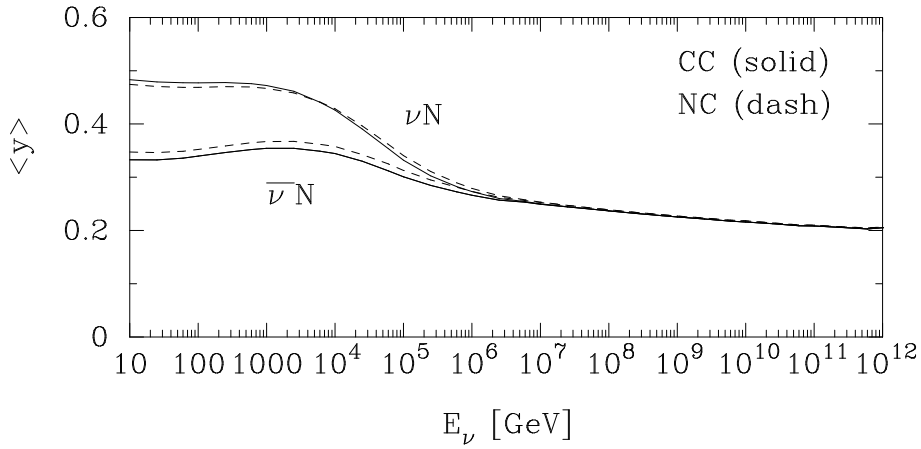

Figure 2.4: Mean inelasticity parameter y of deep inelastic scattering via CC and NC as a function of the neutrino energy. Figure reproduced from [48].

neutrino energy when it is below 10^4 GeV. The growth slows down afer 10^4 GeV due to the increase of the Q^2 factor in the denominator of the propagator in Equation 2.6. This result means that earth will eventually become opaque to neutrinos when the neutrino energy increases. Indeed, [47] showed that for neutrinos at 1 PeV to travel along the diameter of the Earth, about 75% of the particles would be absorbed during the propagation.

Figure 2.4 shows the mean inelasticity parameter y as a function of the neutrino (antineutrino) energy. The inelasticity parameter represents the fractional energy loss of the incoming neutrino. Thus, we can see that at about 10 GeV, the outgoing lepton retains at

least 50% of the incoming neutrino energy. Moreover, the squared momentum transfer Q^2 can be written as

$$Q^2 = -(k_1 - k_2)^2 \approx 4E_\nu E_l \sin^2(\theta/2), \tag{2.7}$$

where θ is the scattering angle of the outgoing lepton. For ultra high energy neutrino DIS, the typical value for Q^2 is $M_{W,Z}^2 \approx 6 \times 10^3\,\mathrm{GeV}^2$ [49]. Although the value of inelasticity fluctuates by a considerable amount, the average angle between a muon and a muon neutrino can be approximated as $0.7^o(E_\nu/\mathrm{TeV})^{-0.7}$ [50], i.e., the product muon from a 1 TeV ν_μ will be scattered by about 0.7 deg, while one from a 100 TeV ν_μ will be scattered by merely 0.03 deg.

In the discussion above, we have ignored neutrino-electron scattering, because the the cross section for this process is about 4 orders of magnitude smaller than that of DIS [43]. However, when an electron antineutrino has a energy of about 6.3 PeV, resonance can happen between it and an electron to produce a W^- boson, i.e.,

$$\bar{\nu}_e + e^- \rightarrow W^- \rightarrow X\,. \tag{2.8}$$

This phenomenon is known as the Glashow resonance (GR) [51]. For a narrow energy range centered at 6.3 PeV, the cross section of $\bar{\nu}_e\, e$ can be almost 100 times larger than that of DIS. IceCube has detected a Glashow resonance candidate [52]. That event deposited 6.05 PeV into the detector, and the neutrino was inferred to have an energy of 6.3 PeV. The detection of GR can be used to measure the $bar\nu_e$ flux to total neutrino flux ratio, which depends on the neutrino production mechanism at the source. For example, the ratio is predicted to be $0.17 : 1$ for pp interaction without muon damping, and $0.074 : 1$ for $p\gamma$ [53]. Nevertheless, the detection of GR is an important step for neutrino astronomy.

2.4 Early Detection Techniques

Neutrinos are notoriously difficult to detect due to their extremely small cross section. When they were first postulated by Wolfgang Pauli in 1930 as an attempt to explain the beta decay spectrum while conserving energy [54], neutrinos were considered undetectable. The following years saw the discovery of neutrons by James Chadwick [55], and eventually Enrico Fermi adopted Pauli's concept into what is known as the Fermi Theory of Beta Decay in 1934 [56]. The theoretical model of neutrinos and their existence were accepted by the end of the 1930s, but the experimental detection was not achieved until 1956 by Frederick Reines and Clyde Cowan [57].

The early neutrino detection techniques involved using inverse beta decay, which has been realized as the scintillator method or radiochemical method. In the scintillator method used by Reines and Cowan [57], the goal was to prove the existence of (anti-)neutrinos by finding the signal from the inverse beta decay,

$$\bar{\nu}_e + p \rightarrow n + e^+. \tag{2.9}$$

They used a nuclear reactor as the source of antineutrinos and a tank of water to provide the protons for interaction. The product positron would annihilate with an electron quickly after its creation, and produce two gamma-ray photons. Cadmium nuclei, which were added into the target water, would be excited by the neutrons and release gamma-ray photons, i.e.,

$$n + {}^{108}Cd \rightarrow {}^{109m}Cd \rightarrow {}^{109}Cd + \gamma\,. \tag{2.10}$$

Liquid scintillator was added to the water to capture the gamma rays emitted by annihilation or by the excited cadmium. Then, the visible light emitted by the scintillator was detected with photomultiplier tubes (PMTs) installed inside the water tank. Due to the diffusion of neutrons, the gamma-rays emitted by neutron capture would be delayed compared to those

emitted by positron annihilation. Thus, an inverse beta decay would create a PMT signature of two consecutive pulses with a time-lag of a few microseconds. The uniqueness of this signature was proved to be very effective in suppressing the background. This technique was adopted by modern experiments such as KamLAND [58] to study neutrino properties with reactor neutrinos.

The Homestake experiment [34] was the first to measure the solar neutrino flux. It employed the radiochemical method which was based on the neutrino capture reaction of $^{3}7\mathrm{Cl}$

$$\nu_e + {}^{37}\mathrm{Cl} \rightarrow {}^{37}\mathrm{Ar} + e^{-}. \tag{2.11}$$

This reaction has a threshold neutrino energy of 0.813 MeV, so it is sensitive to neutrinos produced by $^{7}\mathrm{Be}$ and $^{8}\mathrm{B}$ in the solar proton-proton chain reaction. The neutrino flux was measured by collecting the argon gas produced from the reaction, which had a decay half-life of 35 days to provide enough time for exposure. In order to increase the sensitivity, there were two key design features for this experiment. First, it used 615 metric tons of tetrachloroethylene to provide a large number of target atoms for the neutrinos to interact with. Second, the experiment was conducted in a mine 1478 meters below the surface. The surrounding rock layer provided excellent shielding against cosmic rays, which could contaminate the result by photonuclear interaction. As a result, the solar neutrino flux was successfully measured, which led to the famous solar neutrino problem, and eventually the discovery of neutrino oscillations.

These methods were well suited for the goals of the experiments they were applied in, and delivered the wanted results. However, some of their weaknesses rendered them inadequate for neutrino astronomy. First, the directional information of the neutrinos cannot be reconstructed from their signal, so it is impossible to trace the origin of the neutrino flux. Second, these methods deal with energies at $\mathcal{O}(\mathrm{MeV})$, which is too low for astrophysical neutrinos. Lastly, the scaling is not economical. Due to the astronomical distance, the neutrino flux from objects outside the solar system can be orders of magnitudes smaller than

the flux from the nuclear reactor. To compensate for the smaller flux, one must scale up the volume of the interacting medium, but the cost to do that is impractical for the scintillator experiment or radiochemical experiment. Thus, all neutrino experiments involved in neutrino astronomy adopted the Cherenkov radiation method for detection.

2.5 Cherenkov Radiation

Cherenkov radiation is emitted by a charged particle moving through a medium at a speed faster than the phase velocity of light in that medium [59]. It is the EM wave analogy to the sonic boom generated by supersonic aircrafts. The Cherenkov photons are given off at an angle to the direction of travel of the charged particle, and the angle θ is given by

$$\theta = \arccos \frac{1}{n\beta}, \tag{2.12}$$

where n is the refractive index of the medium, and $\beta = v/c$ is the velocity ratio of the charged particle. To understand this equation, Figure 2.5 depicts the emission of Cherenkov radiation by a charged particle moving at $\beta = 1$ in a medium with $n = 1.33$. The wavefront of the Cherenkov radiation is formed by the envelop of the spherical waves emitted by the charged particle at each point on the path. The propagation of the wavefront will form a conical volume around the charged particle's travel direction. Cherenkov photons can be detected only within this volume.

The threshold energy of the charged particle for Cherenkov radiation to occur can be easily derived using $E^2 = p^2c^2 + m^2c^4$ and $v = c/n$, which is

$$E_{thres}(n, m) = mc^2 \frac{n}{\sqrt{n^2 - 1}}, \tag{2.13}$$

where m is the rest mass of the particle. For example, for a muon ($m = 105.658\,\mathrm{MeV}/c^2$) to emit Cherenkov radiation in ice ($n \approx 1.31$), its energy must be at least 163.6 MeV. The energy emitted by the charged particle through Cherenkov radiation per unit length traveled

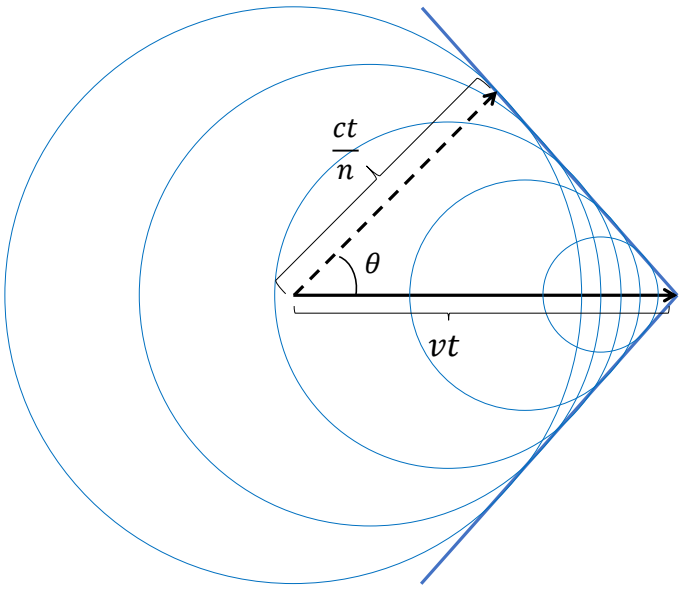

Figure 2.5: Illutstration of the Cherenkov radiation for the case $\beta = 1$ and $n = 1.33$. Using Huygen's construction, the Cherenkov wavefront is enveloping the the spherical waves emitted at each point along the path of the charged particle.

per frequency is given by the Frank-Tamm formula [60]

$$\frac{d^2E}{dxd\omega} = \frac{q^2}{4\pi}\mu(\omega)\omega\left(1 - \frac{1}{n^2(\omega)\beta^2}\right), \tag{2.14}$$

where E is the energy released as Cherenkov photons, x is the distance travelled by the charged particle, ω is the angular frequency of the photon, q is the charge of the particle, μ and n are the frequency-dependent permeability and refractive index of the medium, and β is the velocity ratio of the particle. With the factor of ω in the RHS of Equation 2.14, one may find the integral divergent when integrated over all possible ω. However, in practice, n becomes 1 or smaller as ω increases, thus preventing the divergence. As a result, the spectrum of the Cherenkov radiation usually peaks at ultraviolet and appears bluish to the naked eye.

Although neutrinos are neutral, the products of neutrino-matter interactions contain charged particles. The charged particles can be traced by implementing a dense array of PMTs to collect the Cherenkov photons emitted by them. First, using the locations and

times of the triggered PMT, the orientation of the Cherenkov light cone and the direction of the charged particle can be deduced. Second, by counting the number of photons and combining with Equation 2.14, the energy of the charged particle can be estimated. Finally, combing these two information with the known properties of neutrino scattering, the information of the neutrino can then be reconstructed. The actual reconstruction process varies from experiment to experiment, for the case of IceCube, it will be discussed in section 3.4.

Beside being able to reconstruct the information of the neutrino, another advantage of using Cherenkov radiation to detect neutrino is the ease of increasing the scale of the experiment. Since Cherenkov light is in the visible spectrum, it can be detected by PMT without scintillators. This unlocks the possibility of building neutrino detector around large volume transparent natural medium, such as sea or glacial ice.

CHAPTER 3
ICECUBE NEURINO OBSERVATORY

In order to study high energy neutrinos from extra-galactic sources, the idea of a 10 kiloton underground or underwater Cherenkov neutrino detector was first suggested in the 1950s [61]. The detectors were proposed to be incorporated into a large volume of natural medium to fulfill the size requirement. In the following decades, pioneer experiments such as DUMAND [62], AMANDA [63], ANTARES [64], and Lake Baikal Neutrino Experiment [65] demonstrated the feasibility of neutrino detection and reconstruction with natural interaction medium. Although they failed to identify the cosmic neutrino flux, they laid the foundation for neutrino astronomy by providing valuable insights and techniques to the field. With the goal of discovering the elusive cosmic neutrino, a cubic-kilometer scale detector was proposed in the 1990s [66]. The realization of this idea is the IceCube Neutrino Observatory.

3.1 IceCube

IceCube Neutrino Observatory is situated at the geographical south pole. The main detector, IceCube, consists of 5160 Digital Optical Modules (DOMs) buried in the Antarctic ice. Each DOM houses a 10-inch PMT and necessary electronic components. They are the fundamental detection unit of the experiment. More detail of the DOM is discussed in subsection 3.3.1. The DOMs are deployed as an array of 86 vertical strings, and each string has 60 DOMs attached to it. The strings are placed in a network of hexagonal patterns. Figure 3.1 shows the detector layout. 78 of the 86 strings forms the primary in-ice array. In these strings, the vertical separation between each pair of DOMs is 17m. The presence of the DOMs spans from 1450m to 2450m below the ice surface, and with a horizontal inter-string spacing of 125m, the entire array has an instrumental volume of roughly 1 cu-

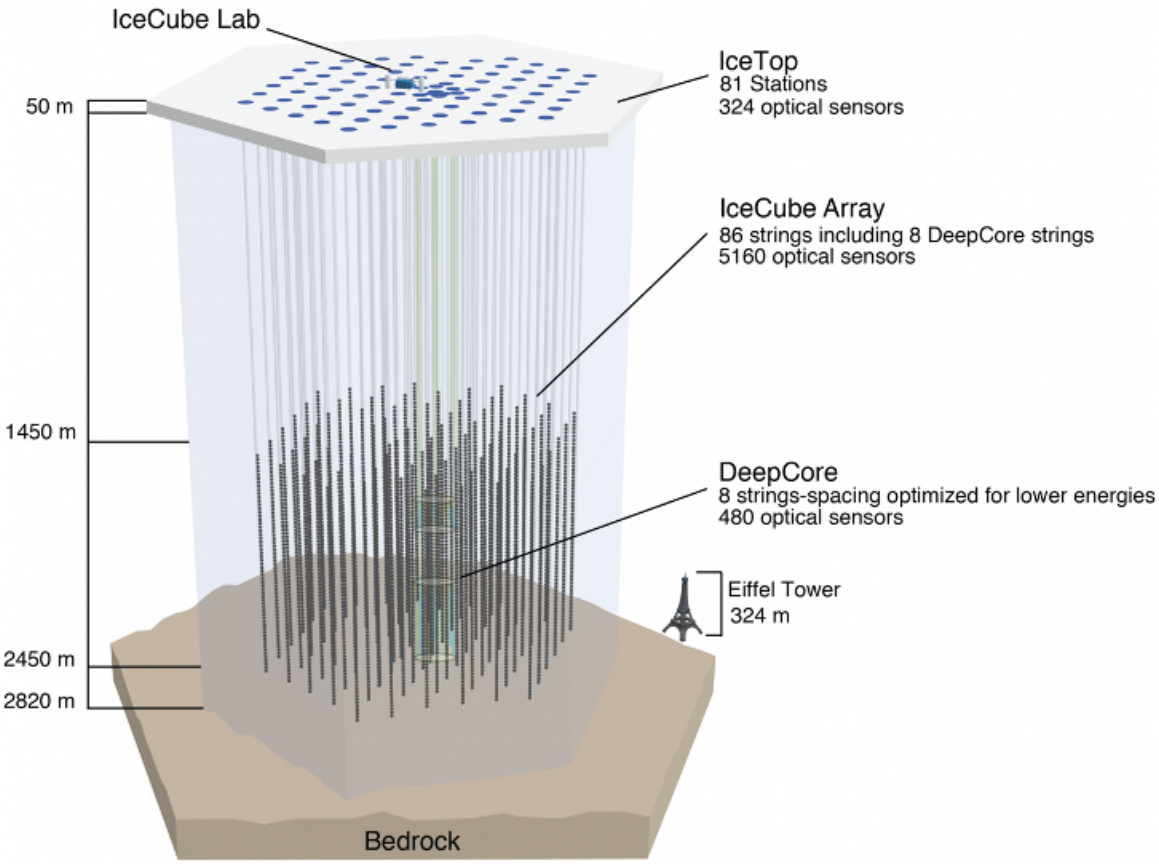

Figure 3.1: Diagram of the IceCube Neutrino Observatory. Image by the IceCube Collaboration.

bic kilometer. The remaining 8 strings form a subarray known as the DeepCore. Most of the DOMs on these 8 strings have a higher quantum efficiency than those in the primary array. For each string, the bottom 50 DOMs are placed at a depth from 2100m to 2450m with a vertical spacing of 7m. Another 10 DOMs are placed 10m apart each other between 1910m to 2000m. The spacing between these 8 strings are also different, ranging from 42m to 105m. Altogether, DeepCore has a higher DOM density than the rest of the detector. The primary in-ice array targets astrophysical neutrinos in the energy range from $\mathcal{O}(\mathrm{TeV})$ to $\mathcal{O}(\mathrm{PeV})$ while DeepCore is optimized for neutrinos with energy 10 to 100GeV, which are important in studies like neutrino oscillation, dark matter annihilation, and galactic supernovae.

Above the glacial ice, there is another array of DOMs in the snow layer known as IceTop. IceTop is an air shower detector which mainly focuses on detecting cosmic ray events. It consists of 81 stations located approximately at the top end of the strings. Each station accommodates two ice tanks, and each tank has two standard IceCube DOMs installed inside. In a similar fashion to DeepCore, the eight stations in the center of IceTop also form a denser infill region. IceTop is sensitive to cosmic rays in the energy range of PeV to EeV, and the infill region's enregy threshold is lowered to 100 TeV. Thus, it covers the energy range between the knee and slightly below the ankle of the cosmic-ray spectrum. In addition to acting as a cosmic rays detector, IceTop can also serve as a veto for the in-ice array by finding events in temporal coincidence with IceCube. This technique can effectively suppress the contamination from atmospheric muons and atmospheric neutrinos in the southern sky [67].

Finally, on the surface and at the center of the array, sits the main building of IceCube Laboratory (ICL). It serves as the counting house for the experiment and collects data from both the IceCube and IceTop arrays. The computer servers in the building are responsible for the data acquisition, initial process and filtering, and data storage before the data are sent to the north.

3.2 Signal Classification

IceCube uses the glacial ice as the target for the incoming neutrinos. The array of DOMs are implemented to capture the Cherenkov photons given out by the product of neutrino-ice interaction. The signal that is observed by the DOMs depends on a list of factors, including the flavor of the neutrino, the type of the weak interaction, and the location of interaction vertex. Thus, it is useful to go through the possible different signal topologies in IceCube.

3.2.1 Muon Neutrinos

Among the three flavors, muon neutrinos are the bread-and-butter for neutrino astronomy because of the penetrating power of muons, which makes the precise pointing of the neutrinos possible. When a muon travels through ice, it can lose energy through: ionization, bremsstrahlung, electron-positron pair production, and photonuclear interactions. The contribution from ionization depends weakly on the muon energy, while the contribution from the radiative processes increases linearly with the energy. Although the radiative processes happen in a stochastic fashion, an averaged continuous loss can be calculated using Monte Carlo method. This has been done by [68], and the energy loss per grammage, which is also known as column density and is defined as density$\times$length, is shown in Figure 3.2.

The total energy loss per unit length travelled by the muon can be approximated by

$$-\frac{dE_\mu}{dx} = a + bE_\mu, \tag{3.1}$$

where E_μ is the energy of the muon, x is the distance travelled by the muon, a and b are the coefficients for ionization and radiative processes respectively. The value of a and b for ice are also provided by [68], and after adjusting with the ice density, they are $a = 0.246\,\mathrm{GeV\,m^{-1}}$ and $b = 0.432\,\mathrm{m^{-1}}$. By integrating Equation 3.1, the average range of the muon as a function of the initial energy can be estimated. For example, an 1 TeV muon will have a range of about 1.8 km while a 100 TeV muon will have a range of about 10

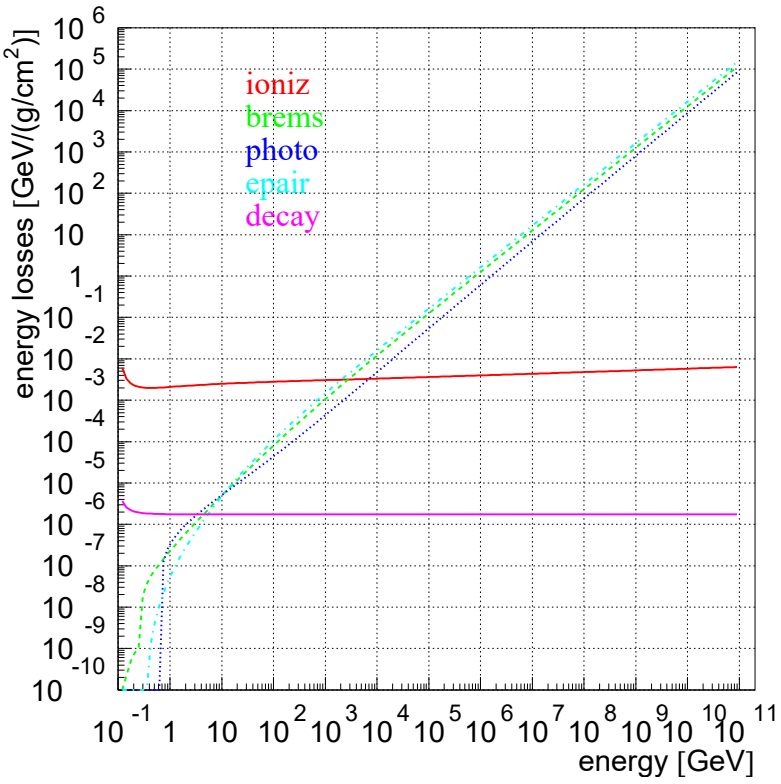

Figure 3.2: Muon energy loss per grammage by different processes in ice. Figure reproduced from [68].

km. The extensive range of muon allows IceCube to detect ν_μ via CC interaction even if the interaction happens far away from the instrumented volume.

If the CC interaction happens outside the detector, but the high energy muon travels through the detector, the Cherenkov photons emitted along the path will trigger the DOMs. Because of photon scattering and absorption by ice, the Cherenkov light cannot propagate too far from the muon's trajectory. The resultant pattern of the triggered DOMs will be linear along the muon's path and is classified as a through-going track event. Figure 3.3a shows an example of through-going track. Instead, if the interaction happens inside the detector, Cherenkov photons from both the outgoing muon and the hadronic shower will be registered by the DOMs. In such case, the signal is classified as a starting track event.

For a muon neutrino NC interaction, the Cherenkov photons will be coming from the hadronic shower only. However, the products in the shower decay quickly, so they cannot emit photons along an elongated path. Moreover, the hadronic shower is small compared to the DOMs' spacing, it can be considered as a point source of light. As a result, the DOMs will be triggered in a spherical pattern. This type of signal is known as a cascade event. Figure 3.3b shows an example for a cascade event.

3.2.2 Electron Neutrinos

Unlike muon neutrinos, the incoming directions of electron neutrinos are more difficult to resolve due to the short range of electrons in ice. Although the energy loss mechanisms for electrons are the same as those for muons, the fractional energy loss by electrons in the stochastic processes is much larger because of its lower mass. The radiation length of electron is 0.39 m in ice [3], which is the length for the electron to lose $1 - e^{-1}$ of its energy [69]. Furthermore, when an electron loses energy through bremsstrahlung, the photons emitted will undergo electron-positron pair production, then the product electron and will lose its energies through bremsstrahlung again. This process goes on until the product electron's energy is below the critical energy and bremsstrahlung is no long the dominant

way of energy loss. The repeated pair production thus produce an electromagnetic shower.

The Cherenkov light emitted by such an electromagnetic shower also peaks at the angle given by Equation 2.12, because the electrons in the shower move in a similar direction to the initial one. However, the hadronic shower will also emit Cherenkov light, and it is nearly impossible to separate the contribution from both types of shower. As a result, both CC and NC electron neutrino interactions trigger the DOMs in a spherical pattern and are both classified as cascade events. Although their angular resolution is poor, cascade events allow a more precise energy reconstruction based on their size.

3.2.3 Tau Neutrino

The signal topologies of tau neutrinos are more complicated and energy dependent. Since taus have a short life time, they can only propagate a short distance before decaying. Their decay can produce another shower (either electromagnetic or hadronic). Given the short distance travelled by the tau, it is difficult to separate this shower from the one produced in the initial interaction. The differentiation is only possible when the tau neutrino has about 100 TeV energy. In that case, the PMT pulse produced by the shower (either electromagnetic or hadronic) from tau decay may be detected with a slight time delay after the pulse produced by the hadronic shower of the initial interaction, and thus creating a double-pulse event [70].

The decay length for tau as a function of energy is 50 meters per PeV energy [3], so it is possible for high energy taus to create a track-like signal in IceCube. There are many possible patterns formed by high energy taus, the most iconic one is a double-bang event, in which the hadronic shower and tau decay create two separated cascades connected by a track created by the tau propagation. The other decay possibilities such as $\tau^- \rightarrow \mu^- \bar{\nu}_\mu \nu_\tau$, will give rise to track-like events with varying brightness.

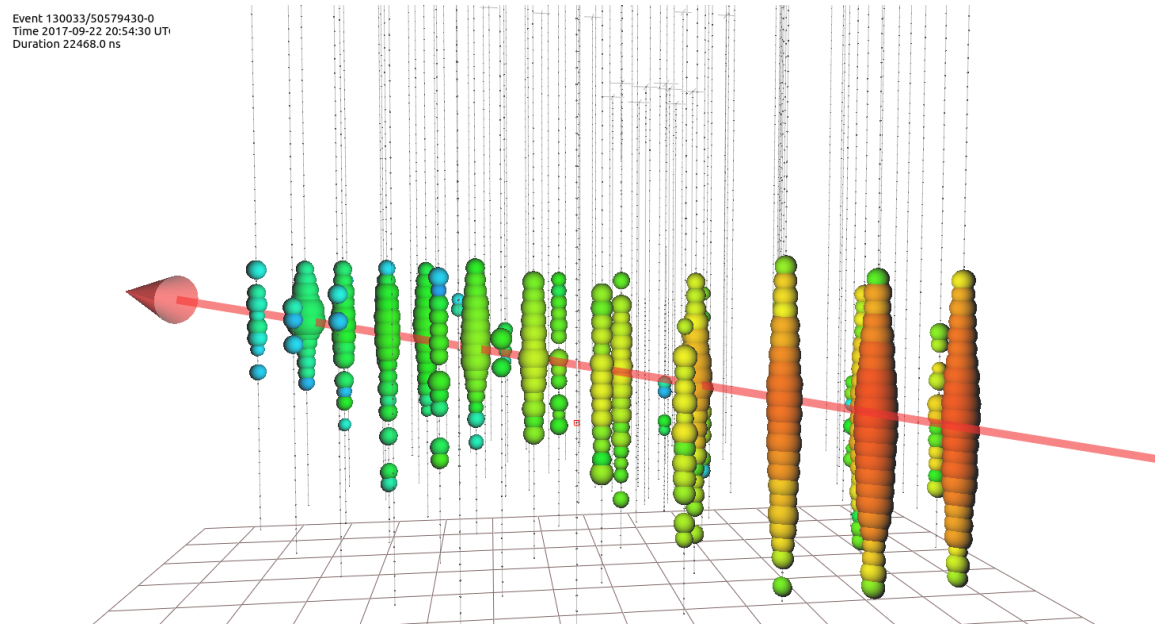

(a)

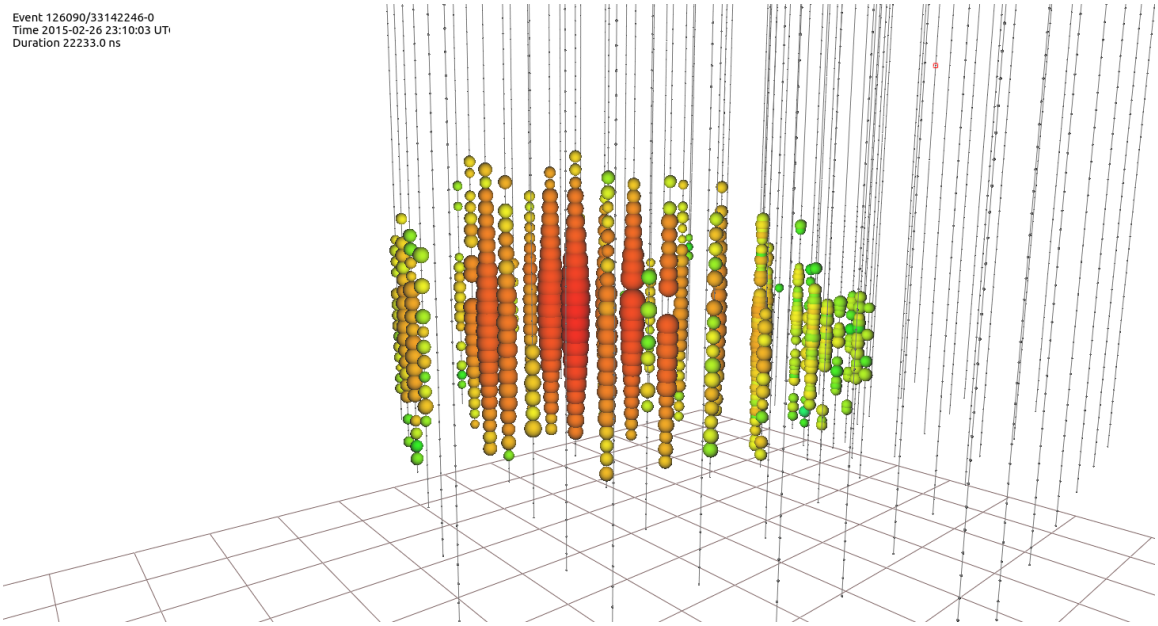

(b)

Figure 3.3: (a) An example of a through-going track event. (b) An example of a cascade event. In both figures, the DOMs that detected HLC pulses are represented by colored spheres. The color reflects the arrival time of the pulse; early pulses are in red while late pulses are in blue. The size of the sphere reflects the charge.

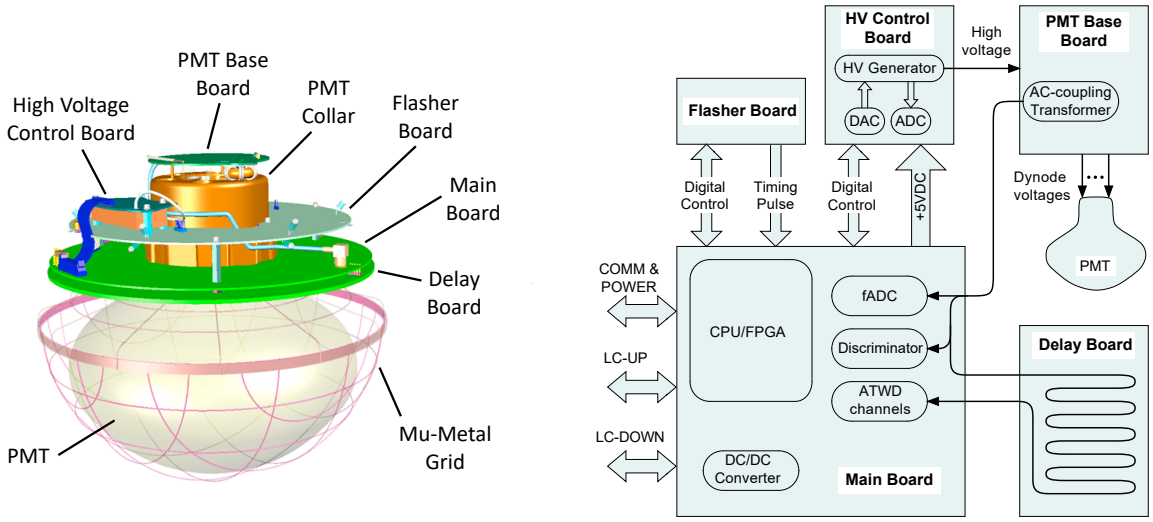

(a) (b)

Figure 3.4: (a) Internal components of a DOM. (b) Functional connections of different parts. Both figures reproduced from [71].

3.3 Data Acquisition

3.3.1 Digital Optical Modules

IceCube's data acquisition (DAQ) begins at 5160 digital optical modules (DOMs), which are the fundamental units for data acquisition. Every DOM contains a downward-facing 10"-PMT and circuit boards that are responsible for the operation, data acquisition, and calibration. All components are protected by a 0.5"-thick spherical low-potassium (to reduce noise from the radioactive decay of ^{40}K) glass housing. Each DOM is connected to the nearest neighbours with communication wires, which allow them to check for coincident detection. The components and circuit connection of a DOM are shown in Figure 3.4.

The PMTs in the standard DOMs are sensitive to wavelengths between 300 nm and 600 nm, and their quantum efficiency peaks at around 25% (34% for high efficiency DOMs) for 390 nm photons. The PMTs are tuned to operate at a gain of 10^7. If the analog waveform signal from the PMT passes the voltage threshold (corresponds to 0.25 PE) of the discriminator, it will be digitized by the Analog Transient Waveform Digitizer (ATWD) and the

fast Analog-to-Digital Converter (fADC) installed on the main board. The main board has two ATWDs working alternately to reduce the deadtime due to its readout. The ATWD has a recording duration of 427 ns and samples at a frequency of 300 Msps. The fADC's recording duration is about 15 times longer at 6.4 μs, but has a sparser sampling rate of 40Msps. The short recording duration of ATWD could be insufficient to capture the entire PMT signal if the photons experienced severe scattering, so fADC is used to complement this weakness with its 6.4 μs recording period.

The main board also contains a 40 MHz crystal oscillator, which serves as the timing device for the DOM. When the converters are launched, the oscillator will provide a local timestamp. The information of the digitized waveform (which can be the full waveform or just the charge summary) with the timestamp together are recorded as a "hit", which will then be sent to the surface. The translation from a DOM timestamp to a IceCube Laboratory timestamp is achieved using the RAPCal algorithm [71]. The uncertainty of this translation is about 1.2 ns. The ICL timestamp can then be converted to a Coordinated Universal Time (UTC) provided by the ICL masterclock.

3.3.2 Local Coincidence and Trigger

PMTs are susceptible to dark noise, i.e., photoelectrons emitted from the cathode without a light source external to the DOM. There is a zoo of possible sources for dark noise, such as thermionic emission, luminescence in the glass housing, radioactive decay, etc. The average hit rate for the in-ice DOMs due to dark noise is 560 Hz per DOM, which poses a heavy burden to the cable bandwidth. Thus, the full waveform of the PMT pulse will be stored only if the hit satisfies the local coincidence criteria (LC) to reduce the data transmission. The LC requires there to be another hit detected by a nearest neighbour or next-to-nearest neighbour DOM within 1 μs of the first hit. If LC is satisfied, both hits will be marked as hard local coincidence (HLC) hit. If LC is not satisfied, the signal digitization will be aborted at 2.4 μs , and the hit will be marked as a soft local coincidence (SLC) hit.

SLC hits contain only the charge summary and the timestamp. The major source of HLC hits is cosmic ray muons, so the HLC rate depends on the depth of the DOM. The average rate per DOM decreases from 25 Hz at the top to 5 Hz at the bottom.

To further suppress the impact of dark noise, IceCube's DAQ system looks for clusters of HLC hits that satisfy predefined geometric or temporal criteria known as triggers. The triggered hits will be used to reconstruct the particle event detected by IceCube. The fundamental triggers used by IceCube are of type simple multiplicity trigger (SMT). SMT requires N HLC hits within a time window of $t\mu$s, with no geometric requirement imposed. The trigger duration will be extended as long as there is a new HLC hit that happens within $t\,\mu$s after the initial trigger. The The number of N and t depends on the array of the hit DOMs belong to. For the in-ice array, $N = 8$ and $t = 5$, so the trigger is known as SMT8. SMT8 has an average rate of 2100 Hz, which is mainly caused by cosmic ray muons, so the rate shows seasonal fluctuation.

Beside SMT, there are other types of triggers, such as Volume trigger, String trigger, and SLOP trigger. These triggers require the HLC hits to satisfy sets of spatial criteria, on top of the criteria on the number of hits and time. They are designed for events that might be missed by the SMT, like low energy events (Volume) or vertically going events (String). The details on these triggers can be found in [71]. Since the hits from a single event can sometimes satisfy multiple triggers, it is of importance to merge these triggers together to avoid multiple counting of the same event. In order to do so, the DAQ system identifies all triggers that are overlapping in time, then creates a single readout window that envelops all triggers, which is known as the Global Trigger.

Hits that are inside the Global Trigger readout window will be gathered to build an IceCube event, which will then be passed to the Processing and Filtering (PnF) system. It should be noted that multiple events are frequently grouped together in a single Global Trigger. These coincident events, e.g., two independent cosmic ray muons, will be separated by the splitting step in PnF.

3.3.3 Processing and Filtering

The communication between IceCube Laboratory and the main data warehouse in Wisconsin relies on satellite. The major role of the PnF system is to utilize the allocated bandwidth of the satellite, so it is tasked to reduce the size of the data and select interesting events. Processes that will be applied to the events include: DOM calibration, data compression, event and trigger splitting, hit cleaning, reconstruction, and event selection (filtering). After these steps, the events will be ready for transmission. It should be noted that the fast processing at South Pole has proven to be scientifically valuable, as it currently reduces more background events than what is needed to fit the data into the satellite bandwidth allocation.

The filters are different sets of event selection schemes, designed for different purposes. The lineup of the filers is reviewed every year, and new filters may be added if the need arises due to a new analysis. Some notable filters are

1. Muon Filter: its purpose is to remove cosmic ray muons from the data. It mainly selects upgoing track events, because cosmic ray muons are blocked by the Earth. Downgoing track events with high total PMT charge will also be selected, because they have a higher chance of being astrophysical neutrinos.

2. high-energy starting-events (HESE) Filter: it is designed to select neutrino events that have their interaction vertices inside the detector by using a self-veto technique. It also requires the events to have a large number of deposited charge, to further increase the chance for the events to have astrophysical origin. This filter will be discussed in detail in chapter 5.

3. Extreme High Energy (EHE) Filter: its goal is to select neutrino events above 1 PeV. This is done by requiring the events to have an extremely high total PMT charge.

There are other filters that are applied at South Pole, but they are beyond the scope of this work, so are omitted here. Some of the filters mentioned above are the fundamental components of IceCube's realtime alert system, which will be discussed in detail in chapter 5.

3.4 Event Reconstruction

The goal of event reconstruction is to obtain the properties of the particles that produce the signal detected by the DOMs. The properties of utmost importance to an astrophysics analysis are the direction, energy and identity of the particle. However, there are many technical challenges posing in this process. First, the propagation of Cherenkov photons in ice depends on the optical properties of the glacial ice, which is a major source of systematic uncertainties. Second, the Cherenkov photons can be emitted by both the muon and the shower products of stochastic energy loss. Third, some of the hits are contributed by dark noise, which would cause errors to the reconstructed values. Ideally, the computation time for reconstruction should be short, because many realtime event selections depend on the reconstructed observables. There are different reconstruction algorithms designed to tackle these challenges, but for the purpose of this work, this section will mainly focus on the reconstruction algorithm for through-going track events.

3.4.1 LineFit: First Guess Algorithm

The first step of a track reconstruction is the LineFit algorithm [24]. This algorithm assumes the hit at position $\vec{x}_i$ at time t_i satisfies the equation

$$\vec{x}_i = \vec{x}_0 + \vec{v}(t_i - t_0), \tag{3.2}$$

where $\vec{v}$ is the velocity of the charged particle, and $\vec{x}_0$ is some point the particle passed through at time t_0. In other words, the hits are assumed to follow closely the trajectory of the charged particle. In this method, the time of the first pulse in the DOM, i.e., the arrival time of the first photon, is used as t_i. This choice is based on the fact that the first photon reaching the DOM is most likely scattered the least, so the charged particle should be closest to the DOM at that time. The track is reconstructed by performing a least-squares

fit for

$$\min_{\vec{v},\vec{x}_0,t_0} \sum |(\vec{x}_i - \vec{x}_0) - \vec{v}\,(t_i - t_0)|^2\,, \tag{3.3}$$

which has an analytical solution.

The track direction obtained by Linefit is less accurate than more advanced techniques, because it disregards effects like the emission profile of Cherenkov cone and the photon scattering by ice. An improved version of Linefit (dubbed Improved LineFit) addresses the scattering effects by implementing two modifications. The first one is delay-hit cleaning, it checks for every hit h_i if there is another hit h_j within a distance of r meter that has a timestamp at least t nanosecond before that of h_i. h_i will be excluded from the reconstruction if the check is positive, because it indicates that h_i is caused by severely scattered photons. The second modification is to the least square fitting, which is changed to

$$\min_{\vec{v},\vec{x}_0,t_0} \sum \begin{cases} \rho^2 & \text{if } \rho < \mu \\ \mu(2\rho - \mu) & \text{if } \rho > \mu \end{cases} \tag{3.4}$$

where $\rho = |(\vec{x}_i - \vec{x}_0) - \vec{v}\,(t_i - t_0)|$, and μ is determined from simulation. This modification reduces the weights of the hits far away from the charged particle's trajectory, which are more likely to be caused by scattered photons, from quadratic to linear. The Improved LineFit method's results are not accurate enough for event selection or performing analysis, but they are good initial guesses (or seed tracks) for more sophisticated reconstruction methods.

3.4.2 Likelihood Reconstruction

The next step of the reconstruction begins to incorporate Cherenkov emission and ice properties into the light emission model. Since the Cherenkov photons are emitted at an angle θ_c, and the light propagation speed in ice c/n is slower than the speed of the charged particle $|\vec{v}| \approx c$, the earliest time for a photon to reach the DOM at $\vec{x}_{\mathrm{DOM}}$ should be given by

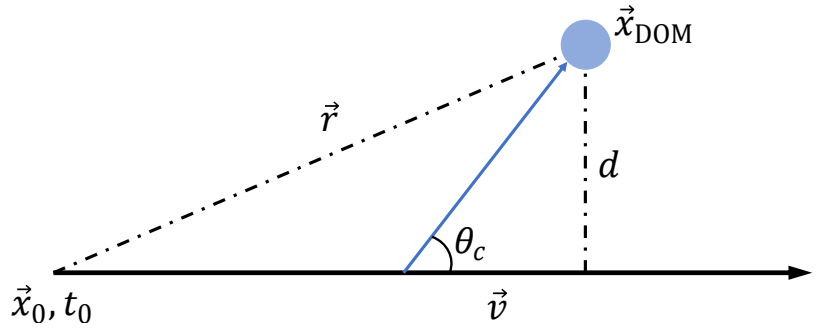

Figure 3.5: Schematic diagram of the Cherenkov light emitted by a track event reaching the DOM.

$$\begin{aligned} t_{\mathrm{min}} &= t_0 + \frac{(\vec{x}_{\mathrm{DOM}} - \vec{x}_0) \cdot \hat{v} - d\cot(\theta_c)}{|\vec{v}|} + \frac{d\csc(\theta_c)}{c/n} \\ &\approx t_0 + \frac{(\vec{x}_{\mathrm{DOM}} - \vec{x}_0) \cdot \hat{v} + d\tan(\theta_c)}{c}, \end{aligned} \tag{3.5}$$

where d is the impact parameter between the DOM and the track. Figure 3.5 illustrates the shortest path for a DOM to detect a Cherenkov photon. In practice, photons emitted at any point on the path must be scattered before reaching the DOM, so they cannot arrive at a time earlier than t_{min}. The difference between the hit arrival time t_{hit} and t_{min} is called the residual time t_{res}.

In the likelihood reconstruction method, the track parameters $(\vec{v}, \vec{x}_0, t_0)$ are determined by maximizing the likelihood function. $|\vec{v}|$ is assumed to be the speed of light, so only the direction of $\vec{v}$ is of importance. In the simplest formulation, the likelihood function is defined as

$$\mathcal{L}_{\mathrm{SPE}} = \prod_{i}^{\mathrm{N_{hits}}} p_1(t_{\mathrm{res},i} | \vec{v}, \vec{x_0}, t_0), \tag{3.6}$$

where p_1 is the probability distribution function (PDF) of the residual time. In IceCube, the first PDF used is known as the Pandel function (named after former Master student Dirk Pandel) [72], which is an analytical approximation to the true distribution of time delays caused by scattering. p_1 only takes the arrival time of the first photon (pulse) of each hit into account, so it is called the single photoelectron (SPE) PDF. A natural extension to the

SPE PDF is to take the first N photons of the hits into account, which is done by the multi photoelectron (MPE) PDF,

$$p_N^1(t_{\rm res}) = N p_1(t_{\rm res}) \left(\int_{t_{\rm res}}^{\infty} p_1(t) dt \right)^{N-1}. \tag{3.7}$$

The MPE PDF quantifies the probability of having 1 photon arrived with a residual time $t_{\rm res}$ and $N-1$ photons arrived after it. The MPE likelihood is given by

$$\mathcal{L}_{\rm MPE} = \prod_{i}^{\rm N_{hits}} p_N^1(t_{{\rm res},i} | \vec{v}, \vec{x_0}, t_0). \tag{3.8}$$

The results of the SPE and MPE reconstructions are usually used as the parameters in event selection and as seed tracks for the more advanced reconstruction method.

3.4.3 Ice Properties and Spline Reconstruction

As seen in the previous section, the understanding of the ice properties at South Pole plays an enormous role in the accuracy of the reconstruction. IceCube uses glacial ice of depth between 1450 and 2450 m as the interaction medium. It was formed from the snow that fell 25,000 to 100,000 years ago [73]. As a result, the dust and trapped air concentration in the ice varies from layer to layer, depending on the climate and volcanic activity at the time of formation. For example, the Toba super eruption caused a sharp increase in dust concentration at precisely 2146 m [73], and the most prominent spike in dust concentration, which happens between 1950 m and 2100m, is related to the second to last glacial maximum about 70,000 years ago [73]. Beside the climate variation, the ice layer is tilted due to the bedrock being non horizontal. As a result, the dust concentration is not uniform across a layer at a certain depth [74]. On top of that, the tilting also causes glacial flow, and ice crystals appear to align themselves along the flow direction. Since ice is a birefringent material, light from different directions will diffuse differently [75]. This effect is still being investigated.

Given the reasons listed above, an analytic function like the Pandel function are not capable of giving a faithful approximation to the actual ice scattering effect. Thus, there is an ongoing campaign to parametrize the South Pole ice and building a more accurate ice model [76][74][75]. The effective scattering and absorption coefficient (length) of ice models SPICE-MIE and AHA are plotted in Figure 3.6. Using the ice model, the distribution of the time delay of Cherenkov photons can be obtained from photon propagation simulations. A more advanced reconstruction algorithm is designed by swapping the Pandel function in Equation 3.8 to a spline table built from the simulations. This method is known as SplineMPE and will be used in the analysis in chapter 6.

3.4.4 Angular Error Estimation

Currently, the best method to search for neutrino point sources is statistical based, but the statistics of neutrinos with astrophysical origins are limited. Therefore, a per-event angular error estimation is important for the sensitivity of the point source search. In IceCube, there are two methods for estimating the statistical error of the reconstructed direction, namely, Paraboloid and Cramer-Rao.

The Paraboloid method uses the fact that most reconstructions are likelihood-based. The idea is to approximate the likelihood function near the maxima with a 2D parabola (paraboloid). When this paraboloid is projected onto the plane of zenith and azimuth, the contour should take the form of an ellipse. The uncertainty of the reconstructed direction can be estimated by finding the semi-major and semi-minor axes of the ellipse, as shown in Figure 3.7. In practice, the contour is chosen to be

$$-2\log(\mathcal{L}) = -\log(\mathcal{L}_{max}) + 1\,. \tag{3.9}$$

Since most point source analyses use an 1D Gaussian to approximate the PSF of the source,

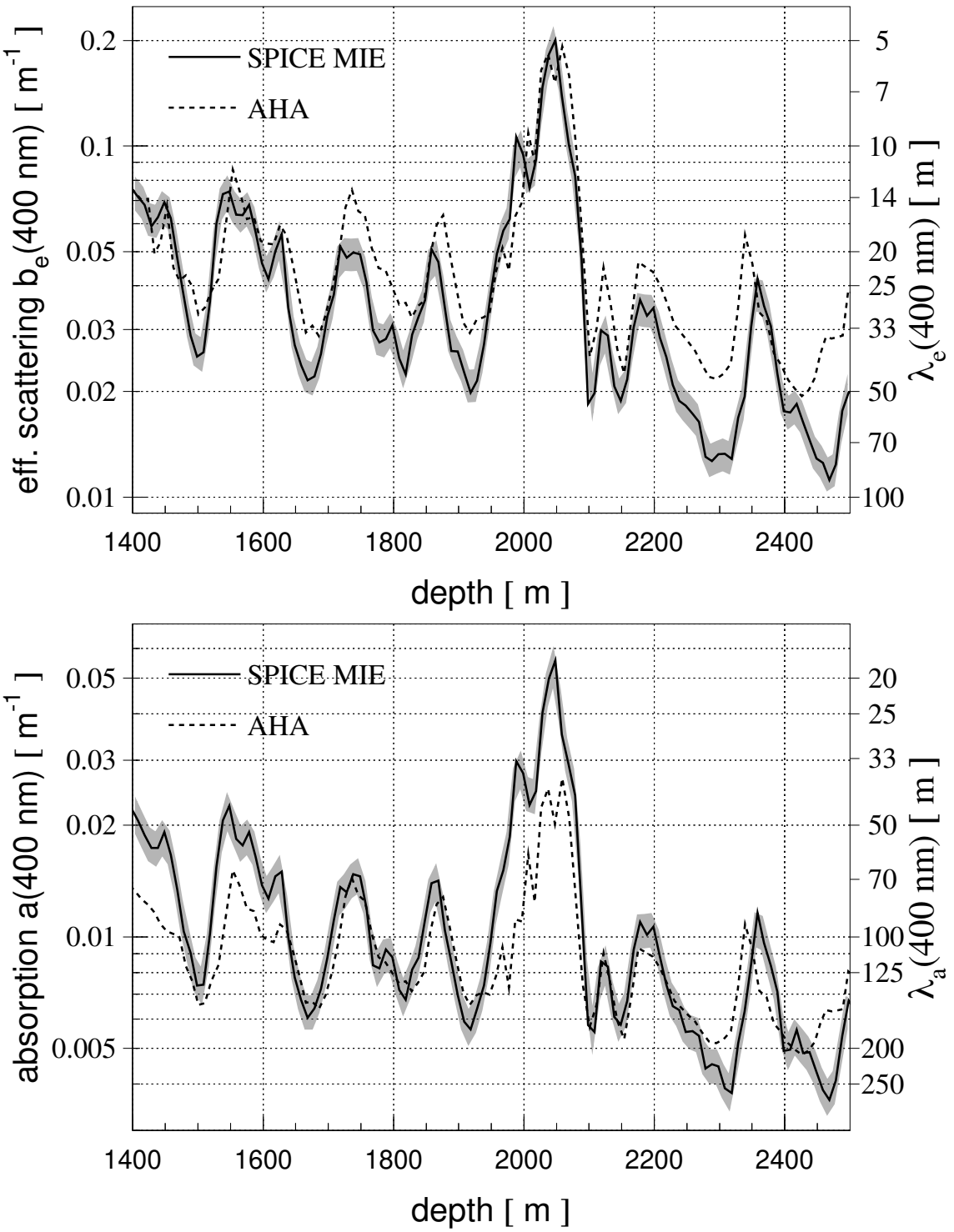

Figure 3.6: The effective scattering (top) and absorption length (bottom) as a function of depth of ice at South Pole for two different models, SPICE MIE and AHA. The y-axis on the left is the value of the coefficient, while the y-axis on the right shows the corresponding length. [76]

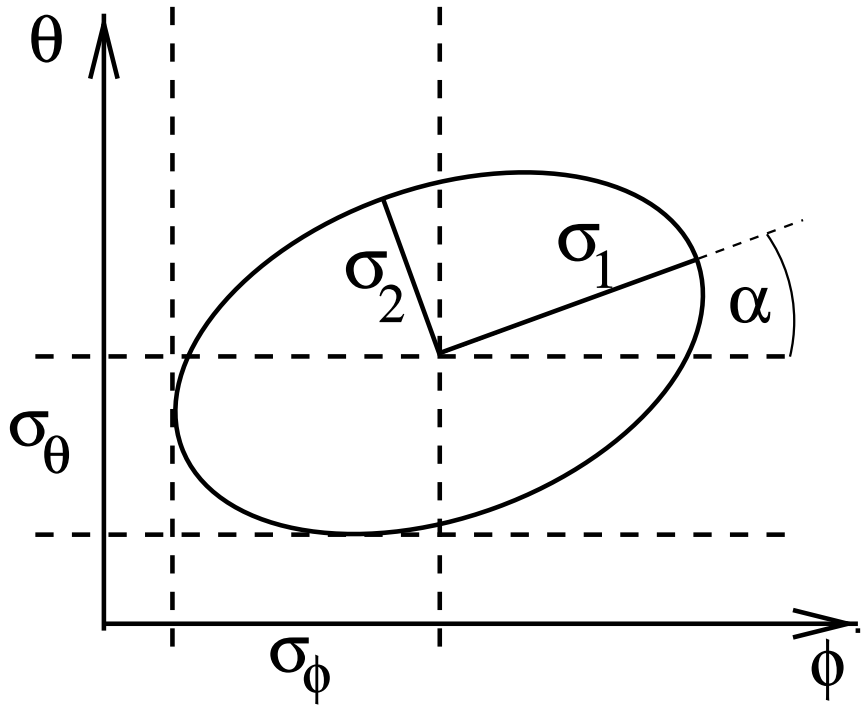

Figure 3.7: Example of a contour of the likelihood function used in reconstruction, where θ is the zenith angle and ϕ is the azimuthal angle. Figure is taken from [77]

the overall angular uncertainty is calculated as

$$\sigma = \sqrt{\frac{\sigma_1^2 + \sigma_2^2}{2}}. \tag{3.10}$$

The Cramer-Rao method, as indicated by the name, utilizes the Cramer-Rao bound. The idea is to find the lower bound of the variance of the parameter estimators by calculating the inverted Fisher information matrix, where the original matrix is defined as

$$I_{m.k}(\vec{\theta}) = -\left\langle \frac{\partial^2}{\partial\theta_m \partial\theta_k} \log \mathcal{L}(\vec{\theta}|t_{\rm res}) \right\rangle . \tag{3.11}$$

The uncertainties of zenith and azimuth are determined from the diagonal elements of the inverted Fisher matrix. Similar to Paraboloid, the overall angular uncertainty used in the analysis is calculated as

$$\sigma = \sqrt{\frac{\sigma_\theta^2 + \sigma_\phi^2 \sin^2(\theta)}{2}}. \tag{3.12}$$

For IceCube data, the Cramer-Rao method is less accurate than the Paraboloid method, it has the advantage of faster calculation (by about 200 times). Therefore, Cramer-Rao is a popular choice in many online filters.

As stated at the beginning, these methods cannot account for the effect of ice systematics, and frequently led to an underestimation of the σ at low energy and overestimation at high energy. Thus, the uncertainty σ has to be pull-corrected. This is done by first finding the median angular error between the true direction and the reconstructed direction as a function of the reconstructed energy with Monte Carlo simulations. Then, σ is scaled as a function of the reconstructed energy to give

$$1.177\sigma_{\mathrm{pull}} = \Delta\Psi\,, \tag{3.13}$$

where $\Delta\Psi$ is the median angular error, and the constant 1.177 is to ensure the resultant bivariate normal distribution with $\sigma = \sigma_{\mathrm{pull}}$ will provide a correct containment.

3.4.5 Energy Reconstruction

Before concluding this chapter, the manner in which neutrino energy is estimated should be addressed. The neutrino energy is an essential attribute for separating astrophysical neutrinos from atmospheric neutrinos, because of the predicted difference in their spectral indices. Therefore, a good energy reconstruction is essential to any analysis. Unfortunately, the accuracy of the energy reconstruction for track events is intrinsically limited, because

1. the interaction vertex is usually outside the detector, so the energy deposited in the hadronic shower cannot be measured directly;

2. the full length of the track is usually unknown, so only the energy deposited by the muon inside the detector can be measured.

Nonetheless, the muon produced by a muon neutrino interaction shares a large proportion of the energy of the neutrino. By measuring the energy deposited by the muon, one can

retain information that can be used to separate astrophysical neutrinos from atmospheric neutrinos.

One of the energy reconstruction methods used in IceCube is called millipede [78]. In this method, a given track is divided into segments, and every segment is treated as a light source. A Poisson likelihood is used to compare the number of photons k detected by the DOM, to the expected number of photons λ reaching the DOM. The photons arriving at a certain DOM are contributed by all the segments, so λ is defined as

$$\lambda = \sum_i \Lambda_i E_i + \rho, \tag{3.14}$$

where E_i is the energy deposited by the segment i, Λ_i is the light yield of that segment at a certain time bin, and ρ is the noise detected by the DOM. The log Poisson likelihood after summing over all the time bin j is

$$\sum_j \log(\mathcal{L}_j) = \sum_j k_j \log(\vec{E} \cdot \vec{\Lambda}_j + \rho_j) - \sum_j (\vec{E} \cdot \vec{\Lambda}_j + \rho_j) - \sum_j \log(k_j!)\,. \tag{3.15}$$

Please note that the energy deposition and the light yield are written in the vector form for clarity. To the first order, the condition to maximize this likelihood function can be approximated by

$$k_j = \vec{E} \cdot \vec{\Lambda}_j + \rho_j\,. \tag{3.16}$$

For a given matrix $\mathbf{\Lambda}$, which predicts the light yield at every point in the detector from every source, the equation can be written in the form

$$\vec{k} - \vec{\rho} = \mathbf{\Lambda}\vec{E}\,. \tag{3.17}$$

$\mathbf{\Lambda}$ is obtained by simulating the propagation of photons from a point source at a reference energy. The energy deposition to the DOM can be found by inverting $\mathbf{\Lambda}$ or fitting $\vec{E}$. Repeating this process for every DOM, the total energy deposited by the track can be found.

The millipede method is CPU intensive, so it is not used for high statistics data sets. For example, in the analysis discussed in chapter 6, event energies are reconstructed with a method known as MuEX [78]. The computation is reduced by using an analytical function to approximate the light yield λ. The function treats the reconstructed track as an cylindrical source in short distance and approximate the photon propagation as random walk when the receiver is farther than the propagation length. MuEX also uses a probability distribution to convolve with Equation 3.14 to account for the stochastic nature of muon energy loss.

These methods provide an estimate for the energy loss rate of the muon, i.e. dE/dx [78]. Recalling Equation 3.1, the average muon energy loss rate scales linearly with the muon energy. Thus, using the estimate of dE/dx, one can estimate the energy of the muon when it enters the detector.

CHAPTER 4

FIRESONG

4.1 Interpreting the Diffuse Neutrino Flux

No neutrino source has been discovered yet. However, this nondetection can be combined with the diffuse astrophysical neutrino flux, to derive a density limit for the underlying neutrino source population. To illustrate the idea, the derivation for the simplest case is presented here. In this scenario, the diffuse neutrino flux is supplied by a population of standard candle sources, i.e. the luminosity in the form of neutrinos is the same for every source. Furthermore, the universe is Euclidean, such that cosmological effects such as expansion are not considered. The diffuse flux is related to the per-source neutrino luminosity by

$$E_\nu^2 \frac{d\Phi_{\nu,\text{diffuse}}}{dE_\nu} = \int_0^{R_H} \rho(r) \frac{L_\nu}{4\pi r^2} r^2 dr \,, \tag{4.1}$$

where $\rho(r)$ is the number density of the source as a function of the distance, $R_H = c/H_0$ is the Hubble radius, L_ν is the neutrino luminosity. The density function can be expressed in terms of the local density and evolution function, i.e. $\rho(r) = \rho_{loc} f(r)$. Assuming the distribution of these sources exhibit no evolution, i.e., $f(r) = 1$, the above equation can be simplified to

$$E_\nu^2 \frac{d\Phi_{\nu,\text{diffuse}}}{dE_\nu} \sim \frac{\rho_{loc} L_\nu}{4\pi} R_H \,. \tag{4.2}$$

Using the diffuse flux value in Equation 1.25 and $H_0 = 70\,\mathrm{km\,s^{-1}\,Mpc^{-1}}$, the neutrino power density is approximately

$$\rho_{loc} L_\nu \sim 4.4 \times 10^{43}\,\mathrm{erg\,Mpc^{-1}\,yr^{-1}} \,. \tag{4.3}$$

Since no point source has been detected, the neutrino flux from the strongest source

can be limited by IceCube's time-integrated point source discovery potential. For a source with a hard spectrum (index = -2), the per flavor flux required for a 5σ discovery is $\sim 10^{-9}\mathrm{GeV\,cm^{-2}\,s^{-1}}$ [28]. Besides that, the strongest source is also the nearest source for standard candles. Therefore, the flux upper limit can be expressed as

$$\frac{1}{3}\frac{L_\nu}{4\pi d_c^2} \lesssim 10^{-9}\,\mathrm{GeV\,cm^{-2}\,s^{-1}}\,, \tag{4.4}$$

where d_c is the distance to the nearest source, and the factor $1/3$ is to account for the equal flavor mixing after long distance propagation. The distance to the nearest source can be approximated with the local density of the sources

$$d_c^{-1} \approx \sqrt[3]{\frac{4\pi}{3}\rho_{loc}}\,. \tag{4.5}$$

Using this expression and Equation 4.3, Equation 4.4 can be translated into an lower limit for the source local density, which is

$$\rho_{loc} \gtrsim 10^{-7}\,\mathrm{Mpc^{-3}}. \tag{4.6}$$

If more details of IceCube are included in the calculation, the derived Equation 4.4 and Equation 4.3 can form a contour on the ρ_{loc} vs. L_ν plane.

4.1.1 Constraints on Neutrino Source Candidates

The constraint on the neutrino power density and the lower limit imposed on the source density can exclude some classes of astrophysical objects as significant sources of the diffuse neutrino flux. An example from [79] is shown in Figure 4.1. In the plot, the typical luminosities of different neutrino source candidates are plotted against their local number densities. Steady objects are plotted as red dots, while transient objects are plotted as red stars. For the transient candidates, the densities correspond to the number of events per

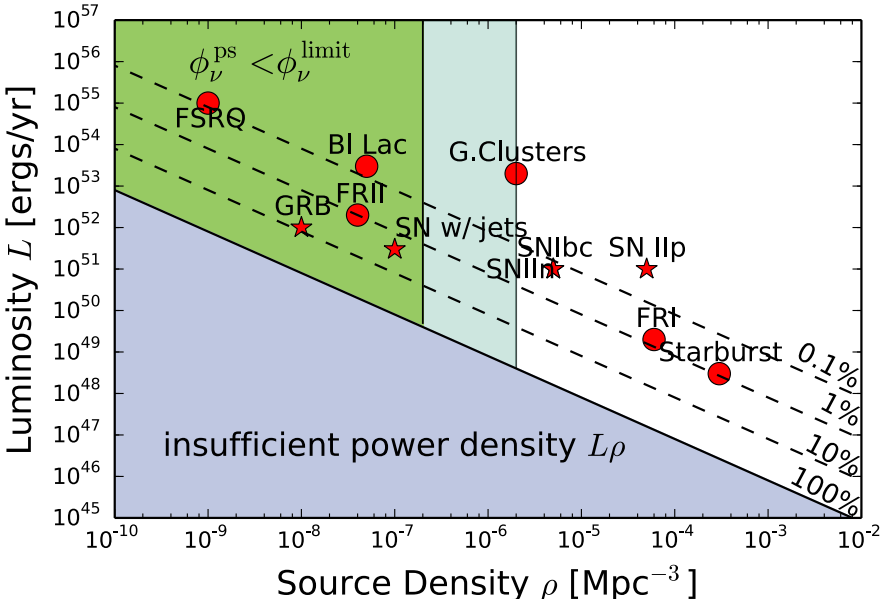

Figure 4.1: Luminosities plotted against local source densities of different neutrino source candidates. [79]

year. The solid diagonal lines represent the minimum power density required to support the diffuse neutrino flux, if the neutrino luminosity equals the typical luminosity. Astrophysical objects that lie below the line are thus excluded, unless they are in an environment very opaque to photons. If the neutrino luminosity is only a portion, e.g., 10%, 1% or 0.1%, of the typical luminosity, the line will be shifted upward, as indicated by the dashed lines. The two vertical lines indicate the density lower limits for steady emission and transient emission, which are $\sim 10^{-7}\mathrm{Mpc}^{-1}$ and $\sim 10^{-6}\mathrm{Mpc}^{-1}\,\mathrm{yr}^{-1}$ respectively. The parameter space excluded by them are shaded green and cyan. It is noteworthy that objects such as FSRQs, BL LACs and GRBs are excluded as dominant sources of the diffuse flux due to their rarity. On the other hand, different types of core-collapse supernovae, galaxy clusters, and starburst galaxies remain possible major suppliers of neutrinos observed by IceCube.

4.2 FIRESONG

The constraints derived in the previous section are under extreme simplification. In order to derive a more realistic upper limit, the effect of cosmology model, source's evolution, and luminosity function must be taken in to consideration. More sophisticated calculations have been performed by [80], [79], and [81]. Although deriving the limit is useful for theoretical interpretation, generating neutrino source distributions based on the constraints is more helpful for actual analysis. For these reasons, I worked on the development of FIRESONG[82], an open source Python package for simulating extragalactic neutrino source distributions. It has been used in numerous IceCube analyses [27][83] and other IACTs' works [84][85].

The major goal of FIRESONG is to generate a distribution of neutrino fluxes that follows a user-specified source evolution and luminosity function, while obeying the constraints on the diffuse neutrino flux and taking the cosmological effect into account. The rest of this section will be dedicated to explaining the working principle behind FIRESONG.

4.2.1 Cosmology

In FIRESONG, all cosmology related calculations are performed with the CosmoloPy[1] package under the ΛCDM model of a flat universe. The values of the cosmological parameters H_0, Ω_m, and Ω_Λ are adopted from the measurement made by Planck in 2015 [86]. The first aspect that cosmological effect has to be considered is the total number of neutrino sources in the universe. Denoting the comoving source number density at a redshift z by $\rho(z)$, the total number of sources within a certain redshift z_{max} is given by

$$N(z_{max}) = \int_0^{z_{max}} \rho(z) \frac{4\pi (c/H_0) d_L^2(z)}{(1+z)^2 \sqrt{\Omega_m (1+z)^3 + \Omega_\Lambda}} \, dz \,, \tag{4.7}$$

[1] http://roban.github.com/CosmoloPy/

where $d_L(z)$ is the luminosity distance at z. z_{max} should be large enough to cover the farthest neutrino source. A value of 10 is set as the default for FIRESONG, because it is the redshift of the farthest galaxy observed [87]. However, the star formation rate is known only up to $z \sim 4$, so the description of the source density evolution beyond relies entirely on the extrapolation.

The second aspect affected by cosmology is the neutrino flux calculation. For a source that emits M neutrinos per unit time in the comoving frame, the bolometric particle flux (unit $cm^{-2}\,s^{-1}$) is reduced by a factor of $(1+z)^{-1}$ due to cosmological time dilation,

$$\Phi(z) = \frac{M}{4\pi(1+z)d^2(z)} = (1+z)\frac{M}{4\pi d_L^2(z)}, \tag{4.8}$$

where $d(z)$ is the comoving distance at z. For a single power-law neutrino spectrum, the number of neutrinos emitted in the comoving frame can be written as

$$M = \int_{E'_{min}}^{E'_{max}} M_0 \left(\frac{E'}{E_0}\right)^{-\Gamma} dE' \,, \tag{4.9}$$

where E' denotes the neutrino energy in the comoving frame. E'_{min} and E'_{max} are the comoving frame minimum and maximum energy of the neutrinos detected in IceCube. The bolometric neutrino luminosity L_ν is therefore

$$L_\nu = \int_{E'_{min}}^{E'_{max}} E' M_0 \left(\frac{E'}{E_0}\right)^{-\Gamma} dE' \,. \tag{4.10}$$

Due to redshift, the neutrino energy in Earth's frame will be reduced by a factor of $(1+z)^{-1}$. Substituting $E = (1+z)E'$ into Equation 4.9, and then substitute it into Equation 4.8, one can obtain the expression for the differential particle flux (unit $\mathrm{GeV}^{-1}\,\mathrm{cm}^{-2}\,\mathrm{s}^{-1}$),

$$\frac{d\Phi}{dE}(z) = (1+z)^{2-\Gamma}\frac{M_0}{4\pi d_L^2(z)}\left(\frac{E}{E_0}\right)^{-\Gamma} . \tag{4.11}$$

If the differential particle flux at a certain z is found, L_ν can be found with E'_{min} and E'_{max}.

4.2.2 Source Evolution and Diffuse Flux Constraint

Most astrophysical objects' distributions evolve as the epoch of the universe. The evolution for a wide range of objects can be mimicked by the star formation rate (SFR) history [88]. In FIRESONG, the source distribution can be chosen to follow a normalized SFR evolution, and the normalization factor is determined by the source local density, which is specified by the user. The normalization factor $\mathcal{A}$ can calculated from the relation

$$\rho_{loc} V_{loc} = \mathcal{A} \int_0^{z_{loc}} P_{sfr}(z) \frac{dV_c}{dz}\, dz\,, \tag{4.12}$$

where V_{loc} is the comoving volume of the local universe up to z_{loc}, dV_c/dz is the differential comoving volume (fraction in the integral of Equation 4.9), and P_{sfr} is the SFR evolution function from [88]. The total number of sources can then be calculated by substituting $\rho(z)$ with $\mathcal{A} \times P_{sfr}(z)$ in Equation 4.7. The redshift distributions up to $z = 5$ for both SFR evolution and no evolution are plotted in Figure 4.2.

The sum of all fluxes is constrained by the diffuse neutrino flux. This condition, when combined with a specific local density, determines the luminosity of each source. In a standard candle scenario, if all sources share the same spectral index as the diffuse flux, the differential particle flux from a source at $z = 1$ is fixed as

$$\frac{d\Phi}{dE}(z=1) = 4\pi \frac{d\Phi_{diffuse}}{dE} \Big/ \mathcal{A} \int_0^{z_{max}} P_{sfr}(z) \left(\frac{1+z}{2}\right)^{2-\Gamma} \frac{d_L^2(1)}{d_L^2(z)} \frac{dV_c}{dz}\, dz\,. \tag{4.13}$$

Since the point source flux and the diffuse flux have the same spectral index, the energy term E/E_0 can be cancelled. Hence, the normalization for the point source flux can be calculated from the diffuse flux normalization. The flux distributions for three different settings are shown in Figure 4.3. As a reference, the estimated IceCube point source analysis discovery potential is also plotted in the figure. The distributions show that as the

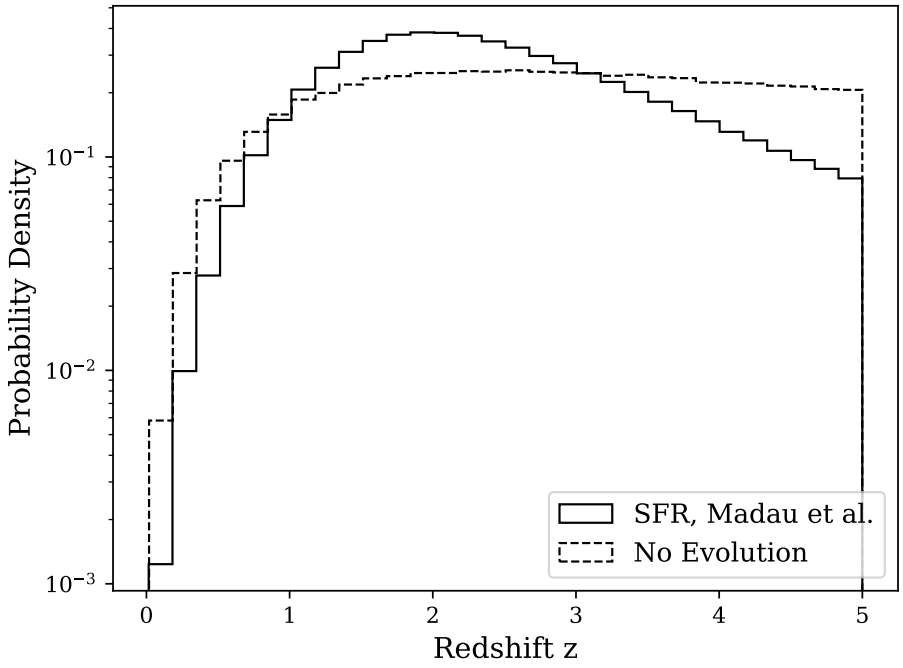

Figure 4.2: Comparing the redshift distribution of the SFR evolution from [88] to that of no evolution.

local density increases, the chance for a source to emit a neutrino flux above the discovery potential decreases.

4.2.3 Source Generation

The distribution of fluxes is obtained in the following steps. First, N_{total} sources' redshifts are generated according to the normalized SFR evolution. Then, their fluxes are calculated by scaling the reference flux from Equation 4.13 to their corresponding redshifts, i.e.

$$\frac{d\Phi}{dE}(z) = \left(\frac{1+z}{2}\right)^{2-\Gamma} \frac{d_L^2(1)}{d_L^2(z)} \frac{d\Phi}{dE}(z=1)\,. \tag{4.14}$$

Finally, the declination of the sources are generated isotropically, based on the assumption that extra-galactic sources show no preference in declination. The strongest 300 sources in a FIRESONG output is shown in Figure 4.4.

FIRESONG is also capable of generating fluxes distribution without the standard candle

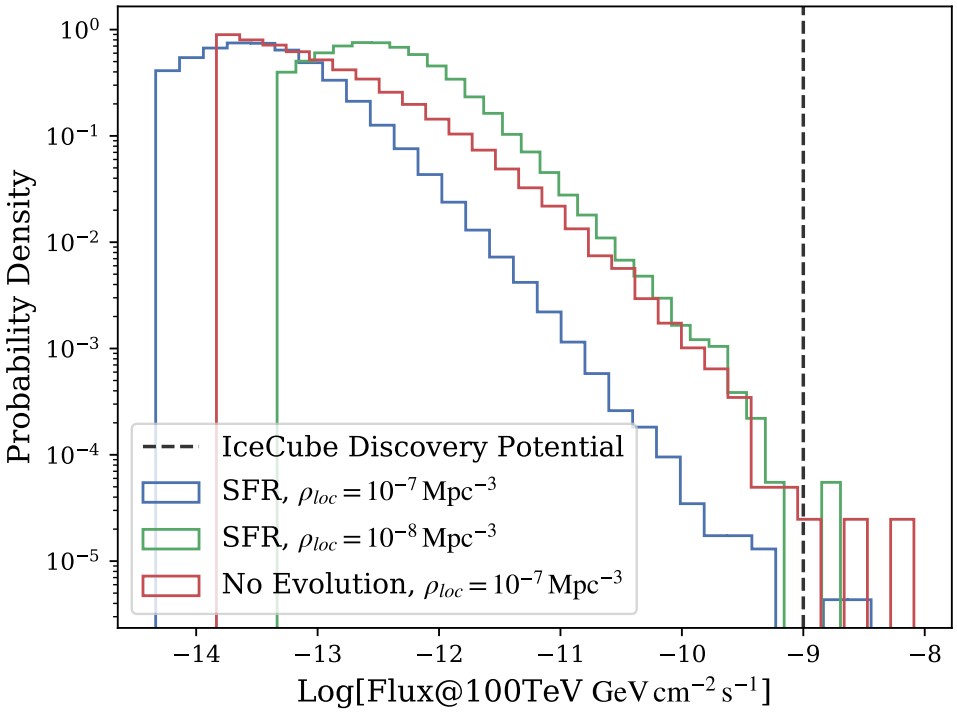

Figure 4.3: Flux distributions for three different settings. SFR evolution with $\rho_{loc} = 10^{-7}\,\mathrm{Mpc}^{-3}$ (blue) and $10^{-8}\,\mathrm{Mpc}^{-3}$ (green), and no evolution with $\rho_{loc} = 10^{-7}\,\mathrm{Mpc}^{-3}$ (red). A typical IceCube point-source analysis discovery potential in the northern hemisphere is also plotted as a black dashed line.

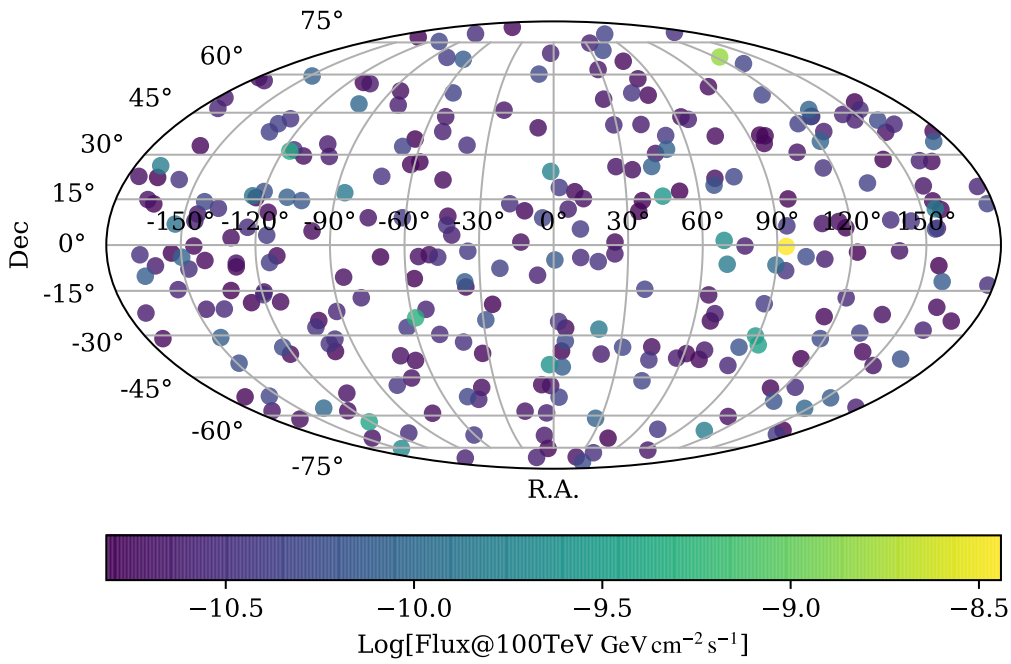

Figure 4.4: Skymap showing the 300 strongest sources generated by FIRESONG. The local density of the sources is $10^{-7}\,\mathrm{Mpc}^{-3}$ and the density evolution follow SFR from [88].

simplification. Their luminosities are allowed to follow a distribution that is redshift independent. The current implementation includes log-normal and power-law distributions. In this case, the reference flux from Equation 4.13 will be used as the mean of the distribution, and the flux at $z = 1$ will be sampled from the selected distribution.

4.2.4 Transient Sources

The discussion above applies to steady sources only. However, it is possible that the diffuse flux is contributed by numerous transient sources, e.g., GRBs or supernovae. The calculation involved in generating the transient fluxes is similar to the steady case, but with a few modification. First, consider all transient sources have the same duration ΔT in their local reference frames. For a source at z, the duration observed on Earth will be dilated to $(1 + z)\Delta T$.

If the flux is a rectangular function of time and the spectral index is time-independent, the differential particle fluence (unit $\mathrm{GeV}^{-1}\mathrm{cm}^{-2}$), i.e. differential particle flux integrated

over the time of the flare, will be given by

$$\frac{d\Psi}{dE}(z) = (1+z)^{3-\Gamma} \frac{M_0}{4\pi d_L^2(z)} \left(\frac{E}{E_0}\right)^{-\Gamma} \Delta T \,. \tag{4.15}$$

The sum of the fluences from all transient sources in a year (assuming every source flares only once) is equal to the diffuse fluence, i.e. the diffuse flux integrated over a year

$$\frac{d\Psi_{diffuse}}{dE} = \int_0^{z_{max}} \rho_t(z) \frac{d\Psi}{dE}(z) \frac{dV_c}{dz}\, dz \,, \tag{4.16}$$

where $\rho_t(z)$ is the density of the number of transient sources in a year. Hence, the normalization for the fluence can be calculated in a similar way as in the steady source case.

4.3 Application - Point Source Analysis

FIRESONG has been applied in IceCube's 8 year northern muon track analysis by René Reimann to impose limit on the source population [27]. In that work, FIRESONG was used to generate flux distributions for different ρ_{loc} and L_ν. The sources were set to follow SFR evolution [89] and their luminosities are distributed in a narrow log-normal style, which closely resembles the standard candle picture. Pseudo-experiments are produced by injecting simulated signal events based on each flux distribution into a background that consists only of atmospheric neutrinos. A point source analysis and a population analysis (see chapter 6 for details on these analyses) were then performed on each pseudo-experiment.

A 90% C.L. upper limit in the $\rho_{loc} - L_\nu$ plane was calculated for each analysis. In the point source analysis, the upper limit was found by requiring the strongest source in the pseudo experiment to have a significance below the significance found in the actual experiment. This limit is shown as the dashed line in Figure 4.5. In the population analysis, the upper limit was found by requiring the most significant group of sources to show a significance below that of the actual experiment. This limit is shown as the solid line in the figure. For comparison, the upper limit derived using the diffuse flux by [80] is shown as

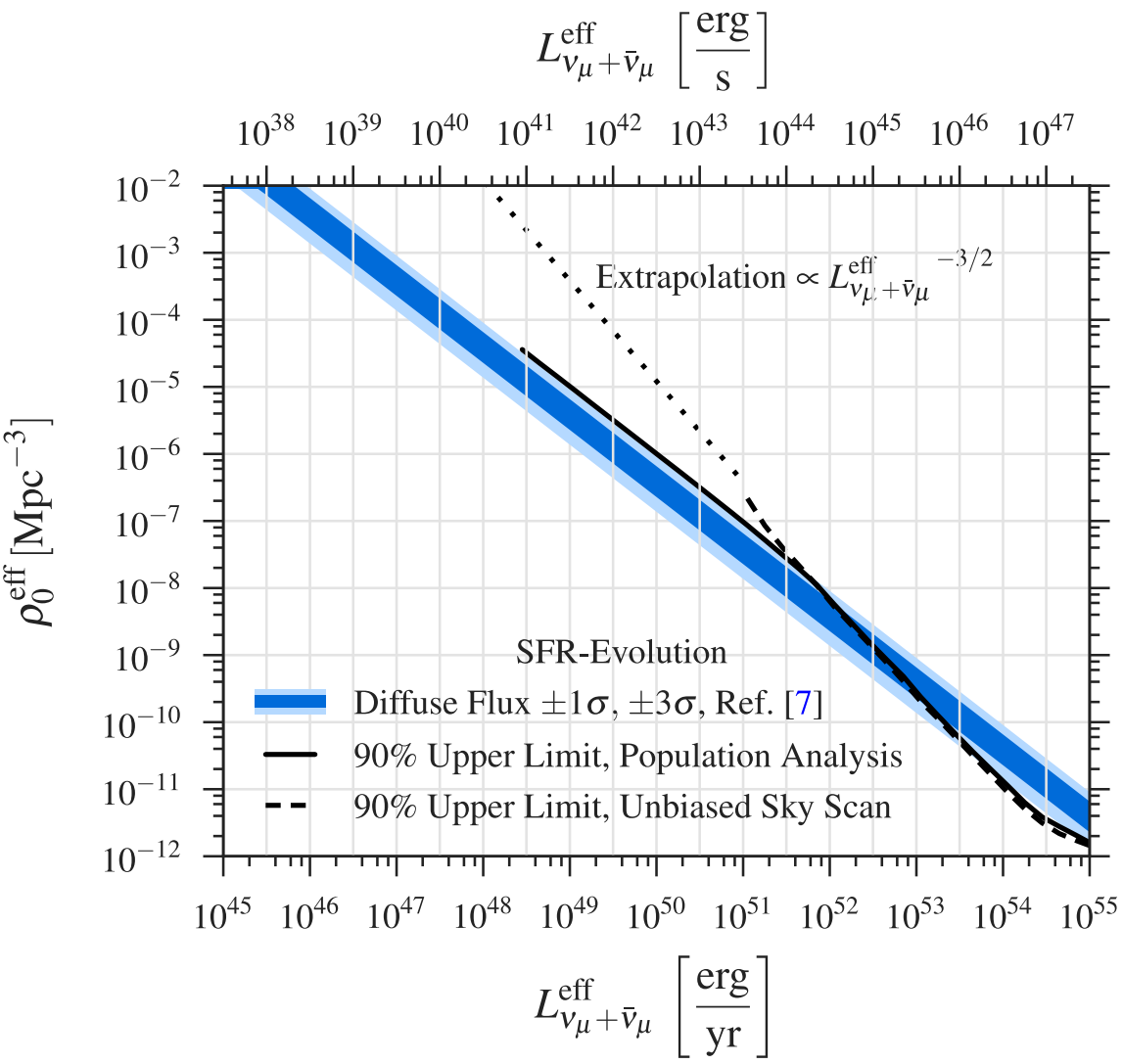

Figure 4.5: 90% C.L. on the neutrino luminosity. L_ν is denoted as $L^{\rm eff}_{\nu_\mu+\bar{\nu}_\mu}$ and ρ_{loc} is denoted as $\rho_0^{\rm eff}$ in the figure. Figure is reproduced from [27].

the blue line in the figure. FIRESONG provided a stronger limit in the low density region.

4.4 Application - Multimessenger Astronomy

Since gamma rays are part of the products of hadronic processes that produce high energy neutrinos, neutrino sources are very likely to also emit gamma rays. Using the production mechanism outlined in chapter 1, the neutrino flux can be related to the gamma-ray flux by

$$\frac{1}{3}\sum_{\alpha}^{3} E_{\nu}^{2}\frac{dN_{\nu}}{dE_{\nu}} = \frac{K_{\pi}}{4}E_{\gamma}^{2}\frac{dN_{\gamma}}{dE_{\gamma}} \tag{4.17}$$

for $E_{\gamma} = 2E_{\nu}$. In the equation, α is the flavor of the neutrino, and K_{π} is the charged-to-neutral pion ratio, which depends on the production process. For a $p\gamma$ interaction, $K_{\pi} = 1$, while a pp interaction will result in a $K_{\pi} = 2$. If the neutrino sources are assumed to be optically thin outside the production site, the neutrino flux distribution can be converted into a gamma-ray flux distribution which is limited by the diffuse neutrino flux.

The gamma-ray flux distribution can be used to estimate the chance for detecting gamma rays emitted by a neutrino source in coincidence with a neutrino event. Adopting this idea for the proposed Cherenkov Telescope Array's (CTA) Neutrino-Target-of-Opportunity (NToO) program, an estimation was performed by Konstancja Satalecka, Anthony Brown, Alberto Rosales-de-leon, Olga Sergijenko, Rene Reimann, Theo Glauch, Ignacio Taboada and I [85][90]. The goal of the study was to estimate the probability for CTA to detect a source in a follow-up observation triggered by a neutrino flare similar to the one exhibited by TXS 0506+056 between 2014 and 2015 [30]. In the calculation, the model of the neutrino sources was adopted from [91], in which the sources belonged to a subclass of BL-Lac objects characterised by TXS. As a remark, a similar work is being studied for MAGIC [92].

The source distribution was generated under a few assumptions. First, the local rate density of the flares from the sources in a year was a fraction of the density of the entire BL-Lac population, i.e.

$$\rho_{loc} = \mathcal{F}\rho_{BL}\,, \tag{4.18}$$

where $\rho_{BL} = 1.5 \times 10^{-8}\,\mathrm{Mpc}^{-3}$. Second, the sources were assumed to be standard candles that show no evolution over redshift. Third, these sources are assumed to have the same flare duration in the corresponding comoving frame. The duration can be calculated from the flare data of TXS in 2014-2015, which was observed to be 110 days on Earth [30],

and was found to be 82 days in the comoving frame after correcting for TXS's redshift $z = 0.335$. Lastly, the neutrinos emitted in these flares were assumed to saturate the diffuse neutrino flux.

Suppose a neutrino alert event is produced from this source distribution, the probability for this event to be emitted at z is proportional to $\rho(z)(dN/dE)$. Hence, the distribution of redshifts from where the alerts were coming could be found. Figure 4.6a shows the redshift distribution for the neutrino alerts produced by a group of TXS-like sources with $\mathcal{F} = 1\%$. From there, a list of sources that produced neutrino alerts was generated.

The neutrino fluxes responsible for the alerts were converted to gamma-ray fluxes using a model spectrum from [91], which was given by

$$\frac{dN_\gamma}{dE} = A_\nu E^{-2} e^{(-E_L/E - E/E_H)}\,, \tag{4.19}$$

where A_ν was the neutrino flux normalization, E_L and E_H were the low and high energy cutoffs and had values of 0.1 TeV and 20 TeV respectively. The probabilities of detecting these alerts with CTA were calculated by passing the EBL attenuated gamma-ray fluxes to CTA's instrument response functions (IRF), which took care of the zenith and azimuth dependencies. The zenith-averaged detection probabilities at each CTA site as functions of the flaring fraction $\mathcal{F}$ were shown in Figure 4.6b. The bands represented the systematic uncertainties due to magnetic field configuration. It showed that in the most optimistic scenario, about 1/3 of the neutrino alerts that were generated by TXS-like flares could result in a gamma-ray detection by CTA.

IceCube's realtime alert system issues about 10 Gold alerts per year (see chapter 5 for details). On average, 50% of these alerts are originated from astrophysical sources. If all astrophysical alerts are produced by the TXS-like sources, CTA is expected to detect about one to two of these sources in gamma rays per year. It should be noted that the TXS-like sources are predicted to be dim in above-GeV gamma rays. Since the majority of the

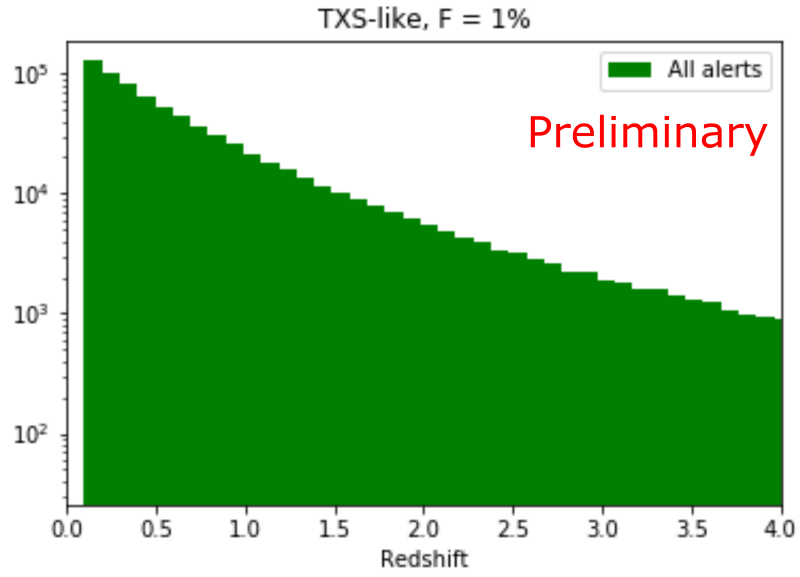

(a)

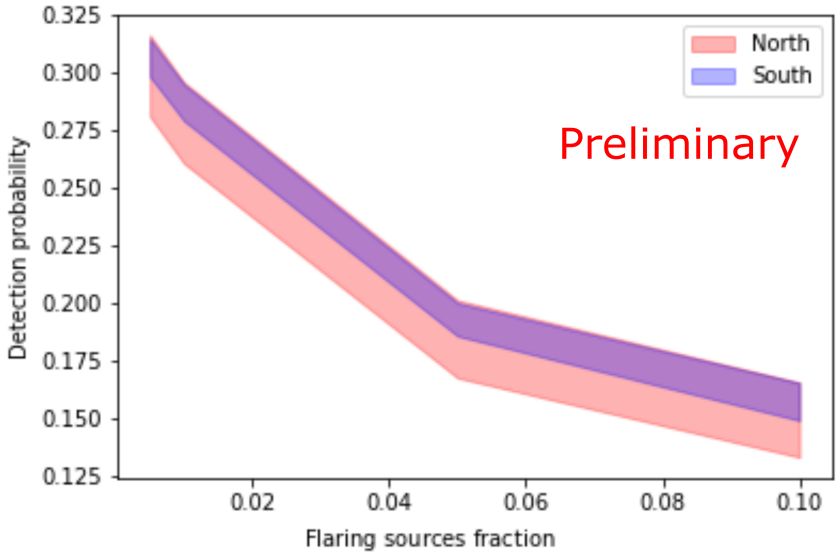

(b)

Figure 4.6: (a) Redshift distribution of neutrino alerts' origin if all of them are produced by TXS-like sources, and each source produce a neutrino alert event. (b) CTA's detection probability of neutrino alerts. North is the detection probability for the Northern Hemisphere Array in La Palmer. South is the detection probability for the Southern Hemisphere Array in Chile.

neutrino source models predict the sources to be gamma-ray bright, the chance for CTA to detect them will be even higher.

4.5 Discussion

Besides the two applications mentioned in the previous sections, FIRESONG has also been used in several published studies, such as [84] and [83], and several works in progress within IceCube, such as point-source analyses on GRBs and neutrino alerts. In these applications, FIRESONG provides a way to impose limits on the luminosity and density of the source population without the need to modify the analyses that are designed for studying point sources individually. This is achieved by using general yet robust assumptions on the distribution of the sources. Nevertheless, it is a powerful tool to extend the scope of the science of many neutrino analyses.

CHAPTER 5

ICECUBE REALTIME ALERT SYSTEM

5.1 Multimessenger Astronomy

The discovery of an astrophysical neutrino flux [21] and gravitational waves [93] signaled the beginning of the era of multimessenger astronomy. This emerging field allows one to study objects that were difficult or even impossible to observe with EM waves alone. These include the extra-galactic sources attenuated by EBL as discussed in chapter 1, and events that do not emit photons, such as black hole mergers. For the origin of cosmic rays problem, the multimessenger approach is the most promising solution right now. Currently, neutrino astronomy is still hindered by small statistics, which is more detrimental to transient events, as the statistics cannot be increased by lengthening the exposure. Therefore, these events are not likely to be resolved with statistical significance by IceCube, the leader in the current generation of neutrino telescopes.

However, neutrino telescopes also have advantages over conventional telescopes. First, they have a large field of view (FOV) which usually covers more than half of the sky. For example, IceCube is the most sensitive for declinations between -5 deg and 90 deg, but it has sensitivity over the entire sky. As a comparison, most of the wide-field telescopes have FOV much smaller than 10 square degrees. The second advantage of neutrino telescopes is the long uptime. Since the detection of high energy neutrinos is not affected by day-night cycle, neutrino telescopes can collect data almost in a continuous fashion, interrupted only by operation necessities. In the recent years, IceCube has achieved over 99% duty factor. These strengths allow IceCube to take on the role as an all-time, all-sky high energy event monitor. When IceCube detects an event with a high probability of being astrophysical neutrino, it will send out a machine-readable message to the astronomy community to

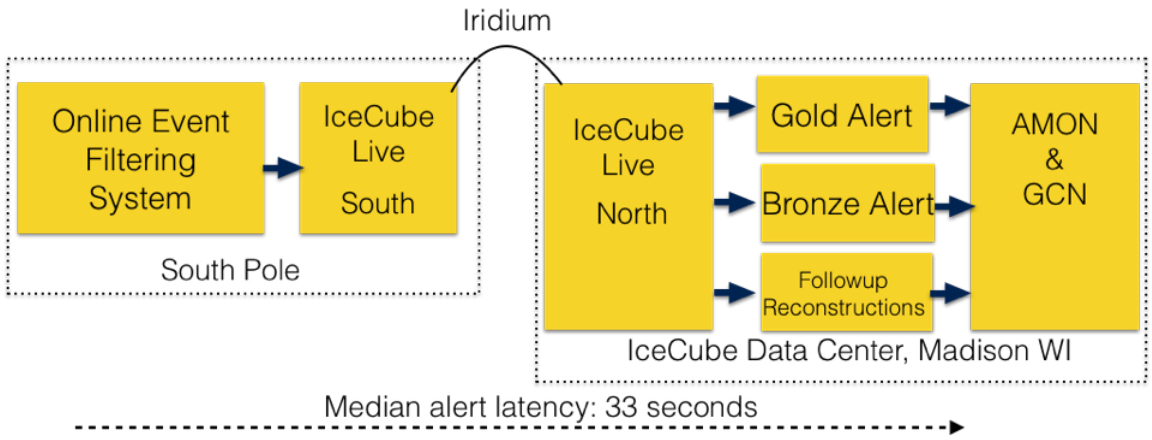

Figure 5.1: Schematic overview of the data flow of the current IceCube Realtime Alert System. Please note that only track alerts are included in this figure.

trigger follow-up observations of the incoming direction of the event. The source of the neutrino can then be resolved if there are spatial and temporal coincident detection made by other detectors.

In order to facilitate the follow-up observations, IceCube established a realtime alert system to provide the information of highly astrophysical neutrino-like events upon detection to the public [94]. The system was first implemented in 2016 and received an update in 2019, which I participated in. The details of the updated system and comparison with the first generation will be given in the following sections.

5.2 Overview

An overview of the IceCube Realtime Alert System is shown in Figure 5.1. The data flow begins at the Processing and Filtering (PnF) step at South Pole (see chapter 3). When an event passes one of the few related filters, the essential information for follow-up (time, some reconstructed quantities including direction and energy, and detector information) will be collected in a JSON-formatted[1] message, and sent to the data center in the north via the Iridium RUDICS system[2]. The remaining information of the event, such as the detected

[1] https://www.json.org
[2] https://www.iridium.com

pulses in each DOM, will be sent in a second message that will arrive at the north at a later time. The practice is put in place due to the bandwidth restriction of the satellite, which is similar to that of a dial-up connection. The small size of the initial message allows it to reach the north with a minimal time delay. The median of the total time delay, which is the time elapsed from the event detection until the message arrival at the data center, is 33 seconds [94].

After the initial message reaches the north, sets of selection criteria will determine if the event qualifies for an alert, based on the event's information included in the message. If the event passes the selection, an alert will be published via the Gamma-ray Coordinates Network[3] (GCN) under the Astrophysical Multimessenger Observatory Network[4] (AMON) system. All alerts are generated in a fixed format to promote machine readability, so receivers can perform follow-up observations automatically. In the first version of realtime alert system, there were two types of alert, namely EHE and HESE, which were differentiated by the event's hit pattern. However, this classification has been replaced since June 2019. In the current version, there are 3 types of alerts that are triggered solely by IceCube events, in which two of them are designed for track events and the remaining one is designed for cascade events. The two track-type alerts are called Bronze and Gold, differentiated by the signal probability of the events.

Once the second message from south pole arrives at the data center, a more sophisticated reconstruction, known as millipede (see subsection 3.4.5), will be performed on the events with issued alerts. This process is very computational demanding, and usually takes $\mathcal{O}(10^3)$ CPU hours for the entire process. With the help of large-scale distributive computing dedicated to the alert system, the reconstruction can be completed about 2 to 3 hours after the alert. Meanwhile, the event will be checked by IceCube members to make sure the detector and the event selection are working as intended. If there is abnormality in the data, a retraction will be submitted to GCN Circulars. If no error is found, once the re-

[3]https://gcn.gsfc.nasa.gov/

[4]https://gcn.gsfc.nasa.gov/amon.html

construction is complete, the new information, which include the direction and uncertainty estimation, will be issued as a revision to the alert. A message that contains the updated information with a descriptive summary will also be submitted to the GCN Circulars.

5.3 IC170922A and TXS 0506+056

5.3.1 Detection

IceCube detected an EHE event on September 22, 2017 at 20:53:30 Coordinated Universal Time[5]. This event had 5785 photoelectrons and the reconstructed declination was +5.75 degree (J2000 epoch), which passed the alert requirement with a signalness of 57% (see definition of signalness in section 5.4). The initial alert for this event, IceCube-170922A, was published 43 seconds after the detection. The millipede reconstruction refined the incoming direction to right ascension = $77.43^{+0.95}_{-0.65}$ degrees and declination = $5.72^{+0.50}_{-0.30}$ degrees (J2000), where the superscript and subscript indicated the 90% containment region. The energy deposited by the muon was estimated to be $23.7 \pm 2.8\,\mathrm{TeV}$, from which the most probable neutrino energy was estimated to be $290\,\mathrm{TeV}$ [29]. Immediately after the detection, it was noticed that the blazar TXS 0506+056 was located 0.1 degrees away from the reconstructed direction.

The alert received massive attention from the astronomy community. Fermi LAT Collaboration reported that TXS 0506+056 was in a flaring state since April 2017, and detected a 0.1-300 GeV gamma-ray flux ~ 6 times stronger than quiescent state during the time of the IceCube event [95]. This observation was confirmed by AGILE's detection of $>$0.1 GeV gamma-ray flux [96]. Several ground-based Imaging Atmospheric Cherenkov Telescopes (IACTs) also performed follow-up observation on the neutrino alert. H.E.S.S. and VERITAS reported no gamma-ray sources detected in the location of the IceCube alert [97][98], but MAGIC reported a detection of VHE gamma-ray source with a 6.2σ significance in a follow-up observation performed six days after the alert [99]. The observations

[5] https://gcn.gsfc.nasa.gov/notices_amon/50579430_130033.amon

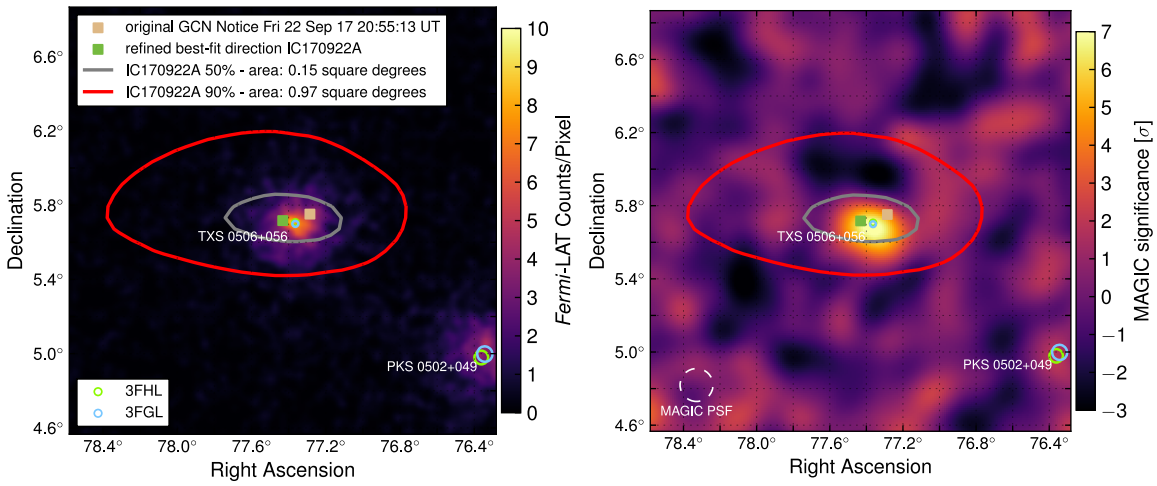

(a) (b)

Figure 5.2: Gamma-ray observation by (a) Fermi-LAT and (b) MAGIC. For both figures, the position of TXS 0506+056 reported in 3FGL and 3FHL are shown as cyan and green circles, respectively. The initial reconstruction direction of IC170922A is indicated by the gold square. The refined direction is indicated by the green square. The 50% and 90% containment contours of the refined IC170922A direction are shown as gray and red respectively.

by Fermi LAT and MAGIC are shown in Figure 5.2. Observation for >1 TeV gamma rays was performed by HAWC, but no source was detected.

Besides gamma rays, observations were performed at other wavelengths, which include radio, optical, and X-ray. For the details of those observations, readers should refer to [29]. IceCube also searched for an abundance of neutrino events in the archival data, and found a flare of neutrino events between 2014 and 2015 [30]. However, no significant event was detected in 2017 before or after IC170922A.

5.3.2 Chance Coincidence Probability

The significance of the coincident between IC170922A and the detection of gamma rays was calculated using a maximum likelihood method [29]. The likelihood function was defined as

$$\mathcal{L}(n_s) = n_s S + (1 - n_s) B \,, \tag{5.1}$$

where S and B were the probability density functions (PDFs) for signal and background, respectively. n_S was the number of signal events, and can be either 0 or 1, given that only one neutrino event was detected in coincidence with a gamma-ray flaring. The signal probability density was given by

$$S(\vec{x}, t) = \sum_s \frac{1}{2\pi\sigma^2} \exp\left(\frac{-(\vec{x_s} - \vec{x})^2}{2\sigma^2}\right) w_s(t) w_{acc}(\theta_s)\,, \tag{5.2}$$

where $\vec{x}$, t, and σ were the reconstructed direction, time and direction uncertainty of the event, $\vec{x_s}$ was the direction of the s-th source, and the sum was iterated for 2257 extra-galactic sources from the Fermi 3FGL catalog [100]. w_{acc} was the zenith-dependent acceptance function of IceCube, and θ_s was the zenith angle of the source. $w_s(t)$ was the weight for the temporal coincident between the IceCube event and gamma-ray emission from source s, and its definition was based on the model of neutrino emission.

The background PDF was given by

$$B(\vec{x}) = \frac{\mathcal{P}_{Bg}(\theta)}{2\pi}\,, \tag{5.3}$$

where $\mathcal{P}_{Bg}$ was the zenith distribution PDF of the alert events. The test statistics was found by comparing the likelihood of the signal hypothesis with that of the background hypothesis, i.e.

$$TS = 2\log\frac{\mathcal{L}(n_s = 1)}{\mathcal{L}(n_s = 0)} = 2\log\frac{S}{B}\,. \tag{5.4}$$

The background TS distribution was obtained from randomly drawn simulated alert events, which included atmospheric muon neutrinos, atmospheric muons, and astrophysical muon neutrinos. The significance of IC170922A was calculated by comparing its TS with the background TS distribution.

Three different models of temporal correlation between neutrino and gamma rays were tested, and the significance was calculated in each case. In the first one, the neutrino flux

was directly proportional to the gamma-ray energy flux between 0.1 to 100 GeV. $w_s(t)$ was defined as

$$w_s(t) = \int_{0.1\,\mathrm{GeV}}^{100\,\mathrm{GeV}} E_\gamma \frac{d\phi_\gamma}{dE_\gamma} dE_\gamma \,, \tag{5.5}$$

where ϕ_gamma was the photon flux constructed from Fermi-LAT measurement with a 28-day wide binning. In the second case, the neutrino flux was proportional to the brightening of the gamma-ray flux, i.e.

$$w_s(t) = \phi_\gamma(t) / \langle \phi_\gamma \rangle \,, \tag{5.6}$$

where $\langle \phi_\gamma \rangle$ was the time-averaged photon flux. In the last case, motivated by the detection by MAGIC, the neutrino flux was proportional to the gamma-ray energy flux in the VHE regime (>100 GeV). The lightcurves used in this model were extrapolated from the 0.1-100 GeV Fermi-LAT lightcurves to 1 TeV. The significance of the three models were shown in Table 5.1.

Table 5.1: Significance of IC170922A under three different models of neutrino-gamma ray correlation.

Model	Significance (Post-trial)
Gamma-ray energy flux	4.1 σ (3.0 σ)
Gamma-ray brightening	4.1 σ (3.0 σ)
VHE gamma-ray energy flux	3.9 σ (2.8 σ)

The look-elsewhere effect was corrected for the post-trial significance p_{global}, which was obtained by correcting the pre-trial significance p_{local} as

$$p_{global} = 1 - (1 - p_{local})^N \,, \tag{5.7}$$

where N is the number of trials. In this analysis [29], the number of trials was the number of alert events, which included IC170922A, the 9 alerts issued before IC170922A, and 41 events that qualified as alerts but were detected before the realtime system was established. Since not all 51 events were subjected to the same treatment as IC170922A before the analysis, I reconstructed these events with the millipede method, and to check if any Fermi-LAT

sources from 3FGL[100], 3FHL[101], or 2FAV[102], were within the 90% contour. Four events with poor angular resolution ($> 5^o$) were ignored, because the spatial correlation would not be significant. One event was found to be in spatial coincidence with the 3FGL source 3FGL J1040.4+0615. However, the source was about 3 orders of magnitude dimmer than TXS 0506+056. Moreover, when the neutrino arrived, the source was about a factor of 2 dimmer than its brightest period. Therefore, this event was not considered as a coincident detection with gamma rays.

5.4 Realtime System Update

The detection of IC170922A and its follow-up campaign revealed that there was a large interest for IceCube's realtime alert. While the alert rate of the first generation system was ~ 8 per year, several partner observatories, including Fermi LAT and VERITAS, expressed interest in a higher rate stream. Thus, the alert selection scheme was updated with a few goals in mind: 1. provide more alerts without a sacrifice of signal purity; 2. improve the angular resolution to provide more accurate direction for follow-up observation and to reduce alert retractions ; 3. more user-friendly alert classification.

To increase the rate of alert, the pool of alert candidates was expanded. The pool was formed by events that passed the designated filters at the PnF level. In the old version, only the EHE filter and HESE filter were considered. The EHE filter was designed to select high energy through-going track events by requiring a minimum number of photoelectron detection. The HESE filter was designed to select high energy starting events, the detail of the filter is discussed in the next section. In the updated version, the GFU filter was added on top of the original two. It was designed to select high-quality through-going track events similar to those used in IceCube's point-source analysis. The filter featured boosted decision trees (BDTs) that were trained to pick out through-going track events caused by astrophysical muon neutrinos.

Each filter came with a set of criteria that a filtered event must satisfy to qualify as an

alert. In general, the criteria had two missions. The first was to ensure the events were well reconstructed with a good angular resolution. The second was to ensure the signal purity. In the scope of the realtime system, signal was defined as track events caused by astrophysical muon neutrinos, while background was defined as any other events. A "signalness" parameter was introduced to provide a quick measure of the signal probability of an alert. This parameter was a function of the energy proxy E and reconstructed declination $delta$ of the alert, and was defined as

$$\text{Signalness}(E,\delta) = \frac{N_{signal}(E,\delta)}{N_{signal}(E,\delta) + N_{background}(E,\delta)}\,, \tag{5.8}$$

where N_{signal} and $N_{background}$ are the number of signal alert events and background alert events at the declination δ with energy above E, respectively.

In the old version, alerts were classified by the filter they passed, i.e., EHE and HESE. However, it was realized that such a naming method was obscure to the public. Therefore, the alerts were classified by their signalness in the updated version. Bronze alerts were issued for events with a signalness between 30% and 50%, and Gold alerts are issued for events with a signalness above 50%.

5.5 Realtime HESE

I designed a new set of HESE event alert criteria for the realtime alert system update. The new criteria were designed to improve on two aspects of the original implementation of HESE alerts. The first aspect was the signal ratio of the data sample, because the original alert cut was optimized for a signalness of 25%, which could not satisfy the updated requirement (30% and 50%). The second aspect was the angular resolution. As observed during the first two years of running, there were occasions that the online reconstructed direction was more than 30 degrees away from the direction obtained by the millipede reconstruction. Although these mis-reconstructed alerts were usually retracted, they would

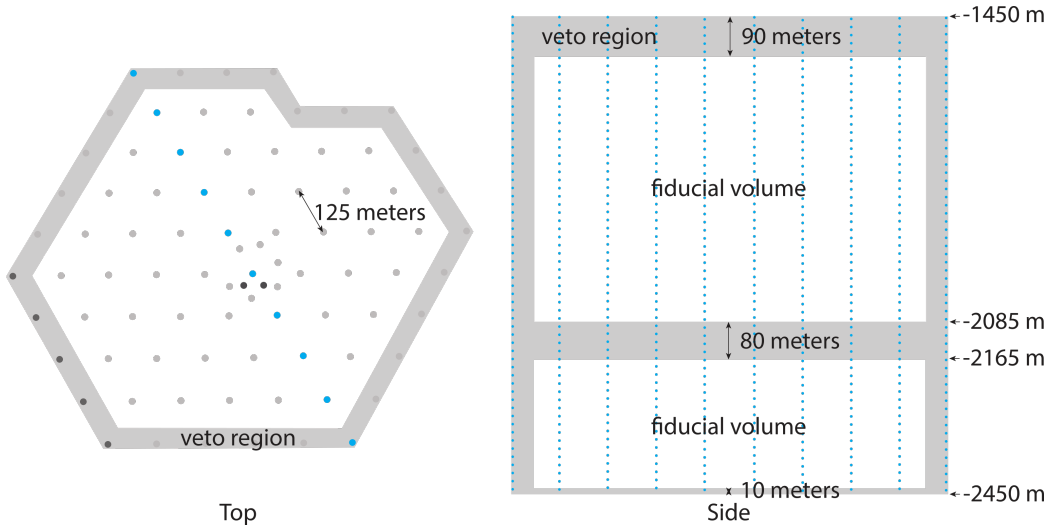

Figure 5.3: Top view and bottom view of the detector. The veto region is shaded in gray.

cause confusion and could lead to fruitless follow-up observations and waste of resources. In the three years runtime of the first generation realtime system, a total of four realtime HESE alerts (out of 17) were retracted.

The first step of the HESE alert is the HESE filter[21]. This filter uses the outermost strings, the top 90 and bottom 10 meters of the detector, and the dust layer, as veto regions. The remaining part of the detector is treated as the fiducial volume. The veto region and fiducial volume are shown in Figure 5.3. The filter requires no more than 3 of the first 250 HLC photoelectrons (PE) to be detected in the veto region. Since muon events are likely to emit light in the veto region as they enter the detector, they are more prone to getting filtered. On the contrary, neutrinos do not emit light, so an event produced by a neutrino interacting in the fiducial region will not be filtered by the veto technique. The filter also requires a minimum of 6000 PE deposited in the detector, to further increase the chance of muon depositing PE in the veto region. The resultant HESE sample consists mainly of neutrinos events with interaction vertices located inside the detector.

The HESE sample contains both track-like events and cascade events. The track-like events, which are called starting tracks in this case, can be produced only by CC interactions of muon and tau neutrinos. All the other interactions produce cascade events. Since cascade

Table 5.2: Breakdown of number of event per year. Number of track-like events are listed in the parenthesis for astrophysical ν_μ and ν_τ.

	Astrophysical ν (Track)	Atmospheric ν
ν_μ	2.09 (1.66)	3.41
ν_τ	3.63 (0.28)	0
ν_e	5.97	0.42

events have a median angular error of $\sim 15^o$, which is larger than many telescopes' FoV, they are not considered for the Gold and Bronze alerts. The expected numbers of HESE events per year can be calculated using computer simulation with the diffuse flux measurement in [103] and the atmospheric neutrino model by [104], based on the assumption of 1:1:1 flavor mixing. A breakdown of the number is shown in Table 5.2. Besides neutrino events, due to the stochastic nature of muon energy loss, some atmospheric muons are able to sneak pass the veto. Unfortunately, the simulation for this type of event is extremely difficult, so the expected number of event needs to be calculated in a data-driven approach. According to [103], there are ~ 4 atmospheric muon events per year, estimated using a muon-tagging technique outlined in [76]. It can be seen that signal (astrophysical tracks) events contribute ~ 2 events per year, which amounts to a small fraction of the sample.

5.5.1 Alert Criteria

Due to the limited computing resources at South Pole, the alert criteria were designed around the parameters provided by existing online reconstructions. Simple reconstructions based on track hypothesis and cascade hypothesis are performed on each HESE event during the PnF stage. The track reconstructions use the SPE and SplineMPE methods which are discussed in chapter 3. The cascade reconstruction uses the SPE likelihood function (Equation 3.6) to fit the interaction vertex position and time, but not the energy or direction of the neutrino.

The updated criteria which I designed for HESE alerts are:

1. $L_{dir} \geq 200\,\mathrm{m}$;

2. $\log(\mathcal{L}_{\text{track}}) - \log(\mathcal{L}_{\text{cascade}}) \geq 0$;

3. $Q \geq Q_i(\theta_z), \quad i \in \{\text{Gold, Bronze}\}$.

Table 5.3: Minimum charge thresholds for gold and bronze alerts at different cosine zenith bins.

$\cos(\theta_z)$	Q_{Gold}	Q_{Bronze}
[-1; -0.75]	6000	6000
[-0.75; -0.5]	6000	6000
[-0.5; -0.25]	8500	6000
[-0.25; 0]	22000	7000
[0; 0.25]	23000	7500
[0.25; 0.5]	11500	9500
[0.5; 0.75]	8500	6000
[0.75; 1]	7500	6500

L_{dir} is the reconstructed track length estimated with direct hits, i.e. DOM hits that experienced minimal scattering by ice. In this work, a direct hit is defined as a hit with residual time t_{res} between -15 ns and +25 ns, where t_{res} is calculated using the reconstructed track parameters. The distance between the earliest and the last direct hit projected on the track is used as the measurement of the direct track length.

Starting tracks and cascades show vehemently different distribution of the reconstructed track length. The distributions are shown in Figure 5.4a. It can be seen that most of the cascades have a reconstructed track length below 200 m, which is correlated to the radius of the cascade. For starting tracks, more events have a track length above 200 m, but the peak still persist below the threshold. This peak is populated by mis-reconstructed events, as shown in Figure 5.4b, in which the reconstructed track parameters do not coincide with the actual muon track, so the track lengths are estimated with the cascade part of the signal. Therefore, this requirement also cuts out the mis-reconstructed events and improve the angular resolution of the alerts.

$\log(\mathcal{L}_{\text{track}})$ and $\log(\mathcal{L}_{\text{cascade}})$ are the maximized log-likelihoods from SPE track and cascade reconstructions, respectively. The likelihood is larger when the hits are better described by the hypothesis. The difference between the two log-likelihoods (equivalently the

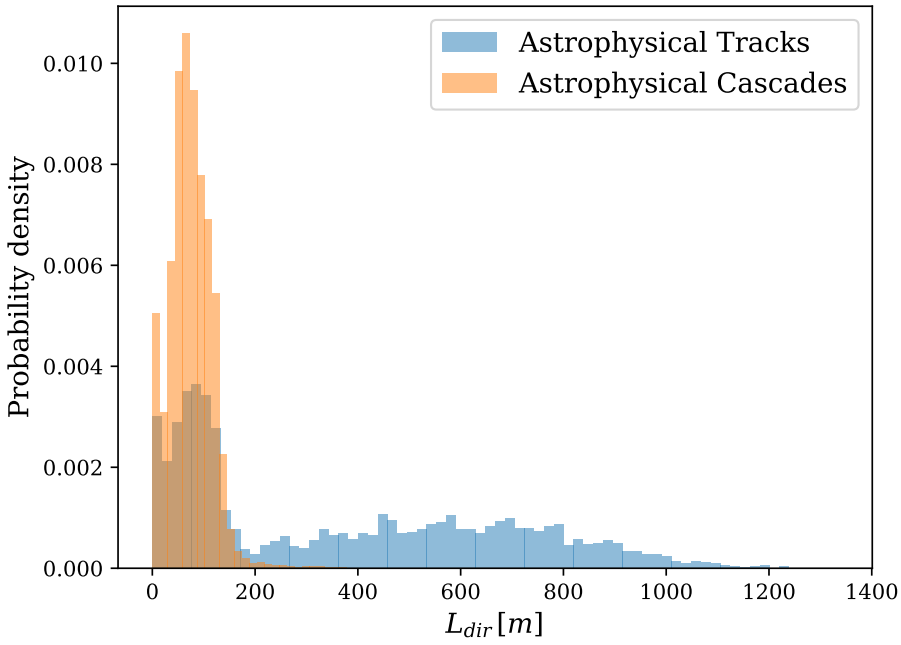

(a)

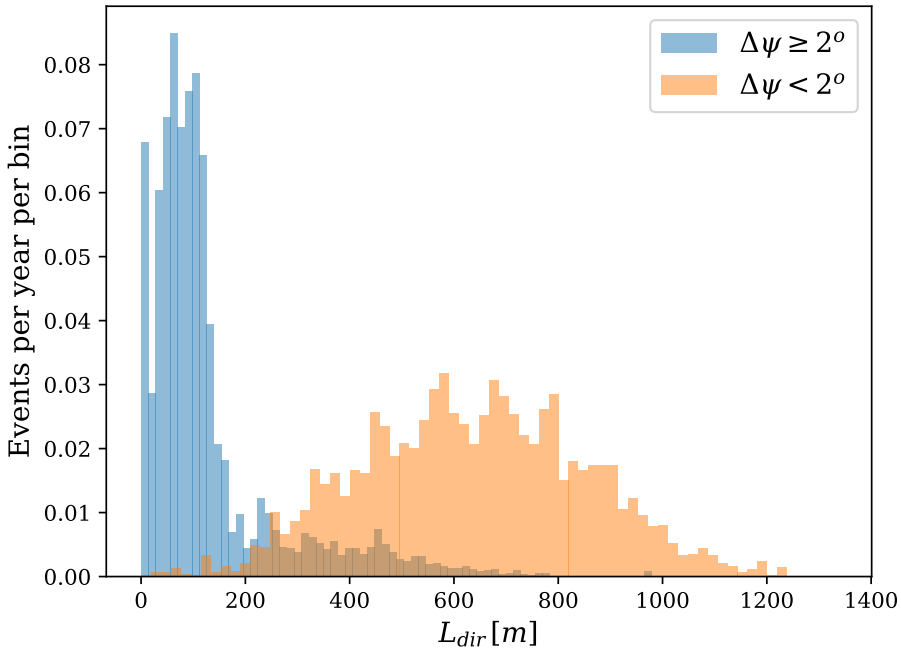

(b)

Figure 5.4: Reconstructed track length distributions of (a) track events and cascade events, and (b) well-reconstructed (angular error $<$ 2 degrees) track events and mis-reconstructed ((angular error $\geq$ 2 degrees) track events.

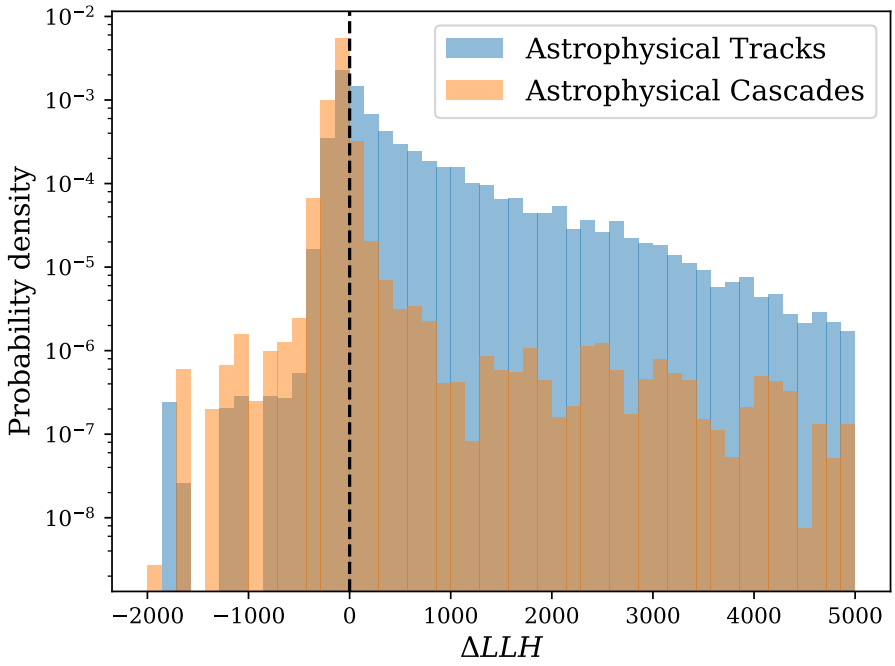

Figure 5.5: Log-likelihood difference distribution of tracks events and cascade events. The cut at 0 is represented by the vertical dashed line.

log-likelihood ratio) hence reflects which hypothesis fits the data better. The distributions of the log-likelihood difference (ΔLLH) are shown in Figure 5.5. Most of the cascade events have ΔLLH below 0, so the cut is set there to further remove them.

Q is the total charge of photoelectrons deposited in the detector within 3 μs from the time of the interaction. $Q_i(\theta_z)$ are two sets of cosine zenith-binned minimum charge thresholds, one for the gold alerts and one for bronze alerts. The values are shown in Table 5.3. This requirement is implemented to achieve the desired signalness for gold (50%) and bronze (30%) alerts, based on the fact that the atmospheric neutrino spectrum is softer than the astrophysical neutrino spectrum, and it is zenith-dependent. By requiring a minimum charge, it effectively removes the lower energy atmospheric neutrino events from the sample, hence improving the signal purity.

5.6 Performance

IceCube is expected to issue in total ~ 30 alerts per year, with ~ 13 being Gold and ~ 17 being Bronze. The expected numbers of gold and bronze alerts from all event streams (GFU, EHE, and HESE) are tabulated in Table 5.4. These values are calculated using the diffuse neutrino flux reported in [105] and the atmospheric neutrino flux from [104]. The total number of Gold alerts is not the sum of the 3 streams, because some through-going tracks pass the GFU and EHE selections simultaneously. Overlapping between HESE and GFU or EHE, on the contrary, is negligible. As of the end of January 2021, IceCube has issued 18 Gold alerts and 26 Bronze alerts, in good agreement with the expected alert rate.

Table 5.4: Expected and observed passing rates for Gold and Bronze selections. All values shown are events per year. Because of the overlap between GFU and EHE, the total rate of Gold alerts is not the sum of all selections. The observed rate is calculated using the number of alert issued between June 2019 and January 2021.

	Gold	Bronze
Astrophysical Signal ($E^{-2.19}$)	6.6 (Total) 5.1 (GFU) 0.5 (HESE) 2.1 (EHE)	2.8 (Total) 2.5 (GFU) 0.3 (HESE)
Atmospheric Backgrounds	6.1 (Total) 4.7 (GFU) 0.4 (HESE) 1.9 (EHE)	14.7 (Total) 13.8 (GFU) 0.9 (HESE)
Observed rate	11.1 (Total)	16.1 (Total)

The expected median angular resolution of the alerts, which is defined as the angular difference between the incoming direction of the neutrino and the reconstructed direction, are shown in Figure 5.6. For both through-going and starting tracks, the angular resolutions are below 1 degree. It can be seen that the Gold alerts have a worse resolution than the Bronze alerts in the low energy regime. For the through-going tracks, this behavior is caused by near-vertically upgoing events, which are more difficult to reconstruct due to the inter-string spacing. For starting tracks, the poorer resolution is caused by the bright cascade at the interaction vertex. This median angular resolution, along with a 90%-tile

angular resolution, are included in the initial message as the 50% and 90% uncertainties of the reconstructed direction of the alert event. It should be noted that these two uncertainties do not take the effect of ice properties into account, but it will be addressed in the more sophisticated reconstruction.

5.7 Discussion

The realtime system has been updated and running since June 2019. The changes have successfully increased the rate of alerts and reduced the rate of retractions. The Gold and Bronze classification also clarified the interpretation of the alerts. However, there are rooms for future improvement. The most prominent one is the online reconstruction for starting track events. Currently, starting tracks are reconstructed with the SplinMPE (subsection 3.4.3) method, which uses an infinite track hypothesis in the likelihood function. As a result, this reconstruction method is not appropriate for a starting track when the light from the hadronic cascade outshines the light from the muon track, and leads to the mis-reconstructed events observed in both the data and simulations. Many starting tracks with high signalness are thus filtered due to poor online reconstruction. The most promising way forward is to introduce a deep neural network (DNN) for event classification and reconstruction algorithm [106]. It has been applied to IceCube cascade alerts and showed remarkable improvement on both computation speed and angular resolution over the conventional liklihood-based method. Although the application of DNN on starting track events is not ready, some preliminary tests have shown that a reconstruction based on convoluted neural network (CNN) architecture can provide a reliable direction when the SplineMPE method fails.

As a closing remark, the prospective realtime system for IceCube Gen2, the next generation neutrino telescope, is going to bring exciting changes to the field of high energy astronomy. The proposed 8 times increase in the instrumented volume will lead to a few significant improvements. First, the alert rate is estimated to increase by about five-fold

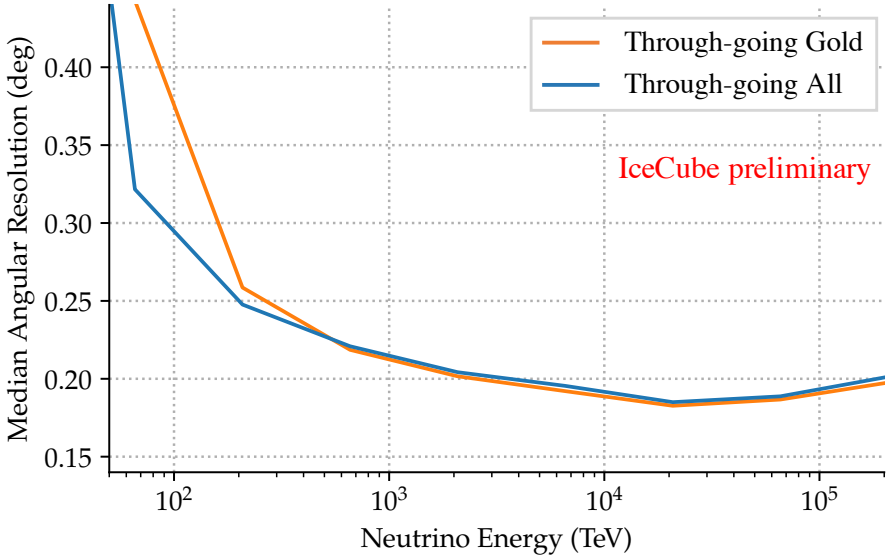

(a)

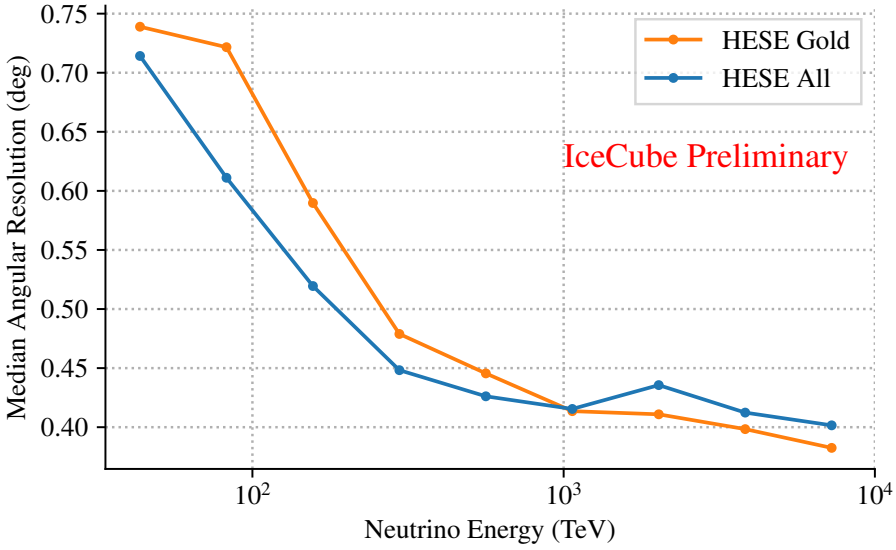

(b)

Figure 5.6: Median angular resolution of (a) GFU and EHE alerts and (b) HESE alerts, as a function of the neutrino energy. In both figures, 'All' means both Gold and Bronze alerts.

[107]. Second, the larger size of the detector will improve the reconstruction for both direction and energy. The improved direction reconstruction will reduce the chance coincidences between neutrino alerts and uncorrelated sources. The improved energy reconstruction will allow a better separation between astrophysical neutrinos from the background. With a larger number of neutrino alerts of astrophysical origin, observing coincident detection or not are both interesting. If a coincidence is observed, the neutrino can provide additional information for the high energy environment of the source. If there are many alerts without counterparts, it can be a hint of the existence of a group of opaque cosmic accelerators. Either way, the realtime system of IceCube Gen2 will play a bigger role in multimessenger astronomy.

CHAPTER 6

SEARCH FOR NEUTRINOS FROM X-RAY BINARIES

6.1 Introduction

In the search for the origin of UHECR, X-ray binaries (XRBs) have been long-standing candidates of Galactic CR accelerators. An XRB is composed of a compact object and a companion star which is non-degenerate in most cases. The compact object can be either a black hole or a neutron star, while the companion stars can be massive giants, main sequence stars, or white dwarfs. A simple classification of XRBs can be done based on the mass of the companion star: High Mass X-ray Binaries (HMXBs) if the mass is above $10\ M_{\odot}$ and Low Mass X-ray Binaries (LMXBs) if the mass is below $1\ M_{\odot}$. If the companion mass lies between $1 - 10\ M_{\odot}$, the binary system can be classified as Intermediate Mass X-ray Binary (IMXB), but such binaries are expected to evolve to LMXB quickly by mass transfer, so only a few have been observed [108]. It must be noted that this classification is inadequate to generalize the properties of XRBs.

As the name suggested, XRBs emit X-ray radiation with a typical flux in the order of $10^{-10}\ \mathrm{erg\,cm^{-2}\,s^{-1}}$ at the energy range between $1 - 10$ keV. The X-ray radiation is powered by the accretion of matter flowing from the companion star to the compact object. XRBs are known to transit between different accretion states, which can be inferred from their spectral properties. There are three typical states, known as high/soft, low/hard, and intermediate. In the high/soft (low/hard) state, the luminosity is high (low) compared to the Eddington luminosity and the spectrum is soft (hard). It is believed that the thermal emission from the disk dominates the luminosity in the high/soft state, while a broadband component, likely from inverse Compton emission, dominates in the low/hard state [109]. In the intermediate state, the contributions from these two mechanisms are comparable.

Some of the XRBs exhibit strong radio jet emission, in a way similar to that of active galactic nuclei (AGNs), and are thus known as microquasars. Examples of microquasars include Cygnus X-1, SS433, and Cygnus X-3. In recent years, they have been observed to emit VHE gamma rays [110][111]. Both hadronic and leptonic models of the VHE gamma rays have been proposed, but the exact emission mechanism remains an open question to this date. As described in chapter 1, high energy neutrinos are counterparts to the VHE gamma rays if the hadronic model is true. Thus, detecting high energy neutrinos from XRBs can indisputably confirm the presence of hadronic component in them and establish XRBs as Galactic CR accelerators.

Searches for neutrinos from XRBs have been conducted by IceCube [112] [113] and Antares [114]. In IceCube's analyses, the hypothesis that XRBs were periodic emitters, i.e., the neutrino emission varies periodically as the orbital period of the binary system, was tested. For Antares' analysis, it tested the hypothesis that neutrino emission was correlated with the X-ray flares of the XRBs. Neither study detected a significant neutrino signal. In this chapter, a new point source analysis for XRBs, which I designed and conducted, will be discussed in detail. In this work, the periodic emission hypothesis is revisited using 7.5 years of IceCube's muon neutrino data. It also features an expanded XRB catalog and a significantly improved methodology to enhance the sensitivity for a wider range of emission scenarios.

6.2 Neutrino Production Models

A plethora of models have been proposed for different neutrino production mechanisms that are possible in some XRBs [115][116][117][118][119][120]. For example, [116] provided a model for LS I +61 303 to produce TeV neutrinos, as illustrated in Figure 6.1a. In the model, the jet is assumed to contain a hadronic component, so relativistic protons can be found inside the jet. Using the Larmor radius as an argument, it is possible for the system to accelerate the protons to PeV scale energy. As the compact object (CO) moves

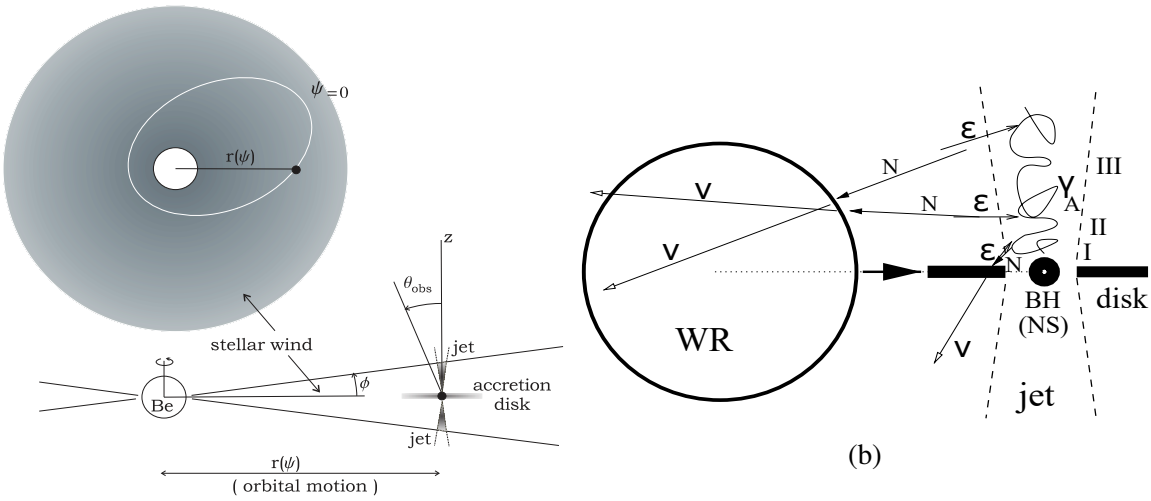

Figure 6.1: (a)A sketch of the system of LS I +61 303. Figure is from [116] (b) A sketch of the the system Cyg X-3. Figure is from [117].

around the Be star donor in an elliptical orbit (eccentricity = 0.72), some particles in stellar wind may be able to penetrate into the jet and collide with the relativistic protons. Thus, pions are produced via the pp interaction chain (chapter 1) from these collisions, and from their subsequent decay a neutrino flux is formed. The predicted neutrino production rate and maximum neutrino energy depend on the wind density and velocity, both of which depend on the distance from the donor. Due to the elliptical nature of the orbit, the neutrino emission should be modulated by the orbital period.

A similar model for TeV neutrino production in Cyg X-3 was proposed by [120] and [117]. In this model, nuclei are accelerated inside the jet, and the jet is divided into three regions, as shown in Figure 6.1b. In region I, the nuclei are disintegrated by the X-ray photons emitted from the inner disk, and the product nucleons can undergo photo-meson production ($p\gamma$) with the X-ray photons from either the inner disk or the synchrotron radiation produced by electrons inside the jet. The resultant neutrino flux from region I is calculated in [121].

In region II, the photon field is dominated by photons emitted by the accretion disk. These photons are energetic enough to disintegrate the nuclei if the collision is head-on.

However, the product nucleons cannot perform photo-meson production efficiently with the accretion disk radiation. Therefore, the majority of the nucleons will escape the jet region and propagate towards the accretion disk. Neutrinos are produced by the collisions between the disk matter and nucleons via pp pion production. In region III, photons from the Wolf-Rayet (WR) star donor dominate the photon field. The nuclei are also photo-disintegrated in head-on collisions with these photons, but the product nucleons will be propagating towards the WR star. Neutrinos are then produced by the collision with the matter in the atmosphere of the WR star. The neutrino spectrum from region III is predicted to be modulated by the orbital period, because the production should reach a maximum when the compact object is behind the donor [117].

Neutrino production is not limited to microquasars. Neutrino production model for A 0535+26, an XRB without a radio jet, was proposed in [115]. This model describes an accreting neutron star system, in which the magnetosphere is divided into different zones. Due to the different rotation speeds of these zones, electrostatic potential differences are formed between them. Protons can be accelerated when they cross the zones while moving along the magnetic field lines. Neutrinos can be produced when the protons impact on the accretion disk, given that the disk grammage is suitable for pion production to occur. Since the disk grammage varies as the orbital position, the resultant neutrino spectrum is also periodically modulated.

Since modulated neutrino emissions are commonly predicted by different neutrino emission models for XRBs, testing XRBs as periodic neutrino point sources is theoretically justified. A periodic signal also allows a new dimension of separating signal events from background events. In a time-integrated analysis, signal events are identified by spatial clustering and a power law spectrum. However, the uncertainties in the reconstructed direction and energy are large. If signal events are clustered in a certain phase, events in the off-phase can be easily treated as background. Thus, there is also practical advantage to perform a periodic point-source analysis.

6.3 Event Selection

This analysis uses a pre-curated data set known as the GFU sample [122]. The goal of this data set is to select well-reconstructed track-like events that are caused by muon neutrinos. The event selection begins after the SMT8 trigger. The triggered events are then reconstructed with the line-fit method and SPE method (subsection 3.4.2. At this step, the event rate is about 2.7 kHz and the sample is dominated by atmospheric muon events.

6.3.1 Muon Filter

The first filter applied to the data is the Muon Filter. Based on the reconstructed zenith angle θ, the filter divides the events into up-going ($\theta \geq 78.5^o$) and down-going ($\theta < 78.5^o$), and applies a cut for each group. For upgoing events, the cut is

$$\frac{\log \mathcal{L}}{N_{ch} - 3} \leq 8.7, \tag{6.1}$$

where $\mathcal{L}$ is the maiximized likelihood of the reconstruction, and N_{ch} is the number of hit DOMs. This cut is implemented to ensure reconstruction quality and the events being track-like. For downgoing events, the cut is

$$\log_{10}(Q_{\text{tot}}) > \begin{cases} 3.9 \cos\theta + 0.65 & \cos\theta \leq 0.5 \\ 0.6 \cos\theta + 2.3 & \cos\theta > 0.5 \end{cases} \tag{6.2}$$

where Q_{tot} is the total deposited charge of the event. This cut is implemented to remove atmospheric muons, which are less energetic than astrophysical neutrinos, by requiring the events to have higher energy. After the muon filter, the event rate is reduced to ~ 40 Hz.

6.3.2 OnlineL2 Filter

Events passing the Muon Filter are then subjected to the OnlineL2 Filter. First, the reconstructed directions of these events are refined with a 2-iteration SPE (SPE2) fit followed by an MPE fit. A set of variables for each event are calculated based on the MPE reconstruction. Then, a set of cuts [123] are applied to the events to remove atmospheric muon events. This reduces the event rate to ~ 6 Hz. After the cut, the remaining events are reconstructed with the SplinMPE method, and their energies are estimated with the MuEx method (details in subsection 3.4.5). More event properties are also calculated at this step, which provides the variables for the cut in the next filter.

6.3.3 GFU Filter

The GFU filter is the last step of the event selection. After OnlineL2, the sample is still overwhelmed with background events. In the Northern sky ($\theta > 82^o$), the background is dominated by mis-reconstructed downgoing muons and mis-reconstructed cascade events. In the Southern sky ($\theta \leq 82^o$), the background is composed of mostly atmospheric muons. Since it is inefficient to remove background events with simple cuts that involve only two to three variables, GFU filter incorporates two boosted decision trees (BDTs), one trained for each hemisphere, to perform a hyper-dimensional cut that involves more than 16 variables on the data. Both BDTs are trained to ensure the quality of the reconstruction and the topology of the events. However, for the Southern sky's BDT, it also features variables to remove events that are likely caused by a bundle of multiple muons. Since atmospheric muons and atmospheric neutrinos are product of air showers, muon bundles are signature of atmospheric events. For the detail of the variables used, please refer to [122].

6.3.4 GFU Data Set

The GFU data set used in this analysis is version GFUv002p05. It composes of 1,501,394 events collected between May 13, 2011 and October 14, 2018, over a total livetime of

2616 days. The directions and energies are reconstructed with SplineMPE and MuEX, respectively. The directional uncertainties are estimated with the Paraboloid method. The expected rates of signal and background events are calculated using Monte Carlo simulations. For the signal rate, it is calculated using the astrophysical neutrino flux reported in [105], which has a spectral index of $\Gamma = 2.19$. For the background rate, the atmospheric neutrino rate is calculated using the model reported in [104], while atmospheric muon rate is calculated with [124]. Figure 6.2 shows them as functions of cosine of the reconstructed zenith. The data is dominated by atmospheric neutrinos in the Northern sky ($\cos(\theta) \leq 0.14$) and by atmospheric muons in the Southern sky. The definition of sky regions is an IceCube convention, based on the Earth's ability to block atmospheric muons. This boundary Since the signal component is more suppressed in the Southern sky, the sensitivity and discovery potential (see definition in subsection 6.5.6) for a point source analysis in this region is usually orders of magnitude worse than the Northern sky. Therefore, this analysis tests only X-ray binaries in the Northern sky. The event distributions along the reconstructed azimuthal angle are shown in Figure 6.3, and it can be seen that all components are almost isotropically distributed. The layout of strings does not impose an significant effect on events' detection.

The event rates as functions of the reconstructed energy (MuEX) for $\theta > 90^o$ and $90^o > \theta > 60^o$ are shown in Figure 6.4. In both zenith bands, events with a higher reconstructed energy also have a higher probability to be astrophysical neutrinos. This shows that the reconstructed energy, aka the energy proxy, can be used to distinguish between astrophysical neutrinos from the background and improve the sensitivity of the analysis.

The angular errors of neutrino events are estimated with Monte Carlo simulations. It is done by calculating the angular separation between the reconstructed direction and the true incoming direction of the neutrino. Hence, the angular error accounts both the kinematic angle between the neutrino and the outgoing muon, and the statistical error in the reconstruction, but not the systematic errors of the ice properties. The median angular errors as

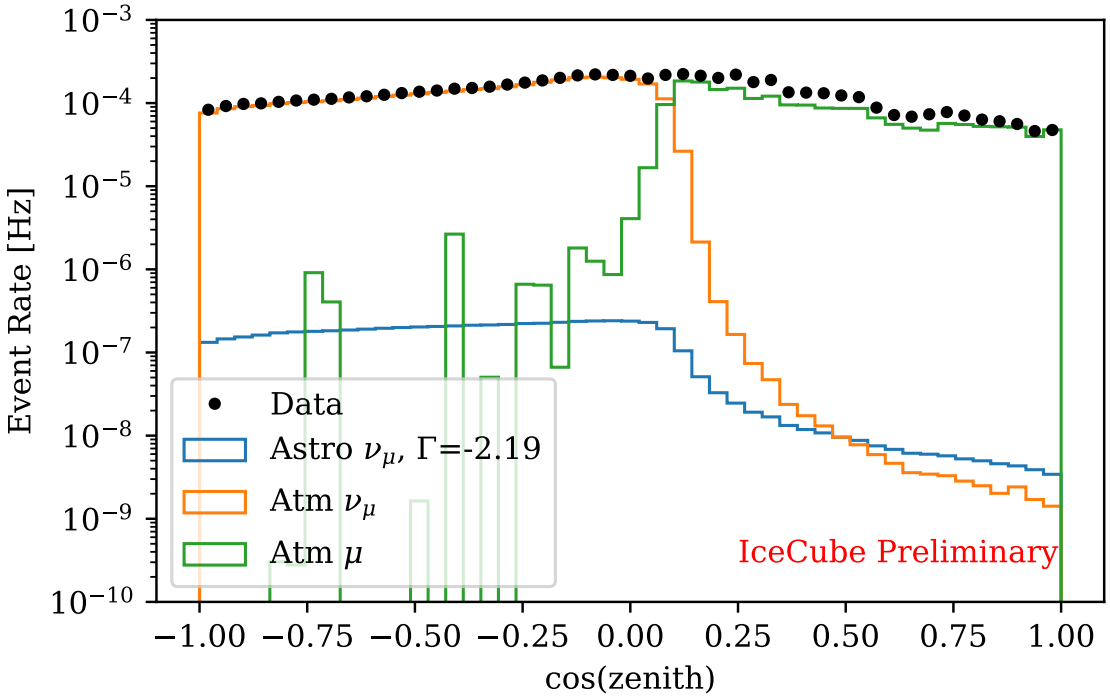

Figure 6.2: Event rates as a function of cosine of reconstructed zenith of data, astrophysical muon neutrinos, atmospheric muon neutrinos and atmospheric muons. The data is from GFUv002p05. Rate of astrophysical muon neutrino is calculated with diffuse neutrino flux with $\Gamma = 2.19$ [105]. Rate of atmospheric neutrino is calculated with model from [104]. Rate of atmospheric muon is calculated with [124].

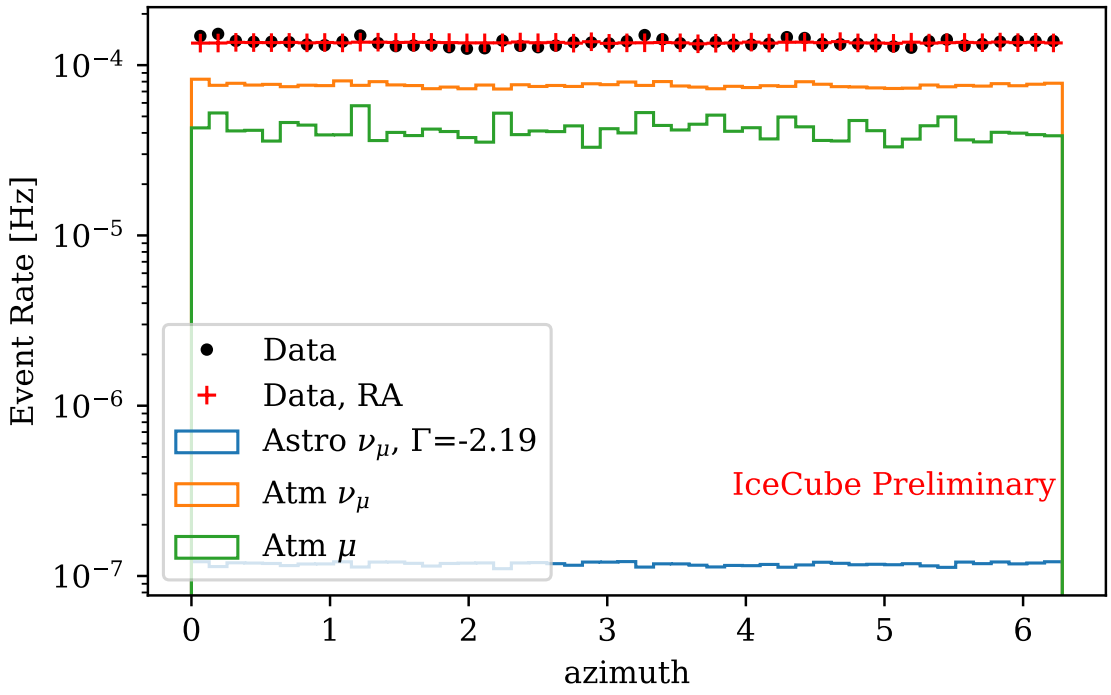

Figure 6.3: Event rates as a function of the reconstructed azimuths of data, astrophysical muon neutrinos, atmospheric muon neutrinos and atmospheric muons. The is a companion plot to Figure 6.2.

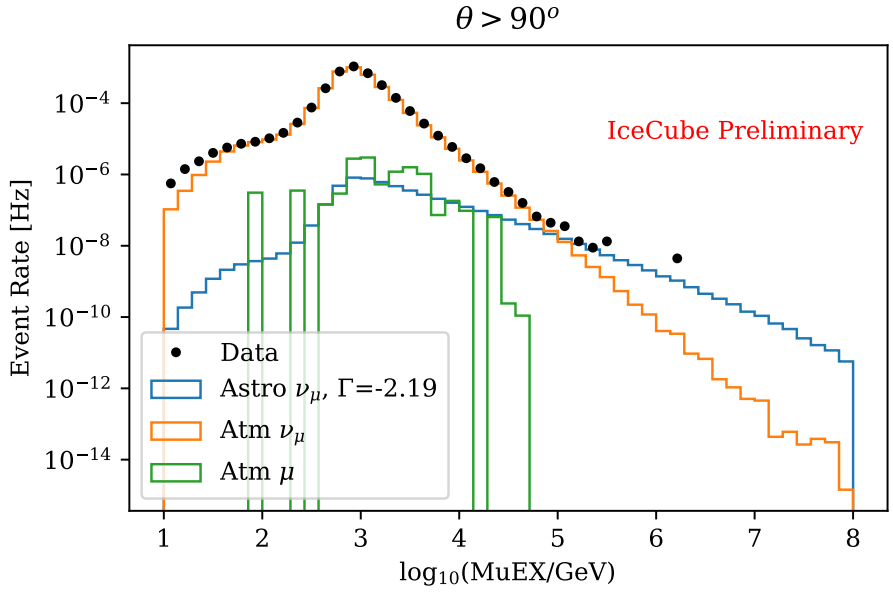

(a)

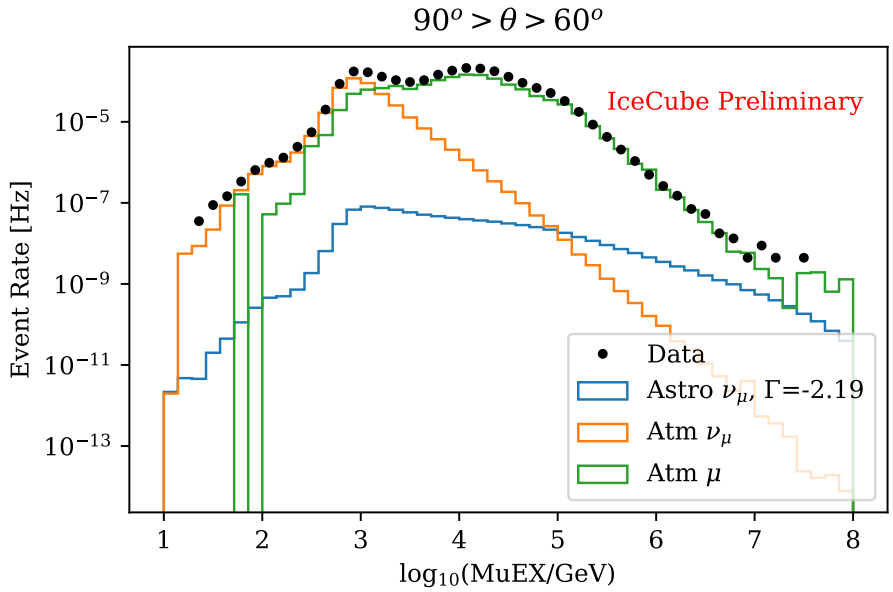

(b)

Figure 6.4: Companion plots of Figure 6.2. Event rates of different components as a function of the reconstructed energy from MuEX. Two zenith bands are shown here; (a) $\theta > 90^o$ and (b) $90^o > \theta > 60^o$. It should be noted that the astrophysical component was not fitted with GFU data set.

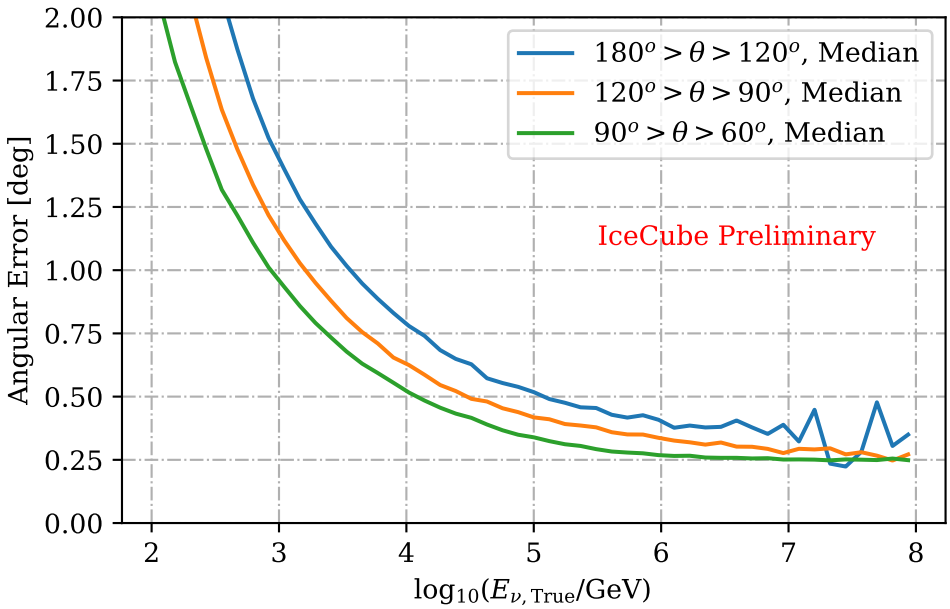

Figure 6.5: Companion plot of Figure 6.2. Median angular error of neutrino event as a function of the true neutrino energy. The large fluctuation in the high energy regime of the $180^o > \theta > 120^o$ band is due to limited statistics, which is caused by the Earth attenuation of high energy neutrinos.

functions of the true neutrino energy in three zenith bands are shown in Figure 6.5. The all-sky median angular error is $\sim 0.7^o$. Since the median angular error is above 0.25^o for even the highest energy events, a lower bound of 0.2^o is imposed on the estimated directional uncertainty.

The reconstructed directions are expressed in zenith and azimuthal angles, which are defined locally by the detector's orientation. Due to Earth's motion and rotation, neutrinos from a point source are spread around a zenith band. Therefore, the directions have to be converted to equatorial coordinates (J2000 epoch), i.e. declinations and right ascensions (RAs), for a point-source analysis. Exact conversion is nontrivial due to factors such as offset from the geographical south pole and precession. However, for illustration, declinations can approximated as $\delta = \theta - \pi/2$. The event distribution along RA is shown in Figure 6.3 as red crosses. Similar to the case of azimuthal angles, background events are also isotropically distributed in RA.

6.4 Source Catalog

The X-ray binaries tested in this analysis are selected from HMXBCAT[125], LMXBCAT[126], TeVCAT[127], and 4FGL[128]. Because of the poor sensitivity in the Southern sky, only XRBs with a declination north of -5^o are considered. Further more, XRBs without a resolved orbital period are also excluded, because the goal of this analysis is to use the period information to facilitate the point-source search, instead of identifying an unknown periodic signal. The final catalog consists of 55 sources, with 31 from HMXBCAT, 22 from LMXBCAT, 1 from TeVCAT and 1 from 4FGL. The equatorial coordinates and measured orbital periods of these source are listed in Table A.1.

6.5 Method - Unbinned Likelihood Ratio

An unbinned likelihood ratio method is used to identify if any XRB in the catalog is a periodic neutrino point source. In this method, the events are assumed to consist of two components, one for the signal, i.e., those from the point source, and one for the background. The contribution from the signal component is unknown, so is left as a free parameter. The best estimates of the signal's contribution, along with other parameters that characterize the signal component, could be obtained by maximizing the likelihood function, which is defined as

$$\mathcal{L}(n_s, ...) = \prod_i^N \left[\frac{n_s}{N} \mathcal{S}_i + \left(1 - \frac{n_s}{N}\right) \mathcal{B}_i \right], \tag{6.3}$$

where N is the total number of events in the data set, n_s is the number of signal events, and $\mathcal{S}_i$, $\mathcal{B}_i$ are the signal and background probability density functions(PDFs) evaluated for event i, respectively.

6.5.1 Signal PDF

For an XRB located at $\mathbf{x_s}$, the signal PDF could be written as

$$\mathcal{S}_i = \mathcal{P}\left(\mathbf{x_i} - \mathbf{x_s}, \sigma_i\right) \times \mathcal{E}\left(E_i|\gamma\right) \times \Psi\left(t_i|\kappa, \Phi_0, P\right). \tag{6.4}$$

$\mathcal{P}$ is the spatial PDF of the signal events, also known as the point spread function (PSF). Although the exact PSF is not known, it is approximated by a Gaussian distribution given by

$$\mathcal{P}\left(\mathbf{x_i} - \mathbf{x_s}, \sigma_i\right) = \frac{1}{2\pi\sigma_i^2} \exp\left(-\frac{\left(\mathbf{x_i} - \mathbf{x_s}\right)^2}{2\sigma_i^2}\right), \tag{6.5}$$

where $\mathbf{x_i} - \mathbf{x_s}$ is the angular difference between the reconstructed direction and the source location, and σ_i is the per-event estimated angular uncertainty. $\mathcal{E}$ is the signal events' energy PDF, which is given by

$$\mathcal{E}(E_i|\Gamma) = \left(\frac{E_i}{E_0}\right)^{-\Gamma} \times A_{\text{eff}}(E_i, \delta_i), \tag{6.6}$$

where E_i is the reconstructed energy from MuEX, E_0 is the pivot energy, Γ is the spectral index, and A_{eff} is IceCube's effective area evaluated at the energy E_i and declination δ_i of the event. The form of $\mathcal{E}$ is motivated by the assumption that astrophysical neutrino spectrum follows a power-law, and A_{eff} is included to take the detector's response into consideration. Since no neutrino flux from XRB has been measured, Γ is left as a free parameter.

Ψ is the signal phase PDF. As XRBs are hypothesized to be periodic sources, the signal events are assumed to cluster around a certain phase. The PDF is modeled by a von Mises distribution, which is given by

$$\Psi = \frac{1}{2\pi I_0\left(\kappa\right)} \exp\left[\kappa \cos\left(\phi_i\left(t_i|P\right) - \Phi_0\right)\right], \tag{6.7}$$

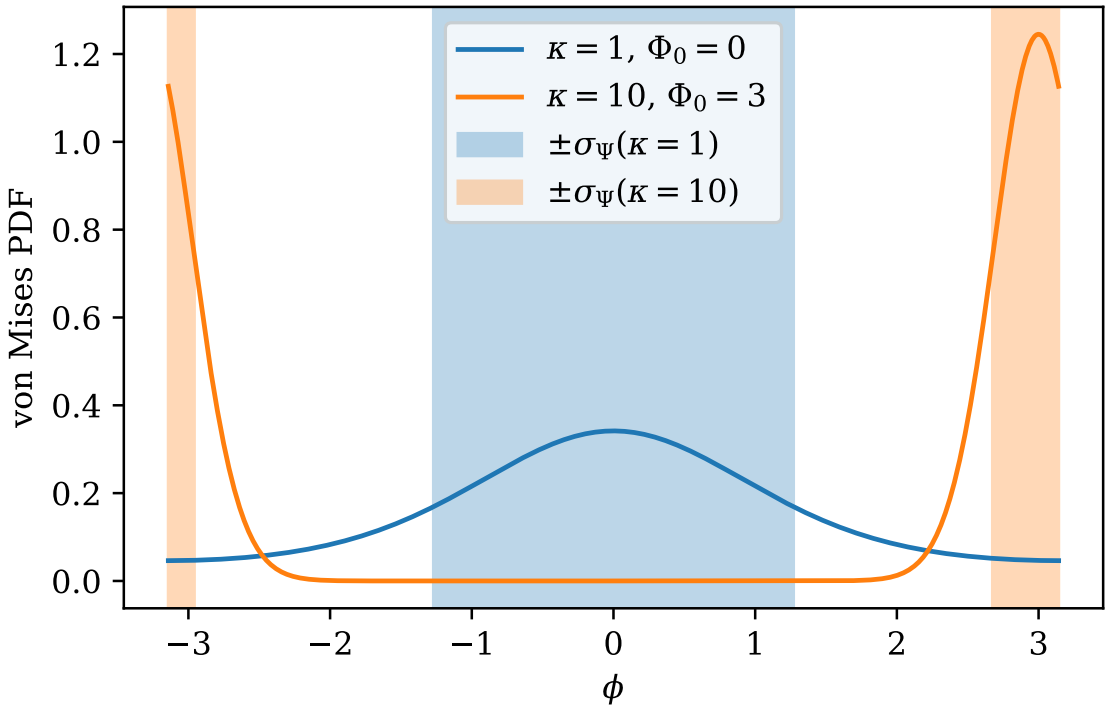

Figure 6.6: von Mises PDF for different concentration parameter κ. The regions covered by $\pm$ 1 standard deviation σ_Ψ around the median are shaded in the corresponding color.

where ϕ_i is the phase of the event, κ is a measure of the concentration of the distribution, and Φ_0 is the median of the distribution. I_0 is the modified Bessel function of the first kind. The effect of different κ and Φ_0 is shown in Figure 6.6. As a reference, the area $\pm$ 1 standard deviation of the distribution for the respective κ is shaded in the same color as the curve, and 68% of the neutrinos are emitted within the shaded region per cycle. For later discussion, the duty cycle of the neutrino emission is defined as standard deviation divided by 2π. ϕ_i is calculated from the event arrival time t_i and the source's orbital period P, i.e., $\phi_i = (t_i - T_0)/P$, where T_0 is set to MJD 55690. κ, Φ_0, P, are free parameters that need to be determined.

In the previous periodic point source analyses, the signal phase PDF was modeled with a Gaussian distribution over the range of the folded phase [113]. However, the Gaussian distribution is not a periodic function. If the peak of the distribution is found near the two ends of the phase range, part of the peak would be cut off by the boundaries, which could

lead to a loss of sensitivity. Hence, the von Mises distribution was used instead in this analysis for its periodic nature.

Furthermore, the source period was fixed in the previous work. It was then reported that the sensitivity would be adversely affected if the neutrino flux was modulated by a frequency modestly different from the given orbital period [113]. This problem is exacerbated in this analysis because the error in the phase would accumulate over the extended experiment live time. Therefore, in my work, the source period was set as a free parameter to retain sensitivity in the said scenario.

6.5.2 Background PDF

The background PDF $\mathcal{B}_i$ is defined as

$$\mathcal{B}_i = \mathcal{P}_{Bg}(\delta_i)\mathcal{E}_{\mathrm{Bg}}(E_i|\delta_i) \times \frac{1}{2\pi}. \tag{6.8}$$

$\mathcal{P}_{\mathrm{Bg}}$ and $\mathcal{E}_{\mathrm{Bg}}$ are the declination and energy PDFs for background events. These PDFs are constructed from the empirical distributions of the corresponding observables for the GFU sample, similar to those shown in Figure 6.2 and Figure 6.4, based on the assumption that the sample is dominated by background events. The background events are assumed to be uniformly distributed in phase, independent of the source period. Rates of atmospheric neutrinos and atmospheric muons depend on the temperature and density of the upper atmosphere, which result in a seasonal variation that has been detected[129][130]. However, the effect is negligible at the final sample level according to [131] and most of the XRBs have a period much shorter than a year.

6.5.3 Test Statistics

The test statistic Λ for each source location is given

$$\begin{aligned}\Lambda = &-2\log\left[\frac{\mathcal{L}\left(n_s=0\right)}{\mathcal{L}\left(\hat{n}_s,\hat{\gamma},\hat{\kappa},\hat{\Phi}_0,\hat{P}\right)}\times\frac{2\pi}{\sigma_\Psi(\hat{\kappa})}\right]\\ &-2\frac{(\hat{P}-P_{exp})^2}{2\sigma_P^2}.\end{aligned} \tag{6.9}$$

The first term on the right hand side is the log-likelihood ratio of the null hypothesis ($n_s = 0$ or background-only hypothesis) to the alternative hypothesis (signal-plus-background hypothesis). The free parameters in the alternative hypothesis are determined by maximizing Λ. The hat symbols indicate the best-fit values. $2\pi/\sigma_\Psi(\hat{\kappa})$ is the marginalization term used to approximate the marginalized likelihood, where σ_Ψ is the circular standard deviation of the von Mises distribution, which is defined as

$$\sigma_\Psi(\kappa) = \sqrt{-2\log\left(\frac{I_1(\kappa)}{I_0(\kappa)}\right)}. \tag{6.10}$$

The usage of the marginalization term is introduced to prevent the minimizer from biasing towards a narrower periodic emission [132]. Such bias occurs due to the fact that more unique possible locations could be fitted for a narrow periodic emission, thus leading to a hidden trial factor.

The second term in the test statistic is the prior probability of the orbital period of the source. It is approximated by a normal distribution centered at the measured orbital period P_{exp}, and σ_P is the reported 1-sigma uncertainty for P_{exp}. This term is added to accommodate the widely varying precision in p_{exp}. Some of the XRBs, such as Cyg X-1 and LS I 61+303, have their orbital period accurately resolved and in good agreement with radial velocity measurements, while some others' periods, such as SAX J0635.2+0533, are derived with a limited amount of observation data. Hence, the role of the prior is to

facilitate the minimization of P with the information provided by the EM measurements of the sources. Practically speaking, the prior can reduce the chance that P getting stuck at the boundary during the minimization and preserve the sensitivity for sources with an precisely measured period.

A more intuitive form for the test statistic can be obtained by expanding Equation 6.9 into

$$\begin{aligned}\Lambda = \sum_{i}^{N} 2\log\left(1 + \frac{\hat{n}_s}{N}\left(\frac{S_i(\hat{\gamma},\hat{\kappa},\hat{\Phi}_0,\hat{P})}{B_i} - 1\right)\right) \\ + 2\log\left(\frac{\sigma_\Psi(\hat{\kappa})}{2\pi}\right) - 2\frac{(\hat{P}-P_{exp})^2}{2\sigma_P^2}.\end{aligned} \tag{6.11}$$

The ratio of $\mathcal{S}_i/\mathcal{B}_i$ can be considered as the weight of event i in the likelihood function, and is frequently used as a parameter to select the most signal-like events. However, its value does not represent the probability of the event being an actual signal.

6.5.4 Skylab

The analysis is performed with Skylab, a Python-based IceCube internal analysis package. Test statistic maximization is carried out using MINUIT's MIGRAD method [133][134]. Bounds are placed on the free parameters to improve the convergence of the minimizer. The lower and upper bounds for all parameters are tabulated in Table 6.1.

Table 6.1: Lower and upper bounds for the free parameters in the likelihood function.

Parameter	Lower Bound	Upper Bound
n_s	0	1000
Γ	1	4
κ	0.5	100
Φ_0	-200π	200π
P	$P_{exp} - 5\sigma_P$	$P_{exp} + 5\sigma_P$

The lower bound of n_s is set as 0 to ensure the best-fit value is non-negative, because a negative n_s is likely to be unphysical. The bounds for Φ_0 are set as $\pm 200\pi$ so the minimizer

will not get stuck at the boundary. The best-fit Φ_0 will be wrapped back to the range of [-pi, π]. The bounds of P are set as ± 5 times the 1-sigma uncertainty σ_P around the measure orbital period, so they are source-dependent.

The ability for this analysis to retrieve a signal is tested by injecting simulated neutrino events, weighted according to IceCube's response for a given neutrino spectrum, into scrambled samples (see next part for details about scrambling). The neutrino spectrum injected is characterised by the free parameters, and modeled as

$$\frac{dN}{dE_\nu} = A \times \left(\frac{E_\nu}{E_0}\right)^{-\Gamma} \times \Psi\left(t_i|\kappa, \Phi_0, P\right) \ , \tag{6.12}$$

where A is the period-averaged flux normalization at E_0, and Ψ is the von Mises distribution PDF. The flux normalization depends on the number of signal events injected $n_{\rm inj}$. The median values of the fitted parameters as a function of $n_{\rm inj}$ are shown in Figure 6.7. The accuracy of the fitting depends strongly on the injection model. Indeed, the parameters are recovered more accurately when there are more signal events. Besides that, the phase distribution concentration κ also have a large effect on the fitting. A more concentrated injection, i.e., larger κ, is usually identified by the analysis more correctly.

6.5.5 Significance Calculation

The significance of each source is calculated by comparing the test statistic from the actual data to those from background-only samples (known as background trials). These background-only samples are prepared by scrambling the arrival times of the events while keeping the other attributes unchanged, such that the event directions are the same in the detector's frame but scrambled in the equatorial coordinate representation. This approach is again justified by the assumption that the data set is dominated by background events, and any existing signal will be delocalized by the scrambling. The background test statistics distribution of Cygnus X-1 is shown in Figure 6.8 as an example.

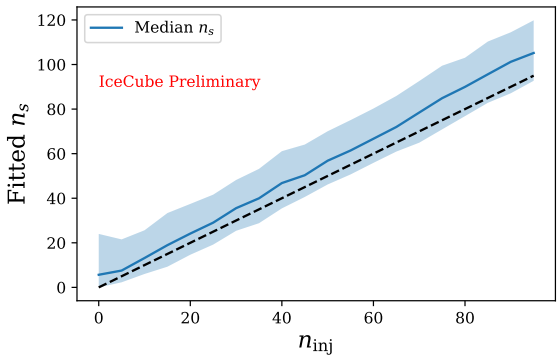

(a) n_s

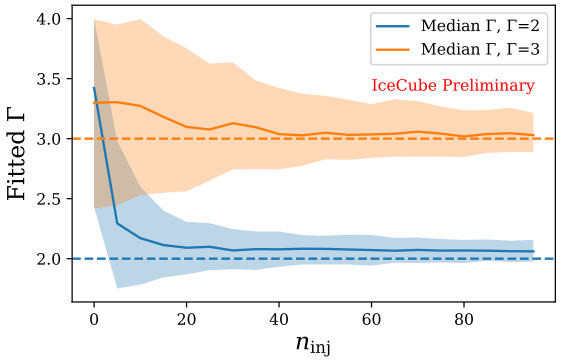

(b) Γ

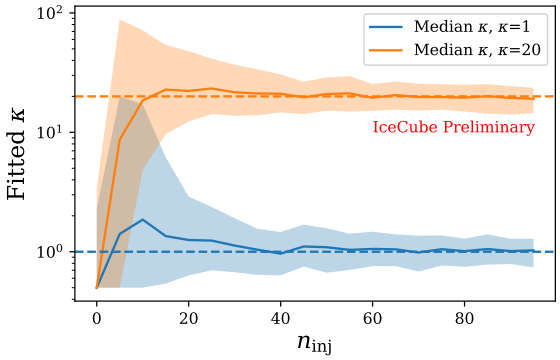

(c) κ

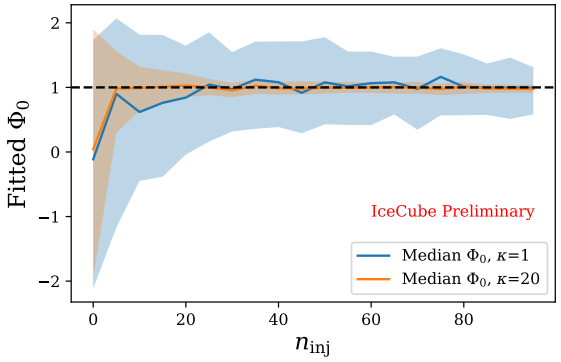

(d) Φ_0

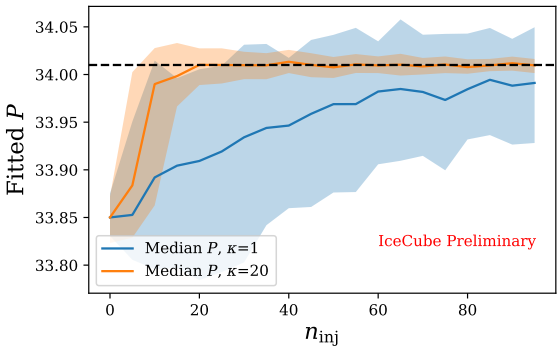

(e) P

Figure 6.7: Median values of the best-fit of the free parameters of GRS 1915+105 as a function of the number of injected signal events. The injected truths are indicated by the dash-line. The shaded regions indicate the 68-percentile centered at the median.

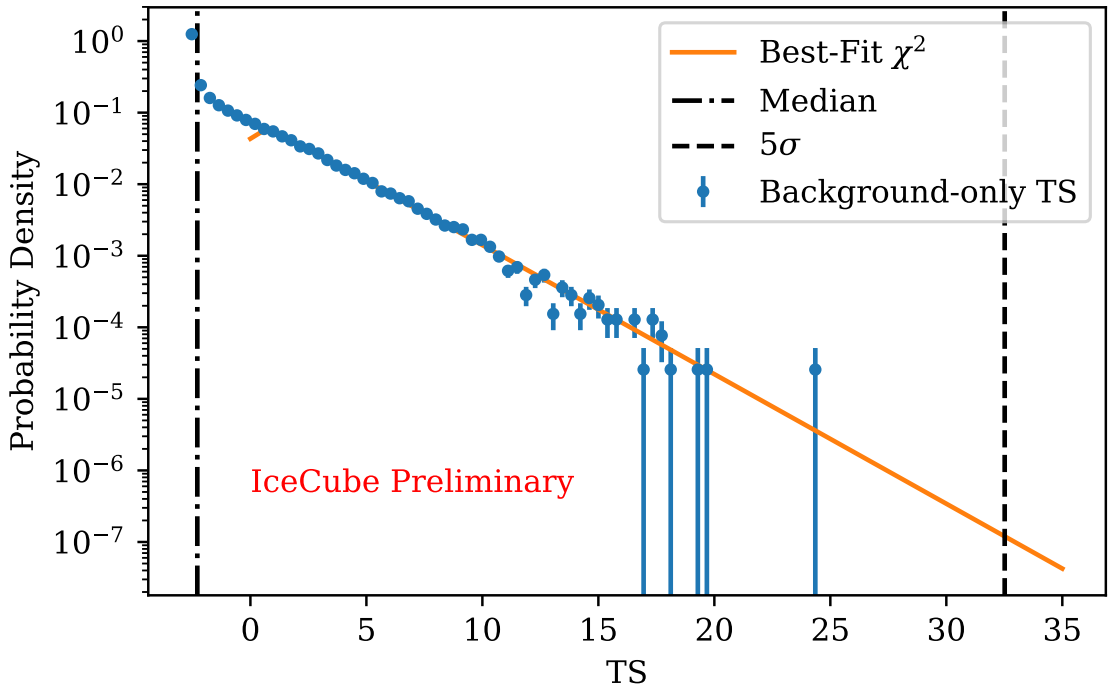

Figure 6.8: An example of 100,000 background trials' test statistics distribution. The source is Cyg X-1. The best-fit χ^2 distribution is also shown. The median and the estimated 5σ TS are also indicated.

For each source, a local p value is obtained by finding the fraction of background trials with test statistics larger than the test statistic observed in the analysis, i.e.

$$p_{\rm local} = N_{\rm bkgtrial}(\Lambda \geq \Lambda_{\rm obs})/N_{\rm bkgtrial}. \tag{6.13}$$

Thus, the local p value is the probability of a background-only sample to produce a test statistic larger than the observed one due to random fluctuations. Since the analysis is performed on multiple sources, the look-elsewhere effect must be taken into account. A global p value is obtained by correcting the minimum local p value among all sources with

$$p_{\rm global} = 1 - (1 - \min(p_{\rm local}))^{N_{\rm src}}, \tag{6.14}$$

where $N_{\rm src}$ is the number of XRB studied in this analysis, which is 55. To claim a discovery of neutrino point source, the global p value must be smaller than 2.87×10^{-7}, so the null-hypothesis is regarded as rejected by data at 5σ level. In this case, the XRB with the minimum $p_{\rm local}$ will be considered as the point source.

6.5.6 Sensitivity and Discovery Potential

The sensitivity of this analysis is defined as the number of signal events required in the signal-injected samples (signal trials) such that 90% of the test statistics from them are above the median of the background trials. Similarly, the 5σ discovery potential is defined as the number of signal events such that 50% of the signal trials' test statistics are larger than 99.99713% (1-side σ) of the background trials'. However, the number of background trials needed to determine the actual 5σ position is computationally prohibitive if carried out for all sources. Therefore, the 5σ level is usually estimated by extrapolating a χ^2 distribution PDF fitted to the background test statistics. This method is based on Wilk's theorem [135], which suggested that the test statistics from the likelihood-ratio tests under a null hypothesis follow a χ^2 distribution when N asymptotically approach infinity. Although

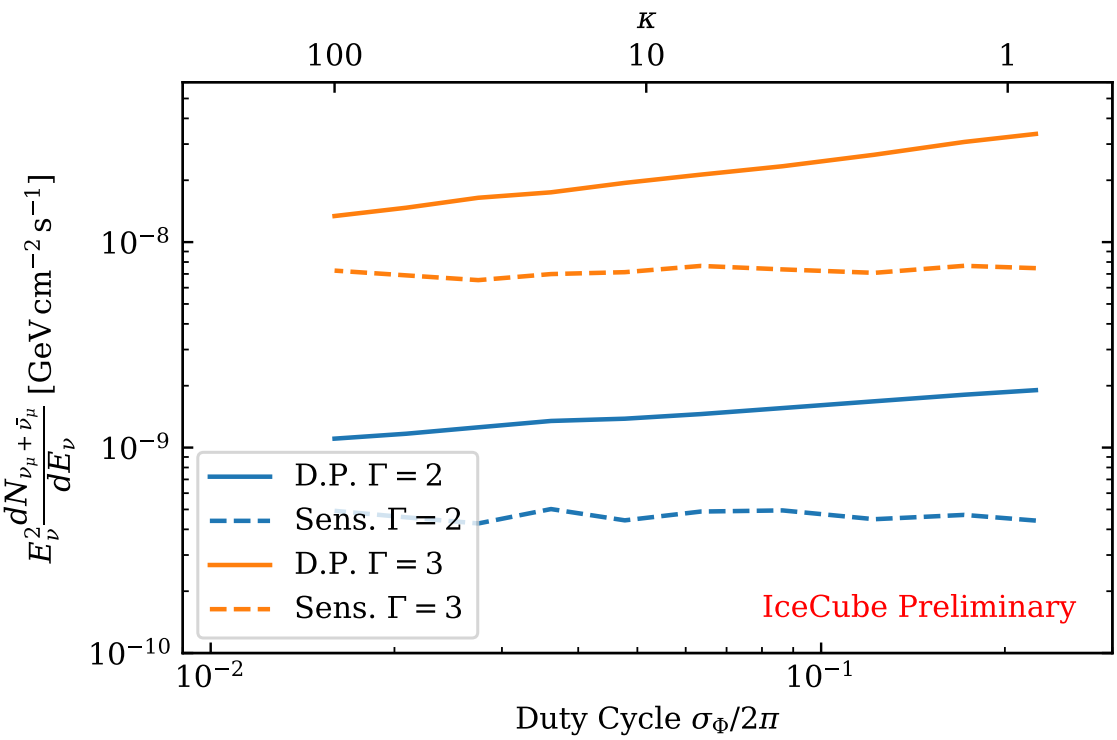

Figure 6.9: Sensitivity and discovery potential of Cygnus X-1 as functions of the concentration parameter κ for both hard (Γ=2) and soft (Γ=3) spectra.

the test statistic defined in this analysis does not match the condition for Wilks theorem to be applicable (due to the presence of the regularization term), χ^2 is found to describe the background test statistics distribution well. Figure 6.8 shows the best-fit χ^2 and the estimated 5σ location as an example.

Figure 6.9 shows the sensitivity flux and discovery potential flux of Cygnus X-1 for different von Mises concentrations κ and spectral indices Γ. The injected events are modulated with a period the same as the measured orbital period of 5.599829 days. The duty cycle of the injection, which is defined as $\sigma_\Phi/2\pi$ and is a function of κ, is shown on the bottom x-axis for reference. The y-axis shows the period-averaged flux normalization at the pivot energy $E_0 = 1\,\mathrm{TeV}$, which is calculated from the number of injected signal events.

From Figure 6.9, it can be seen that the analysis is better at identifying sources with a short duty cycle, as it requires a smaller flux from sources with a larger κ to achieve

discovery. The effect of $kappa$ is more pronounced on softer spectrum sources, which is as expected because the energy PDF becomes less effective in separating signal events from the background when the spectrum is soft, so the separating power of the phase PDF is more important. On the contrary, sensitivities are not affected by the phase concentration. This is because the number of signal events required to reach the sensitivity level is too few for the concentration to take effect.

The effect of a displaced injection period is investigated and illustrated in Figure 6.10. In the figure, the discovery potentials of GRS 1915+105 for three cases with spectral index $\Gamma = 3$ are plotted against different duty cycles. The first case (blue) is that signal events injected are modulated in the same period as the measured orbital period P_{exp}, and the period is fitted during the test statistic maximization. The second case (orange) is that the injection period is offset by one σ_P from P_{exp}, while the period is being fitted. The third case (green) is that the injection period is offset by the same amount as the second case, but the period is not fitted (that is, it is not a free parameter in Equation 6.4) and fixed at P_{exp}. A big difference is seen between the third case and the other two, while the first and second case are very similar. This shows that the period fitting procedure can indeed retain the discovery potential even the neutrinos are modulated slightly different from the measured orbital period. This is a significant improvement over the previous periodic analysis, in which a modest deviation from the measured period would result in a major loss in sensitivity.

6.6 Method - Binomial Test

The unbinned likelihood ratio method is designed to test each source individually, so it is not sensitive to the scenario of a group weak neutrino sources. This drawback can be compensated by performing a binomial test on the point-source analysis' result. The steps for the test are:

1. Rank the local p value obtained from the point source analysis in ascending order,

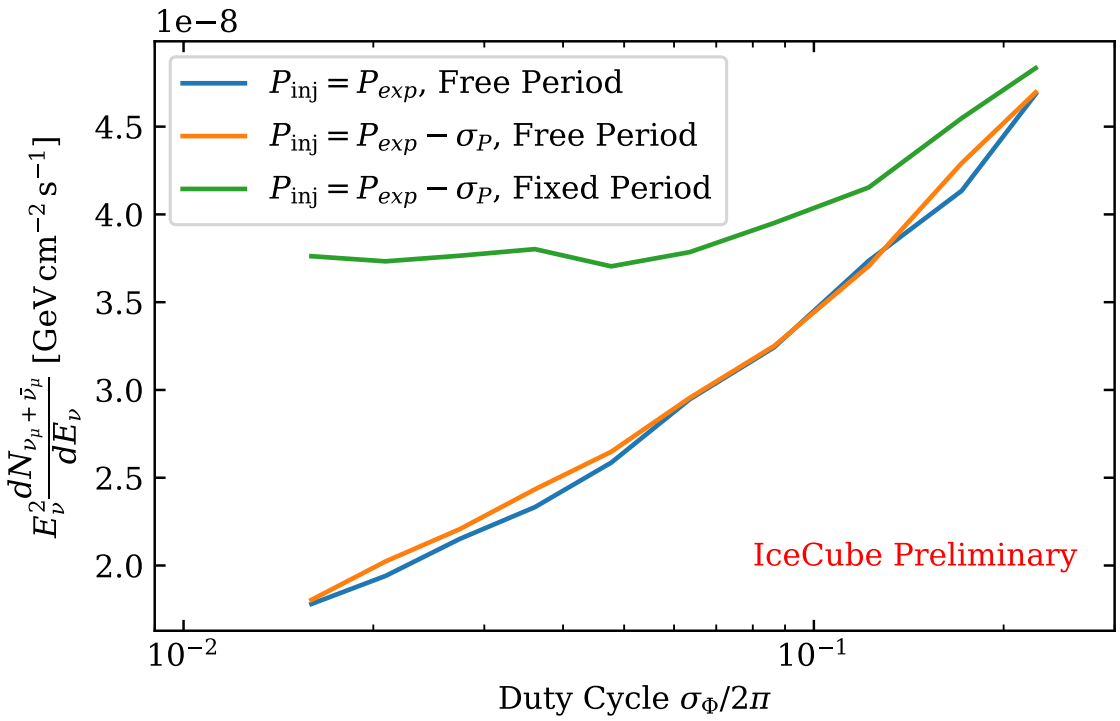

Figure 6.10: Discovery potentials of GRS 1915+105 as functions of duty cycle for different injection scenarios. See text for description.

such that the smallest p value is ranked 1st.

2. For each p value, calculate the binomial probability

$$\mathcal{P}_{\rm bi}(k) = \binom{N_{\rm src}}{k} p_k^k (1-p_k)^{N_{\rm src}-k}, \tag{6.15}$$

where p_k is the k-ranked local p value. $\mathcal{P}_{\rm bi}(k)$ is the probability of finding k sources to have local p value smaller than p_k from catalog of $N_{\rm src}$ sources.

3. The minimum $\mathcal{P}_{\rm bi}(k)$ is chosen as the test statistic $\Lambda_{\rm bi}$.

4. Repeat the steps above with background-only trials to obtain distribution of background test statistics. The significance of the binomial test is obtained by finding the fraction of background trials with test statistic large than $\Lambda_{\rm bi}$.

Since neutrino production in XRBs can be categorized in many different way, it is possible

that neutrino emission is exhibited by a subset of XRBs. One possible key factor is the nature of the compact object, and if it is true, it can be tested by applying the binomial test to each subset of XRBs with the same type of compact object. The XRBs in the catalog are classified into two groups, black hole XRBs (BHXBs) and neutron star XRBs (NSXBs), based on the type of the compact objects. The classifications are listed in the class column in Table A.1, the background test statistics distributions for each group are shown in Figure 6.11.

6.7 Results

Like all other IceCube's analyses, this analysis was also conducted using a blinded technique. Only scrambled data were used during the design stage of the analysis. The analysis was performed on actual data to obtain the results only after the method was finalized and approved by the IceCube Collaboration. The test statistics(TS), best-fit values for the free parameters, and negative-logarithm of the local p values, of the 55 XRBs are tabulated in Table 6.2. The highest significance is found at V635 Cas (=4U 0115+634), which has a local p value $p_{\rm local} = 0.52\%$. After correcting for look-elsewhere effect, the global p value of this analysis is $p_{\rm global} = 24.9\%$. Therefore, the result is compatible with the background-only hypothesis. The neutrino flux upper limits of both hard spectrum ($\Gamma = 2$) and soft spectrum ($\Gamma = 3$) are calculated for each source. The upper limit is defined as the flux required to have 90% of the signal injected trials having test statistics above the observed one. If the observed TS is below the median of the background trials' TS, the sensitivity flux will be reported as the upper limit instead. The upper limits are also listed in Table 6.2.

The binomial tests for BHXBs and NSXBs give test statistics of 0.175 and 0.00345, respectively. They are shown in Figure 6.11 as dashed lines to compare with the background trials. The p values for the tests are: 92.17% for $k = 5$(BHXBs) and 7.66%, which is close to 2 sigma, for $k = 16$ (NSXBs). Therefore, they are also compatible with the background-only hypothesis.

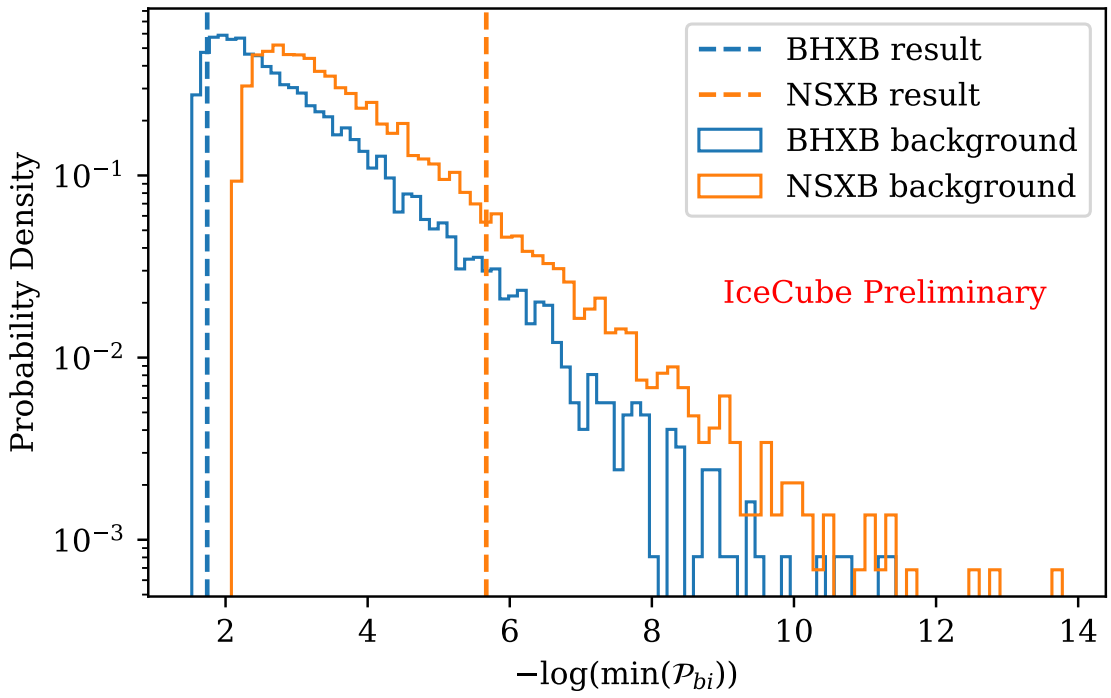

Figure 6.11: Binomial test background TS distributions and the observed test statistics for both BHXBs and NSXBs.

Table 6.2: Results of Periodic Point Source Analysis. The TS, best-fit values of the free parameters, and local p value of each source are shown in the 2nd to 8th columns. The 90% upper limits are shown in the last two columns. These upper limits are calculated with spectral indices of 2 and 3, pivot energy of 1 TeV, and the unit is $\mathrm{GeV}^{-1}\mathrm{s}^{-1}\mathrm{cm}^{-2}$.

Name	TS	n_s	Γ	κ	Φ_0	P	$-\log_{10}(p_{\mathrm{local}})$	U.L. $\Gamma = 2$	U.L. $\Gamma = 3$
AX 1845.0-0433	2.42	30.6	3.93	0.5	5.15	5.7196	1.253	6.9E-16	3.5E-14
IGR J18483-0311	-2.63	0	3.16	0.5	1.32	18.545	0.184	2.66E-16	1.11E-14
XTE J1855-026	-2.54	4.67	3.72	0.5	4.34	6.0741	0.275	2.84E-16	1.08E-14
2S 1845-024	-2.63	0	2.76	0.5	4.81	242.18	0.021	2.44E-16	1.14E-14
4U 1901+03	-2.63	0	3.46	0.5	4.65	22.535	0.177	2.82E-16	1.08E-14
SS 433	-2.63	0	2.76	0.5	3.26	13.068	0.075	2.53E-16	9.95E-15
SAX J0635.2+0533	0.308	18.8	2.93	10.1	0.48	11.168	0.440	3.83E-16	1.47E-14
4U 1909+07	0.14	29	4	0.5	4.93	4.4003	0.754	5.84E-16	1.76E-14
XTE J1859+083	-2.63	0	2.16	0.5	4.29	60.65	0.060	3.1E-16	9.75E-15
4U 1907+09	2.7	37.6	4	0.5	2.97	8.3753	1.221	6.91E-16	2.47E-14
IGR J19140+0951	-0.162	24.6	4	6.27	2.99	13.553	0.710	4.69E-16	1.69E-14
1A 0535+262	-2.63	0	3.96	0.5	0.08	111	0.158	4.68E-16	8.93E-15
XTE J1946+274	5.61	35.8	3.52	2.87	5.58	171.1	1.582	1.07E-15	2.47E-14
KS 1947+300	-2.63	0	3.03	0.5	1.32	40.415	0.040	4.72E-16	8.29E-15

Table 6.2 continued from the previous page

Name	TS	$\hat{n}_s$	$\hat{\Gamma}$	$\hat{\kappa}$	$\hat{\Phi}_0$	$\hat{P}$	$-\log_{10}(p_{\text{local}})$	U.L. $\Gamma = 2$	U.L. $\Gamma = 3$
X PER	-1.17	15.6	3.89	2.26	4.63	250.3	0.507	6.23E-16	1.14E-14
Cyg X-1	-2.63	0.04	1.25	0.5	0.39	5.5998	0.080	4.96E-16	7.89E-15
V2246 Cyg	-0.213	1.53	1.17	0.5	3.06	46.021	0.717	8.35E-16	1.32E-14
Cyg X-3	7.46	50.6	3.52	1.06	4.82	0.19966	1.345	1.38E-15	2.29E-14
GRO J2058+42	-2.63	0	3.88	0.5	0.65	55.03	0.102	5.14E-16	7.54E-15
LS V +44 17	-2.63	0	3.14	0.5	1.78	150	0.044	5.53E-16	7.75E-15
SAX J2103.5+4545	-2.46	3.99	2.55	0.5	1.7	12.665	0.281	5.27E-16	7.9E-15
BQ Cam	0.108	17.4	3.3	10.2	1.34	33.85	0.780	9.34E-16	1.46E-14
BD +53 2790	-0.275	16.3	4	1.98	1.02	9.5583	0.684	1.07E-15	1.28E-14
CI Cam	-2.63	0	3.99	0.5	4.99	19.41	0.049	7.18E-16	7.74E-15
V490 Cep	-0.477	1.45	1	1.33	5.31	20.848	0.495	8.97E-16	1.2E-14
gam Cas	-1.79	13.4	4	0.5	1.68	203.59	0.387	7.76E-16	9.11E-15
LS I +61 303	-2.63	0	3.54	0.5	2.18	26.496	0.064	7.12E-16	7.99E-15
SAX J2239.3+6116	3.09	23.5	4	12.1	0.6	265.62	1.055	1.22E-15	1.64E-14
BD +60 73	-2.36	6.89	4	0.5	5.8	15.66	0.294	7.13E-16	8.3E-15

Table 6.2 continued from the previous page

Name	TS	$\hat{n}_s$	$\hat{\Gamma}$	$\hat{\kappa}$	$\hat{\Phi}_0$	$\hat{P}$	$-\log_{10}(p_{\mathrm{local}})$	U.L. $\Gamma = 2$	U.L. $\Gamma = 3$
V635 Cas	9.07	50.5	4	0.83	2.58	24.316	2.284	2.67E-15	2.85E-14
V662 Cas	0.1	25.8	4	1.79	4.02	11.599	0.662	1.29E-15	1.42E-14
Swift J1753.5-0127	-2.63	0	2.61	0.5	2.74	0.13518	0.138	2.47E-16	9.95E-15
V616 Mon	0.523	27.5	3.71	1.26	4.7	0.32301	0.703	4.41E-16	1.89E-14
4U 1823-00	3.87	22.7	3.38	18.6	5.35	0.1333	0.799	4.33E-16	2.36E-14
Aql X-1	-2.53	2.04	2.48	0.5	4.6	0.7896	0.197	2.58E-16	9.9E-15
V1055 Ori	4.75	17.8	2.65	59.6	6.18	0.028403	1.006	6.94E-16	2.55E-14
GRS 1915+105	-0.865	23.4	3.77	0.5	2.78	33.862	0.516	5.22E-16	1.5E-14
V1408 Aql	-2.63	0	2.77	0.5	1.34	0.38888	0.043	3.35E-16	8.92E-15
M15 X-2	-2.37	8.24	3.8	0.5	6.27	0.015681	0.254	3.46E-16	1E-14
M15 X-1	-2.59	3.45	3.99	0.5	3.01	0.71303	0.195	3.02E-16	9.43E-15
V406 Vul	1.26	23.9	3.34	5.06	0.89	0.274	0.562	5.96E-16	1.46E-14
V934 Her	-2.63	1.21	3.98	0.5	1.24	420.17	0.144	3.99E-16	7.8E-15
QZ Vul	-2.63	0	2.64	0.5	5.01	0.34409	0.108	4.75E-16	8.38E-15
UW CrB	-1.39	17.8	4	0.5	5.92	0.077067	0.470	6.3E-16	1.22E-14

Table 6.2 continued from the previous page

Name	TS	$\hat{n}_s$	$\hat{\Gamma}$	$\hat{\kappa}$	$\hat{\Phi}_0$	$\hat{P}$	$-\log_{10}(p_{\mathrm{local}})$	U.L. $\Gamma = 2$	U.L. $\Gamma = 3$
V518 Per	-2.16	9.4	3.48	0.5	2.54	0.21216	0.319	5.52E-16	8.18E-15
4U 0042+32	2.56	17.5	4	21.1	4.12	11.588	0.664	7.72E-16	1.61E-14
V404 Cyg	-2.63	0	4	0.5	1.6	6.473	0.038	4.73E-16	7.89E-15
Her X-1	-0.718	20.1	4	0.5	2.08	1.7002	0.582	7.47E-16	1.21E-14
Cyg X-2	-0.0499	20.6	4	0.5	5.95	9.8445	0.703	9.01E-16	1.33E-14
V1727 Cyg	0.452	17.4	4	8.35	0.15	0.21826	0.793	9.07E-16	1.47E-14
KV UMa	-2.23	1.55	1.99	0.5	3	0.16993	0.292	5.76E-16	7.86E-15
V1037 Cas	-2.63	0	3.92	0.5	1.63	0.10236	0.122	7.35E-16	8.17E-15
Swift J061223.0+701243.9	-0.439	1.62	1.19	0.5	0.84	0.0125	0.493	1.34E-15	1.36E-14
HESS J0632+057	11.3	39.7	3.73	23.6	0.75	308.75	2.048	7.84E-16	3.85E-14
3FGL J0212.1+5320	1.04	19.8	3.01	0.5	3.38	0.86948	0.733	1.08E-15	1.46E-14

6.8 Discussion

This is the first time for V635 Cas, the most significant object in this analysis, to be studied for periodic emission, so there is no previous result to compare with. However, the second most significant source, HESS J0632+057, was the most significant source in the previous periodic point source analysis with a local p value of 8.7% [113]. The data used in that analysis were collected between April 2008 and May 2012. Since different data sets were used and the livetimes overlapped for only one year, the significance in the two analyses should be contributed by different events.

Although none of the XRBs shows a significant excess of neutrino events, the result can be used to compare with the neutrino emission prediction made by some phenomenological models. Here I will present two comparisons.

6.8.1 Cyg X-3

The neutrino flux from Cyg X-3 under a pp pion production scenario has been predicted in [136]. In the model of [136], neutrinos are produced via collisions between relativistic protons in the jet and cold protons in the stellar wind. The neutrino spectrum depends on the spectrum of the protons in the jet, which is assumed to take a generic form of a power law with cutoff at 100 TeV, i.e.,

$$N_p(E_p) \sim E_p^{-\alpha} \exp\left(\frac{E_p}{100\mathrm{TeV}}\right). \tag{6.16}$$

The spectral index α is unknown, so three values, 2.4, 2.5, and 2.7 were used in the calculation. The resultant neutrino spectrums of the three cases are shown as dashed lines in Figure 6.12. The 100 TeV cutoff in the proton spectrum is inherited by the neutrino spectrum, but the location is shifted to ~ 10 TeV. To test this model, the 90% upper limits for the three spectral indices are calculated with an injection spectrum largely the same as Equation 6.12, but with an exponential cutoff at 10 TeV. The range of upper limits for

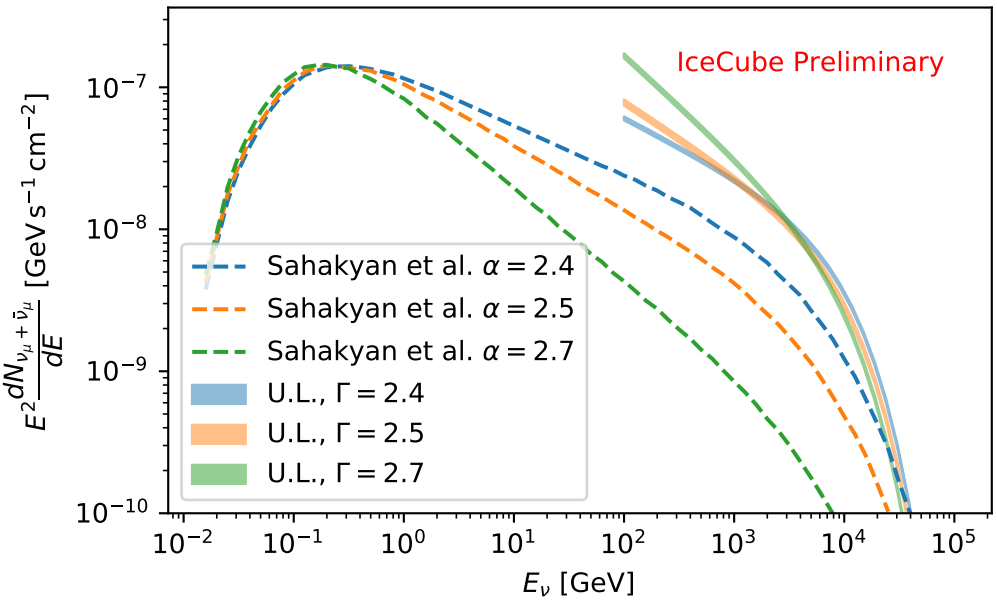

Figure 6.12: Neutrino spectra of Cyg X-3 predicted by [136] (dashed lines) and the upper limits calculated in this analysis (band) for three different spectral indices.

different κ are shown in Figure 6.12 as bands.

The model rejection factor, defined as the ratio of expected n_S from the upper limit flux to the expected n_s from the model flux, i.e.

$$MRF = \frac{n_{s,UL}}{n_{s,\text{model}}} \tag{6.17}$$

is calculated for each spectrum. If the model is inconsistent with the data, MRF will be less than 1. The values are 2.52 ($\Gamma = 2.4$), 5.54 ($\Gamma = 2.5$), and 26.68 ($\Gamma = 2.7$). Since the predicted spectra are below the upper limit, so this analysis is not able to rule out the possibility of this model being valid. For the case of $\alpha = 2.4$ and $\alpha = 2.5$, the spectra are close to the corresponding upper limits. Therefore, these models can be readily ruled out by IceCube Gen2, the next-generation neutrino detector which has an estimated 5-fold improvement in point source sensitivity [107]. However, the case of a $\alpha = 2.7$ proton spectrum is going to be difficult even for IceCube Gen2, at least for an analysis using the current method.

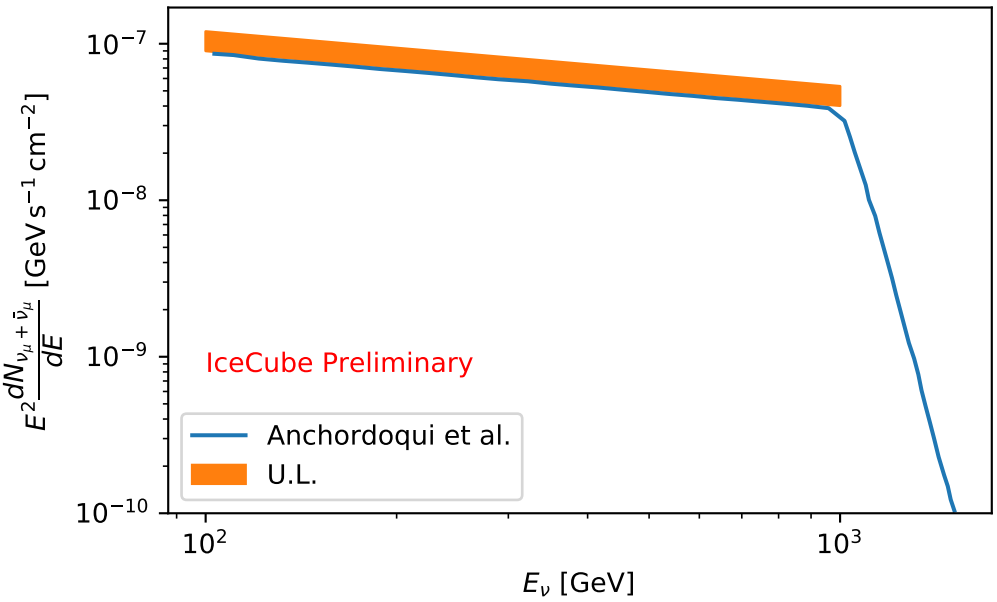

Figure 6.13: Neutrino spectrum of A 0535+26 predicted by [115] and the upper limit for a signal spectrum with $\Gamma = 2.35$. The maximum energy of the injected event is set to 1 TeV

6.8.2 A 0535+26

The model of A 0535+26 proposed in [115] is also tested against this analysis. The predicted neutrino spectrum has an index of $\Gamma = 2.35$ and a sharp cutoff at about 1 TeV. It is also predicted to vary within one period, with an on-time of about 50 days. The 90% upper limit for the source is calculated using a periodic injection with the same spectral index, and an upper energy bound for the injected events at 1 TeV. The spectrum and upper limit are shown in Figure 6.13 The neutrino spectrum prediction is comparable to the 90% upper limit. Given that the test statistic at A0535+26 is -2.63 and the best fit n_s is 0, the actual neutrino emission from this source should be smaller than the prediction. This shows that the model is in tension with the data, with a MRF of 1.05. The possibilities are (i) A 0535+26 is not a neutrino emitter, or (ii) neutrinos are produced at A 0535+026, but not via the accretion disk impact model described by [115].

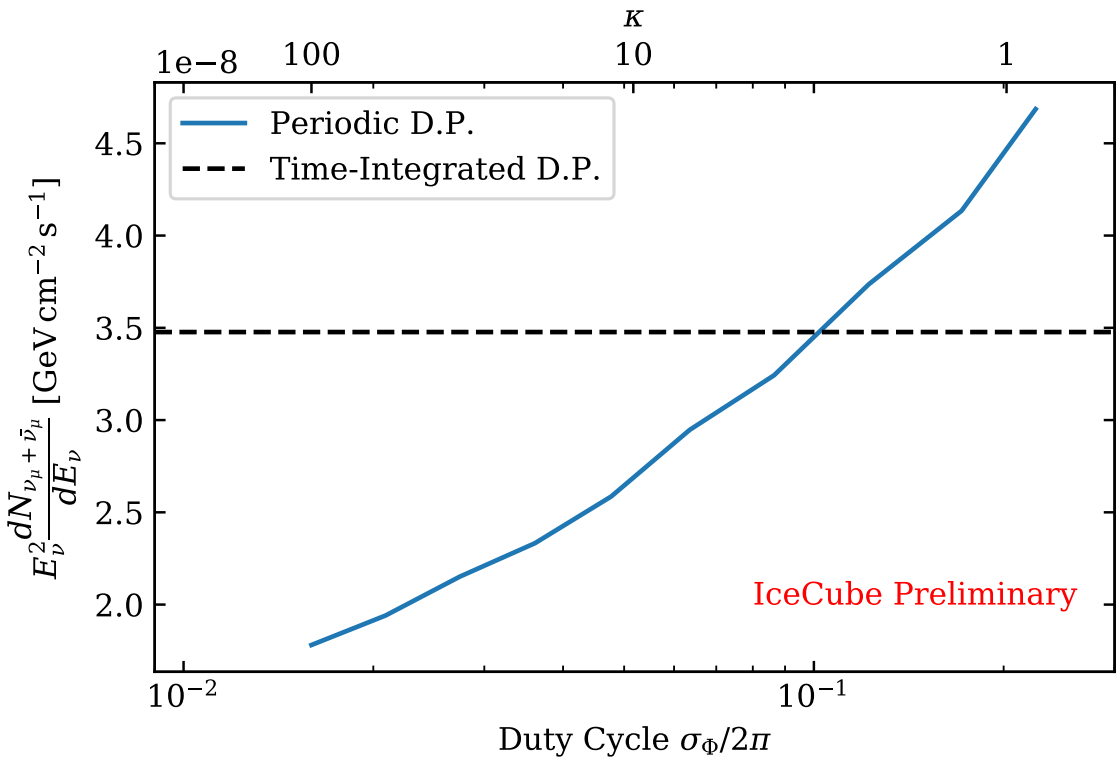

Figure 6.14: Discovery potentials of GRS 1915+105 as a function of duty cycles in a periodic (blue) and time-integrated (black dashed) analysis. The corresponding values of κ are plotted along the top x-axis for reference.

6.8.3 Comparison with Other Analysis

If XRBs emit neutrinos periodically, they can also be regarded as steady sources, and their neutrino emission can be searched in a time-integrated way. For a time-integrated search, the phase PDF in Equation 6.4 is replaced by 1, and the number of free parameters will be reduced to two, n_S and Γ. The regularization term and period prior are also removed from Equation 6.9. The discovery potential of GRS 1915+105 from a time-integrated analysis on the same data set is calculated to compare with the periodic analysis performed in this work, and the result is shown in Figure 6.14.

The time-integrated method has advantages over the periodic analysis in the large duty cycle regime, while the periodic analysis has a better discover potential in the small duty cycle regime. This comparison is intuitive, because as duty cycle approaches 1, the emis-

sion converges to a steady emission. In the large duty cycle regime, the analytical power gained from the the phase PDF is outweighed by the additional degrees of freedom from the free parameters in the phase PDF. This likely caused the worse performance of the periodic analysis in that regime.

There is also a possibility that neutrino emission is correlated to the X-ray outburst of XRBs, i.e., the neutrinos from XRBs are emitted in temporal coincidence with the X-ray outburst. This hypothesis has been adopted in the analysis performed by Qinrui Liu. In that analysis, a total of 102 XRBs over the entire sky are tested. X-ray lightcurves of these source are used as the signal temporal PDF in the likelihood function, and signal neutrinos events are expected to be found when the lightcurve is above a certain threshold, i.e., during the time of flare. These lightcurves are constructed by applying Bayesian Block algorithm [137] on measurements from SwiftBAT [138] and MAXI [139]. The result of this analysis will be reported in a future publication.

6.8.4 Future Works

There are some aspects in the current periodic point-source analysis that can be improved on. First, it might be worthwhile to consider the case of a double peak emission per cycle. Double peak profile is commonly observed in many periodically modulated emissions. It is also predicted in some neutrino emission models for XRBs. For example, according to [115], neutrino emission may happen in a short time before and after the periastron passage. [116] also predicted that the maximum neutrino energy as a function of the orbital phase should display a double peak behaviour. Using a single peak profile to model a double emission will lead to an overestimation of the duty cycle, and may lead to a loss of sensitivity. Therefore, there maybe possible gains in sensitivity if the signal phase PDF can describe a double peak profile.

The second aspect is to expand the search into the southern sky, or the downgoing region of IceCube. This is a challenging task because the event selection in the southern sky is

plagued by atmospheric muon events. However, a new event selection technique known as ESTES [140] is being developed within IceCube. It uses an enhanced veto method to select starting events, which can suppress atmospheric muons efficiently. This should improve the southern sky sensitivity quite significantly. Alternatively, the analysis can be carried out on a cascade data set in the southern sky. In the past, the point-source sensitivity with cascade events was poor due to their large uncertainty in the reconstructed directions. Recently, the deep neural network reconstruction for cascade events showed a large improvement over the conventional likelihood-based method in the high energy regime [106]. Since cascade samples usually have a higher signal purity than track samples, the improved direction of cascades should provide a southern sky sensitivity that is comparable to the northern sky. Either way, by extending the search to the southern sky, many interesting X-ray binaries, such as LS 5039, can be test for periodic emission.

Appendices

APPENDIX A

CATALOG OF X-RAY BINARIES

This catalog contains all X-ray binaries studied in chapter 6. Information including names, right ascensions, declinations, measured orbital period (P_{exp}), uncertainty of the measured orbital period (σ_P) are shown in the first six columns of the table. These XRBs are classified into two classes according to the type of their compact objects. If the compact object is a neutron star, the XRB will be labeled 'NS' in the 'Class' column. If the compact object is a black hole or black hole candidate, the XRB will be labeled 'BH' in that column. If the nature of the compact object is completely unknown, it will be labeled with '?'. The last column shows the references for the orbital periods.

Table A.1: Catalog of X-ray Binaries

Name	Alternate Name	RA (deg)	Dec (deg)	P_{exp} (day)	σ_P (day)	Class	Ref.
AX 1845.0-0433		281.2583	-4.55861	5.7195	7E-4	NS	[141]
IGR J18483-0311		282.075	-3.18333	18.545	0.02	NS	[142]
XTE J1855-026		283.8804	-2.60667	6.07415	8E-5	NS	[143]
2S 1845-024		282.075	-2.42	242.18	0.01	NS	[144]
4U 1901+03		285.9046	3.19194	22.5346	3E-4	NS	[145]
3A 1909+048	SS 433	287.9567	4.98278	13.068	0.004	BH	[146]
SAX J0635.2+0533		98.82621	5.55175	11.2	0.5	NS	[147]
4U 1909+07		287.7008	7.59786	4.4003	4E-4	NS	[148]
XTE J1859+083		284.775	8.25	60.65	0.08	NS	[149]
4U 1907+09		287.4138	9.82917	8.3753	1E-4	NS	[150]
IGR J19140+0951		288.5175	9.88286	13.552	0.003	NS	[151]
1A 0535+262	V725 Tau	84.7275	26.31583	111	0.5	NS	[152]
XTE J1946+274		296.4138	27.36539	172.05	1.15	NS	[153]
KS 1947+300		297.3771	30.20667	40.415	0.01	NS	[154]
4U 0352+309	X Per	58.84583	31.04972	250.3	0.6	NS	[155]

Table A.1 continued from the previous page

Name	Alternate Name	RA (deg)	Dec (deg)	P_{exp} (day)	σ_P (day)	Class	Ref.
4U 1956+35	Cyg X-1	299.5904	35.20167	5.599829	1.6E-5	BH	[156]
EXO 2030+375	V2246 Cyg	308.0633	37.6375	46.0208	0.0013	NS	[157]
4U 2030+40	Cyg X-3	308.1104	40.9525	0.199684	4.6E-5	BH	[158]
GRO J2058+42		314.6979	41.77694	55.03	0.06	NS	[159]
RX J0440.9+4431	LS V +44 17	70.24708	44.53028	150	0.2	NS	[160]
SAX J2103.5+4545		315.8988	45.75111	12.66536	8.8E-4	NS	[161]
V 0332+53	BQ Cam	53.74958	53.17333	33.85	0.003	NS	[162]
4U 2206+543	BD +53 2790	331.9842	54.51833	9.5584	0.0012	NS	[142]
XTE J0421+560	CI Cam	64.92583	55.99972	19.41	0.02	NS	[163]
1H 2138+579	V490 Cep	324.8775	56.98692	20.85	0.05	NS	[164]
2S 0053+604	gam Cas	14.17708	60.71667	203.59	0.21	NS	[165]
1E 0236.6+6100	LS I +61 303	40.13208	61.22944	26.496	0.0028	BH	[166]
SAX J2239.3+6116		339.8371	61.27411	262	5	NS	[167]
IGR J00370+6122	BD +60 73	9.29167	61.35972	15.66	0.01	NS	[168]
4U 0115+634	V635 Cas	19.63292	63.74	24.31	0.021	NS	[169]

Table A.1 continued from the previous page

Name	Alternate Name	RA (deg)	Dec (deg)	P_{exp} (day)	σ_P (day)	Class	Ref.
2S 0114+650	V662 Cas	19.51125	65.29167	11.599	0.005	NS	[151]
Swift J1753.5-0127		268.3679	-1.45173	0.135179	4.17E-05	BH	[170]
1A 0620-00	V616 Mon	95.68543	-0.34576	0.323014	4.17E-06	BH	[171]
4U 1823-00		276.3418	-0.01194	0.1333	5.56E-03	?	[172]
4U 1908+005	Aql X-1	287.8167	0.585	0.7896	1.00E-06	NS	[173]
4U 0614+091	V1055 Ori	94.28083	9.13711	0.028403	4.72E-03	NS	[174]
GRS 1915+105	V1487 Aql	288.7981	10.94577	33.85	1.60E-01	BH	[175]
4U 1957+11	V1408 Aql	299.8508	11.709	0.388879	5.00E-06	BH	[176]
CXO J212958.1+121002	M15 X-2	322.4919	12.16739	0.015681	1.39E-07	NS	[177]
4U 2129+12	M15 X-1	322.493	12.16747	0.713026	1.00E-06	NS	[151]
XTE J1859+226	V406 Vul	284.6733	22.65817	0.274	2.00E-03	BH	[178]
4U 1700+24	V934 Her	256.6438	23.97183	420.17	7.90E-01	NS	[179]
GS 2000+25	QZ Vul	300.7066	25.23647	0.344086	2.00E-06	BH	[180]
1E 1603.6+2600	UW CrB	241.4409	25.86253	0.0770672	2.00E-08	NS	[176]
GRO J0422+32	V518 Per	65.42829	32.90753	0.21216	2.00E-07	BH	[181]

Table A.1 continued from the previous page

Name	Alternate Name	RA (deg)	Dec (deg)	P_{exp} (day)	σ_P (day)	Class	Ref.
4U 0042+32		11.21	33.02139	11.6	0.7	?	[182]
GS 2023+338	V404 Cyg	306.0158	33.86756	6.473	1.00E-03	NS	[183]
2A 1655+353	Her X-1	254.4576	35.34239	1.700167	2.00E-09	NS	[184]
4U 2142+38	Cyg X-2	326.1717	38.32167	9.8445	1.90E-04	NS	[185]
4U 2129+47	V1727 Cyg	322.8592	47.29	0.218259	8.10E-08	NS	[186]
XTE J1118+480	KV UMa	169.5452	48.03692	0.169934	5.00E-07	BH	[187]
IGR J00291+5934	V1037 Cas	7.26275	59.57194	0.102362	2.31E-08	NS	[188]
Swift J061223.0+701243.9		93.09417	70.21206	0.0125	4.63E-05	?	[189]
HESS J0632+057	LS VI +05 11	98.2469	5.800323	317.3	4.3	NS	[190]
4FGL J0212.1+5321		33.0445	53.3507	0.869542	1.67E-04	NS	[191]

REFERENCES

[1] A. Dominguez, J. R. Primack, D. Rosario, F. Prada, R. Gilmore, S. Faber, D. Koo, R. Somerville, M. Pérez-Torres, P. Pérez-González, *et al.*, "Extragalactic background light inferred from aegis galaxy-sed-type fractions," *Monthly Notices of the Royal Astronomical Society*, vol. 410, no. 4, pp. 2556–2578, 2011.

[2] P. Carlson, "Discovery of cosmic rays," in *AIP Conference Proceedings*, American Institute of Physics, vol. 1516, 2013, pp. 9–16.

[3] P. D. Group, P. Zyla, R. Barnett, J. Beringer, O. Dahl, D. Dwyer, D. Groom, C.-J. Lin, K. Lugovsky, E. Pianori, *et al.*, "Review of particle physics," *Progress of theoretical and experimental physics*, vol. 2020, no. 8, p. 083C01, 2020.

[4] B. Peters, "Primary cosmic radiation and extensive air showers," *Il Nuovo Cimento (1955-1965)*, vol. 22, no. 4, pp. 800–819, 1961.

[5] K. Greisen, "End to the cosmic-ray spectrum?" *Physical Review Letters*, vol. 16, no. 17, p. 748, 1966.

[6] G. T. Zatsepin and V. A. Kuz'min, "Upper limit of the spectrum of cosmic rays," *JETPl*, vol. 4, p. 78, 1966.

[7] A. Aab, P. Abreu, M. Aglietta, I. Albuquerque, J. Albury, I. Allekotte, A. Almela, J. A. Castillo, J. Alvarez-Muñiz, G. Anastasi, *et al.*, "The pierre auger observatory: Contributions to the 36th international cosmic ray conference (icrc 2019)," *arXiv preprint arXiv:1909.09073*, 2019.

[8] D. Ivanov and D. Ivanov, "Energy spectrum measured by the telescope array experiment," in *Proceedings, 36th International Cosmic Ray Conference, July 24th-August 1st*, 2019.

[9] A. Aab, P. Abreu, M. Aglietta, I. Al Samarai, I. Albuquerque, I. Allekotte, A. Almela, J. A. Castillo, J. Alvarez-Muñiz, G. A. Anastasi, *et al.*, "Observation of a large-scale anisotropy in the arrival directions of cosmic rays above $8\times$ 1018 ev," *Science*, vol. 357, no. 6357, pp. 1266–1270, 2017.

[10] P. Erdoğdu, J. P. Huchra, O. Lahav, M. Colless, R. M. Cutri, E. Falco, T. George, T. Jarrett, D. H. Jones, C. S. Kochanek, *et al.*, "The dipole anisotropy of the 2 micron all-sky redshift survey," *Monthly Notices of the Royal Astronomical Society*, vol. 368, no. 4, pp. 1515–1526, 2006.

[11] M. Aartsen, M. Ackermann, J. Adams, J. A. Aguilar, M. Ahlers, M. Ahrens, D. Altmann, K. Andeen, T. Anderson, I. Ansseau, *et al.*, "Astrophysical neutrinos and

cosmic rays observed by icecube," *Advances in Space Research*, vol. 62, no. 10, pp. 2902–2930, 2018.

[12] E. Fermi, "On the origin of the cosmic radiation," *Physical review*, vol. 75, no. 8, p. 1169, 1949.

[13] M. Bustamante, P. Jez, J. Monroy Montañez, G. Carrillo Montoya, G. Romeo, F. Padilla Cabal, J. Duarte Chavez, U. Saldaña-Salazar, M. Pino Rozas, M. Velasquez, *et al.*, "High-energy cosmic-ray acceleration," 2010.

[14] T. K. Gaisser, R. Engel, and E. Resconi, *Cosmic rays and particle physics*. Cambridge University Press, 2016.

[15] C. Adler, Z. Ahammed, C. Allgower, J. Amonett, B. Anderson, M. Anderson, G. Averichev, J. Balewski, O. Barannikova, L. Barnby, *et al.*, "Kaon production and kaon to pion ratio in au+ au collisions at snn= 130 gev," *Physics Letters B*, vol. 595, no. 1-4, pp. 143–150, 2004.

[16] T. Kashti and E. Waxman, "Astrophysical neutrinos: Flavor ratios depend on energy," *Physical review letters*, vol. 95, no. 18, p. 181 101, 2005.

[17] A. G. Rosso, C. Mascaretti, A. Palladino, and F. Vissani, "Introduction to neutrino astronomy," *The European Physical Journal Plus*, vol. 133, no. 7, pp. 1–18, 2018.

[18] E. Waxman and J. Bahcall, "High energy neutrinos from astrophysical sources: An upper bound," *Physical Review D*, vol. 59, no. 2, p. 023 002, 1998.

[19] J. Bahcall and E. Waxman, "High energy astrophysical neutrinos: The upper bound is robust," *Physical Review D*, vol. 64, no. 2, p. 023 002, 2001.

[20] T. K. Gaisser, "Atmospheric neutrinos," *arXiv preprint arXiv:1910.08851*, 2019.

[21] I. Collaboration *et al.*, "Evidence for high-energy extraterrestrial neutrinos at the icecube detector," *Science*, vol. 342, no. 6161, 2013.

[22] J. Stettner, "Measurement of the diffuse astrophysical muon-neutrino spectrum with ten years of IceCube data," in *Proceedings of 36th International Cosmic Ray Conference — PoS(ICRC2019)*, vol. 358, 2019, p. 1017.

[23] R. Abbasi, M. Ackermann, J. Adams, J. Aguilar, M. Ahlers, M. Ahrens, C. Alispach, A. Alves Jr, N. Amin, K. Andeen, *et al.*, "The icecube high-energy starting event sample: Description and flux characterization with 7.5 years of data," *arXiv preprint arXiv:2011.03545*, 2020.

[24] V. Stenger, "Track fitting for dumand-ii octagon array," *University of Hawai'i at Manoa*, 1990.

[25] M. Ahlers and F. Halzen, "Opening a new window onto the universe with icecube," *Progress in Particle and Nuclear Physics*, vol. 102, pp. 73–88, 2018.

[26] M. Aartsen, M. Ackermann, J. Adams, J. Aguilar, M. Ahlers, M. Ahrens, I. Al Samarai, D. Altmann, K. Andeen, T. Anderson, *et al.*, "Extending the search for muon neutrinos coincident with gamma-ray bursts in icecube data," *The Astrophysical Journal*, vol. 843, no. 2, p. 112, 2017.

[27] M. Aartsen, M. Ackermann, J. Adams, J. Aguilar, M. Ahlers, M. Ahrens, D. Altmann, K. Andeen, T. Anderson, I. Ansseau, *et al.*, "Search for steady point-like sources in the astrophysical muon neutrino flux with 8 years of icecube data," *The European Physical Journal C*, vol. 79, no. 3, pp. 1–19, 2019.

[28] M. Aartsen, M. Ackermann, J. Adams, J. Aguilar, M. Ahlers, M. Ahrens, C. Alispach, K. Andeen, T. Anderson, I. Ansseau, *et al.*, "Time-integrated neutrino source searches with 10 years of icecube data," *Physical review letters*, vol. 124, no. 5, p. 051 103, 2020.

[29] M. Aartsen, M. Ackermann, J. Adams, J. A. Aguilar, M. Ahlers, M. Ahrens, I. Al Samarai, *et al.*, "Multimessenger observations of a flaring blazar coincident with high-energy neutrino icecube-170922a," *Science*, vol. 361, no. 6398, 2018.

[30] I. Collaboration *et al.*, "Neutrino emission from the direction of the blazar txs 0506+ 056 prior to the icecube-170922a alert," *Science*, vol. 361, no. 6398, pp. 147–151, 2018.

[31] M. Dentler, Á. Hernández-Cabezudo, J. Kopp, P. Machado, M. Maltoni, I. Martinez-Soler, and T. Schwetz, "Updated global analysis of neutrino oscillations in the presence of ev-scale sterile neutrinos," *Journal of High Energy Physics*, vol. 2018, no. 8, p. 10, 2018.

[32] C.-S. Wu, E. Ambler, R. Hayward, D. Hoppes, and R. P. Hudson, "Experimental test of parity conservation in beta decay," *Physical review*, vol. 105, no. 4, p. 1413, 1957.

[33] M. Aker, K. Altenmüller, M. Arenz, M. Babutzka, J. Barrett, S. Bauer, M. Beck, A. Beglarian, J. Behrens, T. Bergmann, *et al.*, "Improved upper limit on the neutrino mass from a direct kinematic method by katrin," *Physical review letters*, vol. 123, no. 22, p. 221 802, 2019.

[34] J. N. Bahcall and R. Davis, "Solar neutrinos: A scientific puzzle," *Science*, vol. 191, no. 4224, pp. 264–267, 1976.

[35] Y. Fukuda, T. Hayakawa, E. Ichihara, K. Inoue, K. Ishihara, H. Ishino, Y. Itow, T. Kajita, J. Kameda, S. Kasuga, *et al.*, "Evidence for oscillation of atmospheric neutrinos," *Physical Review Letters*, vol. 81, no. 8, p. 1562, 1998.

[36] F. An, J. Bai, A. Balantekin, H. Band, D. Beavis, W. Beriguete, M. Bishai, S. Blyth, K. Boddy, R. Brown, *et al.*, "Observation of electron-antineutrino disappearance at daya bay," *Physical Review Letters*, vol. 108, no. 17, p. 171 803, 2012.

[37] K. Abe, J. Adam, H. Aihara, T. Akiri, C. Andreopoulos, S. Aoki, A. Ariga, T. Ariga, S. Assylbekov, D. Autiero, *et al.*, "Measurement of neutrino oscillation parameters from muon neutrino disappearance with an off-axis beam," *Physical review letters*, vol. 111, no. 21, p. 211 803, 2013.

[38] M. Aartsen, M. Ackermann, J. Adams, J. Aguilar, M. Ahlers, M. Ahrens, I. Al Samarai, D. Altmann, K. Andeen, T. Anderson, *et al.*, "Measurement of atmospheric neutrino oscillations at 6–56 gev with icecube deepcore," *Physical review letters*, vol. 120, no. 7, p. 071 801, 2018.

[39] Z. Maki, M. Nakagawa, and S. Sakata, "Remarks on the unified model of elementary particles," *Progress of Theoretical Physics*, vol. 28, no. 5, pp. 870–880, 1962.

[40] Y. Ashie, J. Hosaka, K. Ishihara, Y. Itow, J. Kameda, Y. Koshio, A. Minamino, C. Mitsuda, M. Miura, S. Moriyama, *et al.*, "Measurement of atmospheric neutrino oscillation parameters by super-kamiokande i," *Physical Review D*, vol. 71, no. 11, p. 112 005, 2005.

[41] L. Wolfenstein, "Neutrino oscillations in matter," *Physical Review D*, vol. 17, no. 9, p. 2369, 1978.

[42] S. Mikheev and A. Y. Smirnov, "Resonance amplification of oscillations in matter and spectroscopy of solar neutrinos," *Yadernaya Fizika*, vol. 42, no. 6, pp. 1441–1448, 1985.

[43] J. A. Formaggio and G. Zeller, "From ev to eev: Neutrino cross sections across energy scales," *Reviews of Modern Physics*, vol. 84, no. 3, p. 1307, 2012.

[44] J. M. Conrad, M. H. Shaevitz, and T. Bolton, "Precision measurements with high-energy neutrino beams," *Reviews of Modern Physics*, vol. 70, no. 4, p. 1341, 1998.

[45] R. Gandhi, C. Quigg, M. H. Reno, and I. Sarcevic, "Neutrino interactions at ultra-high energies," *Physical Review D*, vol. 58, no. 9, p. 093 009, 1998.

[46] H. Lai and W. Tung, "Charm production and parton distributions," *Zeitschrift für Physik C Particles and Fields*, vol. 74, no. 3, pp. 463–468, 1997.

[47] A. C. Vincent, C. A. Argüelles, and A. Kheirandish, "High-energy neutrino attenuation in the earth and its associated uncertainties," *Journal of Cosmology and Astroparticle Physics*, vol. 2017, no. 11, p. 012, 2017.

[48] R. Gandhi, C. Quigg, M. H. Reno, and I. Sarcevic, "Ultrahigh-energy neutrino interactions," *Astroparticle physics*, vol. 5, no. 2, pp. 81–110, 1996.

[49] M. Aartsen, M. Ackermann, J. Adams, J. Aguilar, M. Ahlers, M. Ahrens, I. Al Samarai, D. Altmann, K. Andeen, T. Anderson, *et al.*, "Measurements using the inelasticity distribution of multi-tev neutrino interactions in icecube," *Physical Review D*, vol. 99, no. 3, p. 032 004, 2019.

[50] J. G. Learned and K. Mannheim, "High-energy neutrino astrophysics," *Annual Review of Nuclear and Particle Science*, vol. 50, no. 1, pp. 679–749, 2000.

[51] S. L. Glashow, "Resonant scattering of antineutrinos," *Physical Review*, vol. 118, no. 1, p. 316, 1960.

[52] I. Collaboration *et al.*, "Detection of a particle shower at the glashow resonance with icecube," *Nature*, vol. 591, no. 7849, pp. 220–224, 2021.

[53] V. Barger, L. Fu, J. Learned, D. Marfatia, S. Pakvasa, and T. Weiler, "Glashow resonance as a window into cosmic neutrino sources," *Physical Review D*, vol. 90, no. 12, p. 121 301, 2014.

[54] W. Pauli, "Open letter to the group of radioactive people at the gauverein meeting in tübingen," *Letter, December*, 1930.

[55] J. Chadwick, "Possible existence of a neutron," *Nature*, vol. 129, no. 3252, pp. 312–312, 1932.

[56] F. L. Wilson, "Fermi's theory of beta decay," *American Journal of Physics*, vol. 36, no. 12, pp. 1150–1160, 1968.

[57] F. Reines and C. L. Cowan, "The neutrino," *Nature*, vol. 178, no. 4531, pp. 446–449, 1956.

[58] K. Eguchi, S. Enomoto, K. Furuno, J. Goldman, H. Hanada, H. Ikeda, K. Ikeda, K. Inoue, K. Ishihara, W. Itoh, *et al.*, "First results from kamland: Evidence for reactor antineutrino disappearance," *Physical Review Letters*, vol. 90, no. 2, p. 021 802, 2003.

[59] P. Čerenkov, "Visible radiation produced by electrons moving in a medium with velocities exceeding that of light," *Physical Review*, vol. 52, no. 4, p. 378, 1937.

[60] I. Frank and I. Tamm, "Coherent visible radiation of fast electrons passing through matter," in *Selected Papers*, Springer, 1991, pp. 29–35.

[61] C. Spiering, "History of high-energy neutrino astronomy," *arXiv preprint arXiv:1903.11481*, 2019.

[62] V. Berezinskii and G. Zatsepin, "Possibilities of experiments with high-energy cosmic neutrinos: Project dumand (deep underwater muon neutrino detection).," *UsFiN*, vol. 122, pp. 3–36, 1977.

[63] E. Andrés, P. Askebjer, S. Barwick, R. Bay, L. Bergström, A. Biron, J. Booth, O. Botner, A. Bouchta, S. Carius, *et al.*, "The amanda neutrino telescope," *Nuclear Physics B-Proceedings Supplements*, vol. 77, no. 1-3, pp. 474–485, 1999.

[64] M. Ageron, J. Aguilar, I. Al Samarai, A. Albert, F. Ameli, M. André, M. Anghinolfi, G. Anton, S. Anvar, M. Ardid, *et al.*, "Antares: The first undersea neutrino telescope," *Nuclear Instruments and Methods in Physics Research Section A: Accelerators, Spectrometers, Detectors and Associated Equipment*, vol. 656, no. 1, pp. 11–38, 2011.

[65] A. Avrorin, V. Aynutdinov, V. Balkanov, I. Belolaptikov, S. Berezhnev, D. Bogorodsky, N. Budnev, I. Danilchenko, G. Domogatsky, A. Doroshenko, *et al.*, "The baikal neutrino experiment," *Nuclear Instruments and Methods in Physics Research Section A: Accelerators, Spectrometers, Detectors and Associated Equipment*, vol. 626, S13–S18, 2011.

[66] F. Halzen, "The case for a kilometer-scale high energy neutrino detector," *Nuclear Physics B-Proceedings Supplements*, vol. 38, no. 1-3, pp. 472–483, 1995.

[67] D. Tosi and H. Pandya, "IceTop as veto for IceCube: results," *PoS*, vol. ICRC2019, p. 445, 2019.

[68] D. Chirkin and W. Rhode, "Propagating leptons through matter with muon monte carlo (mmc)," *arXiv preprint hep-ph/0407075*, 2004.

[69] D. E. Groom, N. V. Mokhov, and S. I. Striganov, "Muon stopping power and range tables 10 mev–100 tev," *Atomic Data and Nuclear Data Tables*, vol. 78, no. 2, pp. 183–356, 2001.

[70] J. G. Learned and S. Pakvasa, "Detecting $\nu\tau$ oscillations at pev energies," *Astroparticle Physics*, vol. 3, no. 3, pp. 267–274, 1995.

[71] M. G. Aartsen, M. Ackermann, J. Adams, J. Aguilar, M. Ahlers, M. Ahrens, D. Altmann, K. Andeen, T. Anderson, I. Ansseau, *et al.*, "The icecube neutrino obser-

vatory: Instrumentation and online systems," *Journal of Instrumentation*, vol. 12, no. 03, P03012, 2017.

[72] D. Pandel, "Bestimmung von wasser-und detektorparametern und rekonstruktion von myonen bis 100 tev mit dem baikal-neutrinoteleskop nt-72," *Humboldt-Universitaet Berlin*, 1996.

[73] I. Collaboration *et al.*, "South pole glacial climate reconstruction from multi-borehole laser particulate stratigraphy," *Journal of glaciology*, vol. 59, no. 218, pp. 1117–1128, 2013.

[74] D. Chirkin, I. Collaboration, *et al.*, "Evidence of optical anisotropy of the south pole ice," in *Proceedings, 33rd International Cosmic Ray Conference (ICRC2013): Rio de Janeiro, Brazil*, 2013, p. 0580.

[75] D. Chirkin and M. Rongen, "Light diffusion in birefringent polycrystals and the IceCube ice anisotropy," *PoS*, vol. ICRC2019, p. 854, 2019.

[76] M. Aartsen, R. Abbasi, Y. Abdou, M. Ackermann, J. Adams, J. Aguilar, M. Ahlers, D. Altmann, J. Auffenberg, X. Bai, *et al.*, "Measurement of south pole ice transparency with the icecube led calibration system," *Nuclear Instruments and Methods in Physics Research Section A: Accelerators, Spectrometers, Detectors and Associated Equipment*, vol. 711, pp. 73–89, 2013.

[77] T. Neunhöffer, "Estimating the angular resolution of tracks in neutrino telescopes based on a likelihood analysis," *Astroparticle Physics*, vol. 25, no. 3, pp. 220–225, 2006.

[78] M. G. Aartsen, R. Abbasi, M. Ackermann, J. Adams, J. Aguilar, M. Ahlers, D. Altmann, C. Arguelles, J. Auffenberg, X. Bai, *et al.*, "Energy reconstruction methods in the icecube neutrino telescope," *Journal of Instrumentation*, vol. 9, no. 03, P03009, 2014.

[79] M. Kowalski, "Status of high-energy neutrino astronomy," in *Journal of Physics: Conference Series*, IOP Publishing, vol. 632, 2015, p. 012 039.

[80] K. Murase and E. Waxman, "Constraining high-energy cosmic neutrino sources: Implications and prospects," *Physical Review D*, vol. 94, no. 10, p. 103 006, 2016.

[81] M. Ahlers and F. Halzen, "Pinpointing extragalactic neutrino sources in light of recent icecube observations," *Physical Review D*, vol. 90, no. 4, p. 043 005, 2014.

[82] C. Tung, I. Taboada, T. Glauch, M. Larson, A. Pizzuto, and R. R., "Firesong: A python package to simulate populations of extragalactic neutrino sources," In preparation - to be submitted to JOSS.

[83] M. Aartsen, M. Ackermann, J. Adams, J. Aguilar, M. Ahlers, M. Ahrens, C. Alispach, K. Andeen, T. Anderson, I. Ansseau, *et al.*, "A search for neutrino point-source populations in 7 yr of icecube data with neutrino-count statistics," *The Astrophysical Journal*, vol. 893, no. 2, p. 102, 2020.

[84] H. A. Solares, S. Coutu, J. DeLaunay, D. Fox, T. Grégoire, A. Keivani, F. Krauß, M. Mostafá, K. Murase, C. Turley, *et al.*, "Multimessenger gamma-ray and neutrino coincidence alerts using hawc and icecube subthreshold data," *The Astrophysical Journal*, vol. 906, no. 1, p. 63, 2021.

[85] K. Satalecka, A. Brown, A. Rosales de león, O. Sergijenko, C. F. Tung, R. Reimann, T. Glauch, and I. Taboada, "Neutrino Target of Opportunity program of the Cherenkov Telescope Array," *PoS*, vol. ICRC2019, p. 784, 2019.

[86] P. A. Ade, N. Aghanim, M. Arnaud, M. Ashdown, J. Aumont, C. Baccigalupi, A. Banday, R. Barreiro, J. Bartlett, N. Bartolo, *et al.*, "Planck 2015 results-xiii. cosmological parameters," *Astronomy & Astrophysics*, vol. 594, A13, 2016.

[87] P. Oesch, G. Brammer, P. Van Dokkum, G. Illingworth, R. Bouwens, I. Labbé, M. Franx, I. Momcheva, M. Ashby, G. Fazio, *et al.*, "A remarkably luminous galaxy at z= 11.1 measured with hubble space telescope grism spectroscopy," *The Astrophysical Journal*, vol. 819, no. 2, p. 129, 2016.

[88] P. Madau and M. Dickinson, "Cosmic star-formation history," *Annual Review of Astronomy and Astrophysics*, vol. 52, pp. 415–486, 2014.

[89] A. M. Hopkins and J. F. Beacom, "On the normalization of the cosmic star formation history," *The Astrophysical Journal*, vol. 651, no. 1, p. 142, 2006.

[90] K. Satalecka, A. Brown, A. Rosales de león, O. Sergijenko, C. F. Tung, R. Reimann, T. Glauch, and I. Taboada, "The sensitivity of the cherenkov telescope array to the gamma-ray emission from study of neutrino events," In preparation - to be submitted to MNRAS.

[91] F. Halzen, A. Kheirandish, T. Weisgarber, and S. P. Wakely, "On the neutrino flares from the direction of txs 0506+ 056," *The Astrophysical Journal Letters*, vol. 874, no. 1, p. L9, 2019.

[92] D. Fiorillo, K. Satalecka, I. Taboada, and C. F. Tung, In preparation.

[93] B. P. Abbott, R. Abbott, T. Abbott, M. Abernathy, F. Acernese, K. Ackley, C. Adams, T. Adams, P. Addesso, R. Adhikari, *et al.*, "Observation of gravitational waves from a binary black hole merger," *Physical review letters*, vol. 116, no. 6, p. 061 102, 2016.

[94] M. Aartsen, M. Ackermann, J. Adams, J. Aguilar, M. Ahlers, M. Ahrens, D. Altmann, K. Andeen, T. Anderson, I. Ansseau, *et al.*, "The icecube realtime alert system," *Astroparticle Physics*, vol. 92, pp. 30–41, 2017.

[95] Y. T. Tanaka, S. Buson, and D. Kocevski, "Fermi-LAT detection of increased gamma-ray activity of TXS 0506+056, located inside the IceCube-170922A error region.," *The Astronomer's Telegram*, vol. 10791, p. 1, Sep. 2017.

[96] F. Lucarelli, G. Piano, C. Pittori, F. Verrecchia, M. Tavani, A. Bulgarelli, P. Munar-Adrover, G. Minervini, A. Ursi, S. Vercellone, *et al.*, "Agile confirmation of gamma-ray activity from the icecube-170922a error region," *The Astronomer's Telegram*, vol. 10801, p. 1, 2017.

[97] M. de Naurois, H. Collaboration, *et al.*, "Hess follow-up of icecube-170922a," *The Astronomer's Telegram*, vol. 10787, p. 1, 2017.

[98] R. Mukherjee, "Veritas follow-up observations of icecube neutrino event 170922a," *The Astronomer's Telegram*, vol. 10833, p. 1, 2017.

[99] R. Mirzoyan, A. Babić, D. Dominis Prester, N. Godinović, D. Hrupec, D. Lelas, I. Puljak, T. Surić, I. Šnidarić, T. Terzić, *et al.*, "First-time detection of vhe gamma rays by magic from a direction consistent with the recent ehe neutrino event icecube-170922a," *The Astronomer's Telegram,# 10817*, 2017.

[100] F. Acero, M. Ackermann, M. Ajello, A. Albert, W. Atwood, M. Axelsson, L. Baldini, J. Ballet, G. Barbiellini, D. Bastieri, *et al.*, "Fermi large area telescope third source catalog," *The Astrophysical Journal Supplement Series*, vol. 218, no. 2, p. 23, 2015.

[101] M. Ajello, W. Atwood, L. Baldini, J. Ballet, G. Barbiellini, D. Bastieri, R. Bellazzini, E. Bissaldi, R. Blandford, E. Bloom, *et al.*, "3fhl: The third catalog of hard fermi-lat sources," *The Astrophysical Journal Supplement Series*, vol. 232, no. 2, p. 18, 2017.

[102] R. Buehler, "The second catalog of flaring gamma-ray sources (2fav): Observing astrophysical accelerators in real time," in *Proceedings of the 7th International Fermi Symposium*, 2017, p. 123.

[103] C. Kopper, "Observation of Astrophysical Neutrinos in Six Years of IceCube Data," *PoS*, vol. ICRC2017, p. 981, 2017.

[104] M. Honda, T. Kajita, K. Kasahara, S. Midorikawa, and T. Sanuki, "Calculation of atmospheric neutrino flux using the interaction model calibrated with atmospheric muon data," *Physical Review D*, vol. 75, no. 4, p. 043 006, 2007.

[105] C. Haack and C. Wiebusch, "A measurement of the diffuse astrophysical muon neutrino flux using eight years of IceCube data.," in *Proceedings of 35th International Cosmic Ray Conference — PoS(ICRC2017)*, vol. 301, 2017, p. 1005.

[106] R. Abbasi, M. Ackermann, J. Adams, J. Aguilar, M. Ahlers, M. Ahrens, C. Alispach, A. Alves Jr, N. Amin, R. An, *et al.*, "A convolutional neural network based cascade reconstruction for the icecube neutrino observatory," *arXiv preprint arXiv:2101.11589*, 2021.

[107] M. Aartsen, R. Abbasi, M. Ackermann, J. Adams, J. Aguilar, M. Ahlers, M. Ahrens, C. Alispach, P. Allison, N. Amin, *et al.*, "Icecube-gen2: The window to the extreme universe," *arXiv preprint arXiv:2008.04323*, 2020.

[108] P. Podsiadlowski, S. Rappaport, and E. Pfahl, "Evolutionary sequences for low- and intermediate-mass x-ray binaries," *The Astrophysical Journal*, vol. 565, no. 2, p. 1107, 2002.

[109] T. M. Belloni, "States and transitions in black hole binaries," in *The Jet Paradigm*, Springer, 2010, pp. 53–84.

[110] J. Albert, E. Aliu, H. Anderhub, P. Antoranz, A. Armada, C. Baixeras, J. Barrio, H. Bartko, D. Bastieri, J. Becker, *et al.*, "Very high energy gamma-ray radiation from the stellar mass black hole binary cygnus x-1," *The Astrophysical Journal Letters*, vol. 665, no. 1, p. L51, 2007.

[111] A. Abeysekara, A. Albert, R. Alfaro, C. Alvarez, J. Álvarez, R. Arceo, J. Arteaga-Velázquez, D. A. Rojas, H. A. Solares, E. Belmont-Moreno, *et al.*, "Very-high-energy particle acceleration powered by the jets of the microquasar ss 433," *Nature*, vol. 562, no. 7725, pp. 82–85, 2018.

[112] R. Abbasi, Y. Abdou, T. Abu-Zayyad, M. Ackermann, J. Adams, J. Aguilar, M. Ahlers, M. Allen, D. Altmann, K. Andeen, *et al.*, "Searches for periodic neutrino emission from binary systems with 22 and 40 strings of icecube," *The Astrophysical Journal*, vol. 748, no. 2, p. 118, 2012.

[113] M. Aartsen, M. Ackermann, J. Adams, J. Aguilar, M. Ahlers, M. Ahrens, D. Altmann, T. Anderson, M. Archinger, C. Arguelles, *et al.*, "Searches for time-dependent neutrino sources with icecube data from 2008 to 2012," *The Astrophysical Journal*, vol. 807, no. 1, p. 46, 2015.

[114] A. Albert, M. André, G. Anton, M. Ardid, J.-J. Aubert, T. Avgitas, B. Baret, J. Barrios-Martı, S. Basa, V. Bertin, *et al.*, "Time-dependent search for neutrino emission from x-ray binaries with the antares telescope," *Journal of Cosmology and Astroparticle Physics*, vol. 2017, no. 04, p. 019, 2017.

[115] L. A. Anchordoqui, D. F. Torres, T. P. McCauley, G. E. Romero, and F. A. Aharonian, "Neutrinos from accreting neutron stars," *The Astrophysical Journal*, vol. 589, no. 1, p. 481, 2003.

[116] H. R. Christiansen, M. Orellana, and G. E. Romero, "High-energy neutrino emission from x-ray binaries," *Physical Review D*, vol. 73, no. 6, p. 063 012, 2006.

[117] W. Bednarek, "Tev neutrinos from microquasars in compact massive binaries," *The Astrophysical Journal*, vol. 631, no. 1, p. 466, 2005.

[118] T. Gaisser, F. Stecker, A. Harding, and J. Barnard, "Effects of high-energy neutrino production and interactions on stars in close x-ray binaries," *The Astrophysical Journal*, vol. 309, pp. 674–681, 1986.

[119] A. Neronov and M. Ribordy, "Neutrino signal from γ-ray-loud binaries powered by high energy protons," *Physical Review D*, vol. 79, no. 4, p. 043 013, 2009.

[120] A. Levinson and E. Waxman, "Probing microquasars with tev neutrinos," *Physical Review Letters*, vol. 87, no. 17, p. 171 101, 2001.

[121] C. Distefano, D. Guetta, E. Waxman, and A. Levinson, "Neutrino flux predictions for known galactic microquasars," *The Astrophysical Journal*, vol. 575, no. 1, p. 378, 2002.

[122] T. Kintscher, "Rapid response to extraordinary events: Transient neutrino sources with the icecube experiment," Ph.D. dissertation, Humboldt-Universität zu Berlin, Mathematisch-Naturwissenschaftliche Fakultät, 2020.

[123] Markus Voge, "Searches for neutrinos from supernovae using cherenkov in-ice detectors," Ph.D. dissertation, Rheinische Friedrich-Wilhelms-Universität Bonn, May 2017.

[124] T. K. Gaisser, "Spectrum of cosmic-ray nucleons, kaon production, and the atmospheric muon charge ratio," *Astroparticle Physics*, vol. 35, no. 12, pp. 801–806, 2012.

[125] Q. Liu, J. Van Paradijs, and E. Van Den Heuvel, "Catalogue of high-mass x-ray binaries in the galaxy," *Astronomy & Astrophysics*, vol. 455, no. 3, pp. 1165–1168, 2006.

[126] ——, "A catalogue of low-mass x-ray binaries in the galaxy, lmc, and smc," *Astronomy & Astrophysics*, vol. 469, no. 2, pp. 807–810, 2007.

[127] S. P. Wakely and D. Horan, "Tevcat: An online catalog for very high energy gamma-ray astronomy," in *ICRC*, vol. 3, 2008, pp. 1341–1344.

[128] S. Abdollahi, F. Acero, M. Ackermann, M. Ajello, W. Atwood, M. Axelsson, L. Baldini, J. Ballet, G. Barbiellini, D. Bastieri, *et al.*, "Fermi large area telescope fourth source catalog," *The Astrophysical Journal Supplement Series*, vol. 247, no. 1, p. 33, 2020.

[129] P. Heix, T. I. C. (c. l. see PoS(ICRC2019) 1177), S. Tilav, C. Wiebusch, and M. Zöcklein, "Seasonal Variation of Atmospheric Neutrinos in IceCube," *PoS*, vol. ICRC2019, p. 465, 2019.

[130] S. Tilav, T. Gaisser, D. Soldin, and P. Desiati, "Seasonal Variation of Atmospheric Muons in IceCube," *PoS*, vol. ICRC2019, p. 894, 2019.

[131] R. Abbasi, Y. Abdou, T. Abu-Zayyad, J. Adams, J. Aguilar, M. Ahlers, K. Andeen, J. Auffenberg, X. Bai, M. Baker, *et al.*, "Time-dependent searches for point sources of neutrinos with the 40-string and 22-string configurations of icecube," *The Astrophysical Journal*, vol. 744, no. 1, p. 1, 2011.

[132] J. Braun, M. Baker, J. Dumm, C. Finley, A. Karle, and T. Montaruli, "Time-dependent point source search methods in high energy neutrino astronomy," *Astroparticle Physics*, vol. 33, no. 3, pp. 175–181, 2010.

[133] H. Dembinski, P. Ongmongkolkul, C. Deil, D. Hurtado, M. Feickert, H. Schreiner, C. B. Andrew, F. Rost, A. Pearce, L. Geiger, *et al.*, *Scikit-hep/iminuit: V1. 4.9*, 2020.

[134] F. James and M. Roos, "Minuit: A system for function minimization and analysis of the parameter errors and corrections," *Comput. Phys. Commun.*, vol. 10, no. CERN-DD-75-20, pp. 343–367, 1975.

[135] S. S. Wilks, "The large-sample distribution of the likelihood ratio for testing composite hypotheses," *The annals of mathematical statistics*, vol. 9, no. 1, pp. 60–62, 1938.

[136] N. Sahakyan, G. Piano, and M. Tavani, "Hadronic gamma-ray and neutrino emission from cygnus x-3," *The Astrophysical Journal*, vol. 780, no. 1, p. 29, 2013.

[137] J. D. Scargle, "Studies in astronomical time series analysis. v. bayesian blocks, a new method to analyze structure in photon counting data," *The Astrophysical Journal*, vol. 504, no. 1, p. 405, 1998.

[138] H. A. Krimm, S. T. Holland, R. H. Corbet, A. B. Pearlman, P. Romano, J. A. Kennea, J. S. Bloom, S. D. Barthelmy, W. H. Baumgartner, J. R. Cummings, *et al.*, "The swift/bat hard x-ray transient monitor," *The Astrophysical Journal Supplement Series*, vol. 209, no. 1, p. 14, 2013.

[139] M. Matsuoka, K. Kawasaki, S. Ueno, H. Tomida, M. Kohama, M. Suzuki, Y. Adachi, M. Ishikawa, T. Mihara, M. Sugizaki, *et al.*, "The maxi mission on the iss: Science and instruments for monitoring all-sky x-ray images," *Publications of the Astronomical Society of Japan*, vol. 61, no. 5, pp. 999–1010, 2009.

[140] M. Silva and S. Mancina, "Measurement of the Diffuse Muon Neutrino Flux using Starting Track Events in IceCube," *PoS*, vol. ICRC2019, p. 1010, 2019.

[141] M. E. Goossens, A. J. Bird, S. P. Drave, A. Bazzano, A. B. Hill, V. A. McBride, V. Sguera, and L. Sidoli, "Discovering a 5.72-d period in the supergiant fast x-ray transient AX j1845.0-0433," *Monthly Notices of the Royal Astronomical Society*, vol. 434, no. 3, pp. 2182–2187, Jul. 2013.

[142] A. M. Levine, H. V. Bradt, D. Chakrabarty, R. H. D. Corbet, and R. J. Harris, "AN EXTENDED AND MORE SENSITIVE SEARCH FOR PERIODICITIES IN ROSSI x-RAY TIMING EXPLORER /ALL-SKY MONITOR x-RAY LIGHT CURVES," *ApJS*, vol. 196, no. 1, p. 6, Aug. 2011.

[143] M. Falanga, E. Bozzo, A. Lutovinov, J. M. Bonnet-Bidaud, Y. Fetisova, and J. Puls, "Ephemeris, orbital decay, and masses of ten eclipsing high-mass x-ray binaries," *Astronomy & Astrophysics*, vol. 577, A130, May 2015.

[144] M. H. Finger, L. Bildsten, D. Chakrabarty, T. A. Prince, D. M. Scott, C. A. Wilson, R. B. Wilson, and S. N. Zhang, "The outbursts and orbit of the accreting pulsar GS 1843-02 = 2s 1845-024," *ApJ*, vol. 517, no. 1, pp. 449–459, May 1999.

[145] Y. Tuo, L. Ji, S. Tsygankov, T. Mihara, L. Song, M. Ge, A. Nabizadeh, L. Tao, J. Qu, Y. Zhang, *et al.*, "Insight-hxmt insight into switch of the accretion mode: The case of the x-ray pulsar 4u 1901+ 03," *Journal of High Energy Astrophysics*, vol. 27, pp. 38–43, 2020.

[146] K. Rasul, P. M. Chadwick, J. A. Graham, and A. M. Brown, "Gamma-rays from SS433: Evidence for periodicity," *Monthly Notices of the Royal Astronomical Society*, vol. 485, no. 2, pp. 2970–2975, Feb. 2019.

[147] P. Kaaret, G. Cusumano, and B. Sacco, "X-ray timing of the 34 millisecond binary pulsar SAX j0635+0533," *The Astrophysical Journal*, vol. 542, no. 1, pp. L41–L43, Oct. 2000.

[148] R. H. D. Corbet and H. A. Krimm, "SUPERORBITAL PERIODIC MODULATION IN WIND-ACCRETION HIGH-MASS x-RAY BINARIES FROMSWIFT-BURST ALERT TELESCOPE OBSERVATIONS," *ApJ*, vol. 778, no. 1, p. 45, Nov. 2013.

[149] R. H. D. Corbet, J. J. M. in't Zand, A. M. Levine, and F. E. Marshall, "ROSSI x-RAY TIMING EXPLORERANDBeppoSAXOBSERVATIONS OF THE TRANSIENT x-RAY PULSAR XTE j1859+083," *ApJ*, vol. 695, no. 1, pp. 30–35, Mar. 2009.

[150] J. J. M. in't Zand, A. Baykal, and T. E. Strohmayer, "Recent x-ray measurements of the accretion-powered pulsar 4u 1907+09," *ApJ*, vol. 496, no. 1, pp. 386–394, Mar. 1998.

[151] L. Wen, A. M. Levine, R. H. D. Corbet, and H. V. Bradt, "A systematic search for periodicities in RXTE ASM data," *ASTROPHYS J SUPPL S*, vol. 163, no. 2, pp. 372–392, Apr. 2006.

[152] M. J. Coe, P. Reig, V. A. McBride, J. L. Galache, and J. Fabregat, "A 0535+26: Back in business," *Monthly Notices of the Royal Astronomical Society*, vol. 368, no. 1, pp. 447–453, May 2006.

[153] D. M. Marcu-Cheatham, K. Pottschmidt, M. Kühnel, S. Müller, S. Falkner, I. Caballero, M. H. Finger, P. J. Jenke, C. A. Wilson-Hodge, F. Fürst, V. Grinberg, P. B. Hemphill, I. Kreykenbohm, D. Klochkov, R. E. Rothschild, Y. Terada, T. Enoto, W. Iwakiri, M. T. Wolff, P. A. Becker, K. S. Wood, and J. Wilms, "THE TRANSIENT ACCRETING x-RAY PULSAR XTE j1946+274: STABILITY OF x-RAY PROPERTIES AT LOW FLUX AND UPDATED ORBITAL SOLUTION," *ApJ*, vol. 815, no. 1, p. 44, Dec. 2015.

[154] D. K. Galloway, E. H. Morgan, and A. M. Levine, "A frequency glitch in an accreting pulsar," *ApJ*, vol. 613, no. 2, pp. 1164–1172, Oct. 2004.

[155] H. Delgado-Marti, A. M. Levine, E. Pfahl, and S. A. Rappaport, "The orbit of x persei and its neutron star companion," *ApJ*, vol. 546, no. 1, pp. 455–468, Jan. 2001.

[156] C. Brocksopp, R. P. Fender, V. Larionov, V. M. Lyuty, A. E. Tarasov, G. G. Pooley, W. S. Paciesas, and P. Roche, "Orbital, precessional and flaring variability of cygnus x-1," *Monthly Notices of the Royal Astronomical Society*, vol. 309, no. 4, pp. 1063–1073, Nov. 1999.

[157] C. A. Wilson, M. H. Finger, and A. Camero-Arranz, "Outbursts large and small from EXO 2030+375," *ApJ*, vol. 678, no. 2, pp. 1263–1272, May 2008.

[158] F. L. Collaboration *et al.*, "Modulated high-energy gamma-ray emission from the microquasar cygnus x-3," *Science*, vol. 326, no. 5959, pp. 1512–1516, 2009. eprint: https://science.sciencemag.org/content/326/5959/1512.full.pdf.

[159] C. A. Wilson, "GRO j2058+42 observations with BATSE and RXTE," in *AIP Conference Proceedings*, AIP, 2000.

[160] C. Ferrigno, R. Farinelli, E. Bozzo, K. Pottschmidt, D. Klochkov, and P. Kretschmar, "RX j0440.9 + 4431: A persistent be/x-ray binary in outburst," *Astronomy & Astrophysics*, vol. 553, A103, May 2013.

[161] A. Baykal, S. C. Inam, M. J. Stark, C. M. Heffner, A. E. Erkoca, and J. H. Swank, "Timing studies on RXTE observations of SAX j2103.5+4545," *Monthly Notices of the Royal Astronomical Society*, vol. 374, no. 3, pp. 1108–1114, Jan. 2007.

[162] V. Doroshenko, S. Tsygankov, and A. Santangelo, "Orbital parameters of v 0332+53 from 2015 giant outburst data," *Astronomy & Astrophysics*, vol. 589, A72, Apr. 2016.

[163] E. Barsukova, N. Borisov, A. Burenkov, V. Klochkova, V. Goranskij, and N. Metlova, "The orbital period of the b [e]/x-ray binary ci cam/xte j0421+ 560," in *Stars with the B [e] Phenomenon*, vol. 355, 2006, p. 305.

[164] V. A. McBride, J. Wilms, I. Kreykenbohm, M. J. Coe, R. E. Rothschild, P. Kretschmar, K. Pottschmidt, J. Fisher, and T. Hamson, "On the cyclotron line in cepheus x-4," *Astronomy & Astrophysics*, vol. 470, no. 3, pp. 1065–1070, May 2007.

[165] M. A. Smith, R. L. de Oliveira, C. Motch, G. W. Henry, N. D. Richardson, K. S. Bjorkman, P. Stee, D. Mourard, J. D. Monnier, X. Che, *et al.*, "The relationship between γ cassiopeiae's x-ray emission and its circumstellar environment," *Astronomy & Astrophysics*, vol. 540, A53, 2012.

[166] P. C. Gregory, "Bayesian analysis of radio observations of the be x-ray binary LS i +61o303," *ApJ*, vol. 575, no. 1, pp. 427–434, Aug. 2002.

[167] P. Reig, P. Blay, and D. Blinov, "The optical counterpart to the be/x-ray binary SAX j2239.3+6116," *Astronomy & Astrophysics*, vol. 598, A16, Jan. 2017.

[168] A. González-Galán, I. Negueruela, N. Castro, S. Simón-Dıaz, J. Lorenzo, and F. Vilardell, "Astrophysical parameters and orbital solution of the peculiar x-ray transient IGR j00370+6122," *Astronomy & Astrophysics*, vol. 566, A131, Jun. 2014.

[169] P. A. Boldin, S. S. Tsygankov, and A. A. Lutovinov, "On timing and spectral characteristics of the x-ray pulsar 4u 0115+63: Evolution of the pulsation period and the cyclotron line energy," *Astron. Lett.*, vol. 39, no. 6, pp. 375–388, Jun. 2013.

[170] C. Zurita, M. Durant, M. A. P. Torres, T. Shahbaz, J. Casares, and D. Steeghs, "Swift j1753.5-0127: The black hole candidate with the shortest orbital period," *ApJ*, vol. 681, no. 2, pp. 1458–1463, Jul. 2008.

[171] J. E. McClintock and R. A. Remillard, "The black hole binary a0620-00," *ApJ*, vol. 308, p. 110, Sep. 1986.

[172] T. Shahbaz, C. A. Watson, and H. Hernandez-Peralta, "On the ultracompact nature of 4u 1822-000," *Monthly Notices of the Royal Astronomical Society*, vol. 376, no. 4, pp. 1886–1888, Mar. 2007.

[173] D. M. Sánchez, T. Muñoz-Darias, J. Casares, and F. Jiménez-Ibarra, "The donor of aquila x-1 revealed by high-angular resolution near-infrared spectroscopy," *Mon. Not. R. Astron. Soc: Lett.*, vol. 464, no. 1, pp. L41–L45, Sep. 2016.

[174] M. C. Baglio, D. Mainetti, P. D'Avanzo, S. Campana, S. Covino, D. M. Russell, and T. Shahbaz, "Polarimetric and spectroscopic optical observations of the ultra-compact x-ray binary 4u 0614+091," *Astronomy & Astrophysics*, vol. 572, A99, Dec. 2014.

[175] D. Steeghs, J. E. McClintock, S. G. Parsons, M. J. Reid, S. Littlefair, and V. S. Dhillon, "THE NOT-SO-MASSIVE BLACK HOLE IN THE MICROQUASAR GRS1915+105," *ApJ*, vol. 768, no. 2, p. 185, Apr. 2013.

[176] P. A. Mason, E. L. Robinson, A. J. Bayless, and P. J. Hakala, "LONG-TERM OPTICAL OBSERVATIONS OF TWO LMXBs: UW CrB (=MS 1603+260) AND v1408 aql (=4u 1957+115)," *The Astronomical Journal*, vol. 144, no. 4, p. 108, Sep. 2012.

[177] A. Dieball, C. Knigge, D. R. Zurek, M. M. Shara, K. S. Long, P. A. Charles, D. C. Hannikainen, and L. van Zyl, "An ultracompact x-ray binary in the globular cluster m15 (NGC 7078)," *ApJ*, vol. 634, no. 1, pp. L105–L108, Nov. 2005.

[178] J. M. Corral-Santana, J. Casares, T. Shahbaz, C. Zurita, I. G. Martınez-Pais, and P. Rodrıguez-Gil, "Evidence for a black hole in the x-ray transient XTE j1859+226," *Monthly Notices of the Royal Astronomical Society: Letters*, vol. 413, no. 1, pp. L15–L19, Feb. 2011.

[179] K. H. Hinkle, F. C. Fekel, R. R. Joyce, J. Mikołajewska, C. Gałan, and T. Lebzelter, "Infrared spectroscopy of symbiotic stars. XII. the neutron star SyXB system 4u 1700+24 = v934 herculis," *ApJ*, vol. 872, no. 1, p. 43, Feb. 2019.

[180] Z. Ioannou, E. L. Robinson, W. F. Welsh, and C. A. Haswell, "The mass of the black hole in GS 2000+25," *Astron J*, vol. 127, no. 1, pp. 481–488, Jan. 2004.

[181] N. A. Webb, T. Naylor, Z. Ioannou, P. A. Charles, and T. Shahbaz, "A TiO study of the black hole binary GRO j0422+32 in a very low state," *Monthly Notices of the Royal Astronomical Society*, vol. 317, no. 3, pp. 528–534, Sep. 2000.

[182] M. G. Watson and M. J. Ricketts, "The periodic behaviour of 2a 0042 + 323 (=3u 0042 + 32)," *Monthly Notices of the Royal Astronomical Society*, vol. 183, no. 1, 35P–38P, May 1978.

[183] J. Casares, P. A. Charles, and T. Naylor, "A 6.5-day periodicity in the recurrent nova v404 cygni implying the presence of a black hole," *Nature*, vol. 355, no. 6361, pp. 614–617, Feb. 1992.

[184] R. Staubert, D. Klochkov, and J. Wilms, "Updating the orbital ephemeris of hercules x-1; rate of decay and eccentricity of the orbit," *Astronomy & Astrophysics*, vol. 500, no. 2, pp. 883–889, 2009.

[185] J. Casares, J. I. G. Hernández, G. Israelian, and R. Rebolo, "On the mass of the neutron star in cyg x-2," *Monthly Notices of the Royal Astronomical Society*, vol. 401, no. 4, pp. 2517–2520, Feb. 2010.

[186] E. Bozzo, M. Falanga, A. Papitto, L. Stella, R. Perna, D. Lazzati, G. Israel, S. Campana, V. Mangano, T. D. Salvo, and L. Burderi, "X-ray eclipse time delays in 4u 2129+47," *Astronomy & Astrophysics*, vol. 476, no. 1, pp. 301–306, Oct. 2007.

[187] J. I. G. Hernandez, R. Rebolo, and J. Casares, "Fast orbital decays of black hole x-ray binaries: XTE j1118+480 and a0620-00," *Monthly Notices of the Royal Astronomical Society: Letters*, vol. 438, no. 1, pp. L21–L25, Nov. 2013.

[188] A. Patruno, "The slow orbital evolution of the accreting millisecond pulsar IGR j0029+5934," *ApJ*, vol. 839, no. 1, p. 51, Apr. 2017.

[189] O. W. Butters, A. J. Norton, K. Mukai, and J. A. Tomsick, "RXTE andXMMobservations of intermediate polar candidates," *Astronomy & Astrophysics*, vol. 526, A77, Dec. 2010.

[190] G. Maier, O. Blanch, D. Hadasch, N. Komin, A. López-Oramas, M. Lundy, D. Malyshev, J. Moepi, S. Ohm, G. Pühlhofer, R. Prado, D. F. Torres, S. Schlenstedt, and B. Zitzer, "Long-term gamma-ray observations of the binary HESS J0632+057 with H.E.S.S., MAGIC and VERITAS," in *Proceedings of 36th International Cosmic Ray Conference — PoS(ICRC2019)*, vol. 358, 2019, p. 732.

[191] M. Linares, P. Miles-Páez, P. Rodrıguez-Gil, T. Shahbaz, J. Casares, C. Fariña, and R. Karjalainen, "A millisecond pulsar candidate in a 21-h orbit: 3fgl j0212.1+5320," *Mon. Not. R. Astron. Soc.*, vol. 465, no. 4, pp. 4602–4610, Nov. 2016.

VITA

Chun Fai (Chris) Tung was born in Hong Kong in 1991 and was raised there. He attended the Chinese University of Hong Kong as an undergrad where he received a Bachelor of Science in Physics and later a Master of Philosophy in Physics. During his time as a graduate student in CUHK, Chris participated in the research of biophysics. After graduating from CUHK, Chris moved to Atlanta, GA, and enrolled in the graduate school at the Georgia Institute of Technology, where he began his research in particle astrophysics.